

**CFD SIMULATION OF TWO- AND THREE-PHASE FLOW IN FCC REACTORS**

by

Amir Hossein Ahmadi Motlagh

M.Sc., Iran University of Science and Technology, 2008

B.Sc., Sharif University of Technology, 2003

A THESIS SUBMITTED IN PARTIAL FULFILLMENT OF  
THE REQUIREMENTS FOR THE DEGREE OF

DOCTOR OF PHILOSOPHY

in

THE FACULTY OF GRADUATE AND POSTDOCTORAL STUDIES  
(Chemical and Biological Engineering)

THE UNIVERSITY OF BRITISH COLUMBIA

(Vancouver)

March 2015

© Amir Hossein Ahmadi Motlagh, 2015

## **Abstract**

Liquid distribution and evaporation in Fluid Catalytic Cracking (FCC) reactors are investigated numerically. The well-documented inaccuracy of conventional two-fluid modeling of hydrodynamics in fluidized beds of Geldart Group A particles is revisited. A new force-balance (FB) sub-grid-scale model, introduced and applied to the conventional Wen-Yu drag correlation, analyzes the balance of van der Waals, drag, gravity and buoyancy forces. It predicts formation of agglomerates inside the bed, updating the drag calculations by applying a correction factor to the conventional drag models. Good predictions are obtained of fluidization regimes and bed expansion, and there is promising agreement with experimental time-average radial voidage profiles reported by Dubrawski et al. (2013). Good quantitative agreement between discrete element models (DEM) and two-fluid predictions of minimum bubbling velocity is also observed when the model is used to predict minimum bubbling velocity, in contrast to the predictions from a non-cohesive, Wen-Yu model.

Liquid injection experiments on a lab-scale fluidized bed were conducted, at the Institute of Chemical and Fuels from Alternative Sources (ICFAR) in London, Ontario to study the distribution, as well as the penetration, of liquid into catalyst pores. The results shed light on complexities involved in the injection zone to understand the effect of superficial gas velocity on evaporation and imbibition of liquid into particle pores. A methodology is developed to couple and incorporate existing liquid imbibition (into particle pores) models with evaporation models in the CFD code. The results are compared to another set of lab-scale experiments conducted at the British Columbia Research Institute (BCRI) facilities in Burnaby, BC. Simulation results demonstrate that CFD models can capture correct qualitative behavior of liquid injection and

evaporation inside the bed. However, quantitative deviations revealed the likely effect of hydrodynamic properties on drying from both the liquid film around the particles and inside the pores. The deviations also imply that the assumption of convection- or diffusion-dominant drying might be unsuitable, and the two should be combined. Based on experimental results, a methodology is proposed to include the effect of hydrodynamic properties such as superficial gas velocity and particle impact velocity on drying.

## **Preface**

The main chapters of this thesis have already been, or will soon be, submitted to journals for publication. A paper incorporating content very similar to Chapters 2 to 3 has been published as Ahmadi Motlagh, A. H., Grace, J. R., Salcudean, M. and Hrenya, C. M., *Chemical Engineering Science*, 120, 22-36, 2014.

Chapter 4 is based on work conducted at Institute of Chemical and Fuels from Alternative Sources (ICFAR), under co-supervision of Drs. Cedric Briens and Franco Berruti of Western University in London, ON.

The experimental results in Chapter 5 are based on work carried out at the British Columbia Research Institute (BCRI) in Burnaby, BC by Drs. Xuantian Li, Anwu Li and others.

The model that is described and tested in Chapters 2 and 3 is coded as a set of User-Defined-Functions (UDF) in ANSYS Fluent software. The model is currently patent pending and the interested reader should contact the author to obtain a working copy of the model UDFs.

# Table of Contents

<b>Abstract.....</b>	<b>ii</b>
<b>Preface.....</b>	<b>iv</b>
<b>Table of Contents .....</b>	<b>v</b>
<b>List of Tables .....</b>	<b>x</b>
<b>List of Figures.....</b>	<b>xii</b>
<b>List of Symbols and Abbreviations .....</b>	<b>xviii</b>
<b>Acknowledgements .....</b>	<b>xxiii</b>
<b>Chapter 1: Introduction .....</b>	<b>1</b>
1.1    Background.....	1
1.2    Motivation.....	3
1.3    Literature review.....	4
1.3.1    Hydrodynamics and numerical methods.....	4
1.3.2    Liquid injection (experiments and modeling).....	14
1.4    Summary.....	18
1.5    Objectives of this thesis .....	18
<b>Chapter 2: Force-Balance (FB) Model.....</b>	<b>21</b>
2.1    Background.....	21
2.2    Model description .....	25
2.2.1    Drag force ( $F_d$ ).....	25
2.2.2    Collisional force ( $F_c$ ).....	28
2.2.3    Gravitational/buoyancy force ( $F_g$ ).....	30

2.2.4	van der Waals force ( $F_{vw}$ ) .....	30
2.3	Analysis of force vectors .....	38
2.4	Calculation of agglomerate diameter .....	40
2.5	Summary .....	50
<b>Chapter 3: Comparison of FB Model Predictions with Experimental Results and Other Models .....</b>		<b>51</b>
3.1	Case I – Fluidization regime and bed expansion predictions comparing Wen-Yu and FB model.....	52
3.1.1	Simulation setup.....	52
3.1.2	Results and discussion .....	57
3.2	Case II– Qualitative and quantitative comparison of hydrodynamic predictions with other drag correction models .....	61
3.2.1	Boundary and initial conditions .....	62
3.2.2	Data collection and analysis: .....	63
3.2.3	Results and discussion .....	65
3.2.3.1	2D-CFD simulation analysis.....	65
Effect of mesh size.....		65
Qualitative analysis of particle volume fraction .....		68
3.2.3.2	3-D simulation analysis.....	74
Mesh refinement study.....		74
Qualitative analysis of instantaneous particle concentration using CFD.....		76
Effect of different drag models .....		78
3.2.3.3	3D models and comparison with 2D simulations .....	81

3.3	Case III– minimum bubbling velocity, $U_{mb}$ .....	84
3.3.1	Simulation Setup.....	85
3.3.2	Results and discussion .....	87
3.4	Summary.....	89
<b>Chapter 4: Liquid Injection Experiments at ICFAR .....</b>		<b>92</b>
4.1	Background.....	92
4.2	Objectives .....	93
4.3	Experimental apparatus.....	94
4.3.1	Liquid injection assembly.....	98
4.4	Dry experiments (with no liquid injection).....	99
4.4.1	Sand.....	99
4.4.2	FCC.....	99
4.4.3	Voidage measurements .....	100
4.5	Liquid droplet size analysis .....	101
4.6	Liquid injection experiments (ethanol).....	106
4.6.1	Experimental procedure .....	106
4.6.2	Experimental data on capacitance and liquid content.....	107
4.6.3	Small box experiments.....	114
4.6.4	Normalized capacitance vs. liquid content .....	116
4.7	Liquid distribution inside FCC pores.....	121
4.8	Conclusions.....	124
<b>Chapter 5: Liquid Imbibition/Vaporization Model in Porous Media.....</b>		<b>126</b>
5.1	Background.....	126

5.2	Experiments .....	126
5.3	Physics .....	128
5.3.1	Imbibition model.....	133
5.3.2	Drying experiments and models .....	137
5.3.3	Drying model .....	140
5.3.3.1	Convection drying.....	140
5.3.3.2	Diffusion drying.....	141
5.3.4	Maximum liquid film growth.....	142
5.4	Structure of the CFD model.....	145
5.4.1	Mass transfer mechanisms .....	146
5.4.2	Modeling species/phase transport.....	147
5.4.3	Mechanism of liquid film thickness growth in CFD modeling .....	148
5.4.4	CFD solution procedure.....	149
5.5	Simulation setup.....	152
5.5.1	Mesh study .....	153
5.5.2	Time-step study.....	154
5.6	Results and discussion .....	156
5.6.1	A) Effect of imbibition and drying (before pore saturation).....	156
5.6.2	B) Effect of imbibition and drying (after pore saturation-injection continues) .....	163
5.6.3	C) Effect of imbibition and drying (after pore saturation-no injection) .....	166
5.6.4	Mechanism for drying from inside particle pores.....	169
5.7	Conclusion .....	171
<b>Chapter 6: Summary, Contribution and Future Work .....</b>		<b>173</b>

6.1	Summary and contributions .....	173
6.2	Recommendations for future work .....	175
<b>Bibliography .....</b>		<b>177</b>

## List of Tables

Table 2.1 Equations for performing vector calculations.....	43
Table 2.2 Equations for four possible collision scenarios .....	46
Table 3.1 Simulation conditions and physical properties for traveling fluidized bed of Dubrawski et al. (2013) with air as the fluidizing gas.....	54
Table 3.2 Hydrodynamic equations for gas-solid system.....	56
Table 3.3 Expanded bed height predictions.....	61
Table 3.4 Input parameters used in the Case II simulation.....	62
Table 3.5 Physical and simulation parameters used in modeling based on values given by Hou et al. , (2012). .....	86
Table 4.1 Physical properties and dimensions for injection experiments.....	107
Table 4.2 Liquid-to-solid mass ratio measurements at different superficial gas velocities for FCC/ethanol system with properties listed in Table 1 (22 kg of FCC inventory) .....	113
Table 4.3 Root-Mean-Square (RMS) deviations of measured normalized capacitance data at all 20 electrodes from the actual data read from calibration curve at different sampling times for case #1 in Table 4.2 (superficial gas velocity = 0.15 m/s, injected ethanol volume = 150 ml). Electrode positions are shown in Fig 4.1. ....	118
Table 4.4 Root-Mean-Square (RMS) deviations of measured normalized capacitance data at all 20 electrodes from the actual data read from calibration curve at different sampling times for case #2 (superficial gas velocity = 0.2 m/s, injected ethanol volume = 200 ml)). Electrode positions are shown in Fig 4.1. ....	119
Table 4.5 Liquid distribution in pores and in interstices .....	124

Table 5.1 Properties used when calculating capillary number .....	145
Table 5.2 Summary of phase properties for tests at atmospheric pressure and 60 °C .....	151
Table 5.3 Simulation setup values of operating and geometric quantities .....	153
Table 5.4 Physical properties for Case FCC-1 at 60°C.....	157

## List of Figures

Figure 1.1 Typical schematic of fluid catalytic cracker(Sadeghbeigi, 2012). .....	2
Figure 1.2 Multi-level modeling schemes (Deen et al., 2007).....	5
Figure 1.3 Concept of formation of particle clusters due to granular temperature relaxation via collisional cooling and subsequent cohesive interaction. (Cocco et al., 2010).....	8
Figure 1.4 Effect of grid size for the highest gas velocity ( $U = 0.018\text{m/s}$ ). At the far left is the initial bed used in the simulation. The grid sizes are:(a) $0.5\text{mm}(x)\times 0.2\text{mm}(y)\times 0.6\text{mm}(z)$ , (b) $0.3\text{mm}\times 0.2\text{mm}\times 0.4\text{mm}$ , (c) $0.2\text{mm}\times 0.2\text{mm}\times 0.3\text{mm}$ ,and(d) $0.2\text{mm}\times 0.2\text{mm}\times 0.2\text{mm}$ . (Wang et al., 2009).....	11
Figure 2.1 Schematic of force balance model.....	25
Figure 2.2 Plot of drag force correction factor ( $\Omega$ ) vs. internal voidage ( $\epsilon_i$ ) for three different agglomerate diameters with $d_p = 100\ \mu\text{m}$ using Brinkman's extension of Darcy equation for low Reynolds numbers.....	28
Figure 2.3 Contact of two-coated cohesive particles and location of guest particles based on Chen et al. (2008).....	33
Figure 2.4 Changes of van der Waals force with asperity diameter ( $d_p = 100\ \mu\text{m}$ , $A = 10\text{-}19\ \text{J}$ , $d = 0.4\ \text{nm}$ , weight of particle = $8\times 10^{-9}\ \text{N}$ , $\rho_p = 1560\ \text{kg/m}^3$ ).....	34
Figure 2.5 SEM images of whole FCC catalyst particles (top) and close-up (bottom) for $d_p$ of $100\ \mu\text{m}$ . .....	37
Figure 2.6 Schematic of possible force scenarios. Each of these scenarios can result in agglomerate formation based on the magnitude and direction of the force vectors. ....	39
Figure 2.7 Agglomerate diameter calculation procedure repeated in each computational cell. ...	45

Figure 2.8 Schematic of solid fluxes from neighboring computational cells for calculation of new agglomerate diameter.....	47
Figure 2.9 Algorithm for calculation of agglomerate diameter.....	49
Figure 3.1 Fluidization pattern showing solid volume fraction at different times with properties in Table. 3.1 for Conventional Wen-Yu drag model (Left) and FB model with Wen-Yu drag model (Right).....	59
Figure 3.2 Bed expansion predictions (Y-axis given in meters) by FB model from contour of time-averaged solid volume fraction for $U = 0.4$ m/s.....	60
Figure 3.3 Schematic of computational domain (2D).....	65
Figure 3.4 Contours of solid volume fraction at $U = 0.4$ m/s, $d_p = 103$ mm, $\phi = 0.001$ . Left side in each case represents snapshot at $t=15$ s, whereas right side provides time-average over last 10 s. ....	67
Figure 3.5 Radial profiles of time-average particle velocity at heights of 0.4 m (top figure) and 0.56 m (bottom figure) predicted by FB model.....	68
Figure 3.6 Instantaneous particle volume fraction of FCC at $U = 0.4$ m/s, $d_p = 103$ mm, $\phi = 0.1$ . ....	69
Figure 3.7 Qualitative comparison of particle volume fraction of FCC at $U = 0.4$ m/s, $d_p = 103$ mm, $\phi = 0.1$ , $t = 15$ s (a) EMMS-Shi model (b) EMMS-Hong model (c) FB model.....	70
Figure 3.8 Radial profiles of time-average voidage at different heights for a) $U = 0.3$ m/s and b) $U = 0.4$ m/s.....	71
Figure 3.9 Effect of specularity coefficient on radial profile of voidage for $U = 0.4$ m/s, $d_p = 103$ m. Top row at $z=0.56$ m, middle row at $z=0.4$ m, bottom row at $z=0.24$ m.....	73

Figure 3.10 Mesh studies at $U = 0.4$ m/s, $d_p = 103$ mm and $\phi = 0.1$ at different heights. (a) and (b) represent radial profiles of time-average voidage, whereas (c) and (d) show radial profiles of time-average particle velocity in axial direction .....	75
Figure 3.11 FB model prediction of instantaneous gas and particle velocity vectors at $U = 0.4$ m/s and $t = 15$ s. ....	77
Figure 3.12 Variation of axial profile of particle volume fraction averaged over last 10 s of simulation with height at $U = 0.4$ m/s for different drag models.....	79
Figure 3.13 Contours of time-average solid volume fraction at $U = 0.4$ m/s for bed expansion comparing EMMS-Hong and FB models. ....	80
Figure 3.14 Qualitative analysis of 2D snapshots of FCC volume fraction at $U = 0.4$ m/s, $\phi = 0.001$ , $t = 15$ s: (a) Wen-Yu (b) EMMS-Shi (c) EMMS- Hong (d) FB model. ....	81
Figure 3.15 Comparison of radial profiles of time-average voidage from 2D and 3D simulations with experimental results at $U = 0.4$ m/s. ....	82
Figure 3.16 Probability distribution plot for number of particles in agglomerate obtained from 3D simulations at $U = 0.4$ m/s. ....	83
Figure 3.17 Contours of mean granular temperature ( $m^2/s^2$ ) for superficial gas velocities of 0.007 m/s (left), 0.01 m/s (middle) and 0.012 m/s (right) with mesh size = $10 \times d_p$ .....	87
Figure 3.18 Contour of local granular temperature ( $m^2/s^2$ ) for a superficial gas velocity of 0.012 m/s at $t = 4$ s with mesh size = $10 \times d_p$ .....	88
Figure 4.1 Electrode configuration and numbering scheme (not to scale) for ICFAR column....	96
Figure 4.2 Schematic of Experimental Equipment. ....	97
Figure 4.3 Schematic of liquid injection assembly (not to scale). ....	98

Figure 4.4 Particle size distribution for the silica sand particles (Farkhondehkavaki et al., 2012).	99
Figure 4.5 Cumulative particle size distribution of FCC particles	100
Figure 4.6 Laser-photocell arrangement used for open-air experiments (adapted fromPortoghese et al. (2008)).	101
Figure 4.7 Laser-photocell curves used for the open-air experiments. (a) Experimental values for injection of 200 ml of Ethanol initiated at $t=5$ s , (b) $\epsilon_a = 0$ for $t \leq 15$ s and $\epsilon_a = 1$ for $15 < t < 35$ s , (c) Calibration linear curve.	105
Figure 4.8 Normalized capacitance vs. time for FCC and ethanol (Injection started at $t=150$ s with a liquid flowrate of $0.0004$ m <sup>3</sup> /min), superficial gas velocity = $0.2$ m/s.	109
Figure 4.9 Normalized capacitance vs. time for sand and ethanol (Injection started at $t=150$ s with a liquid flowrate of $0.0004$ m <sup>3</sup> /min), and superficial gas velocity = $0.2$ m/s.	109
Figure 4.10 Time-averaged local normalized capacitance of whole bed (after injecting 200 ml ethanol at $t = 150$ s for duration of 30 s at superficial gas velocity of $0.2$ m/s). (a) and (b): FCC (averaged from $t=160$ to $180$ s and $220$ to $240$ s respectively), (c) and (d): sand (averaged from $t=160$ to $180$ s and $220$ to $240$ s, respectively).	111
Figure 4.11 Liquid-to-solid mass ratio measurements vs. time after adding 200 ml of ethanol.	114
Figure 4.12 Schematic showing small box experiment for FCC/ethanol system.	115
Figure 4.13 Calibration curve from FCC/ethanol small box experiments for relating normalized capacitance data to liquid content.	116
Figure 4.14 Mean liquid-to-solid mass ratio measurements of all 20 electrodes vs. time at different superficial gas velocities for injection of 200 ml ethanol over a time span of 30 s.	121

Figure 4.15 Moisture removal of sample vs. Time (Drying curve) for superficial gas velocity of 0.20 m/s after injection of 200 ml ethanol. ....	123
Figure 5.1 Experimental setup and location of sampling points SP4 and SP5 which are on the same face of the column. ....	127
Figure 5.2 Schematic of liquid film formation and penetration inside the pores. ....	129
Figure 5.3 Schematic of drying experiments. ....	138
Figure 5.4 Mixture weight index (non-dimensional) vs. time (s) at ambient condition for three fan speeds (1000, 1400 and 1750 rpm). The circles show transition in drying from falling to constant rate. ....	139
Figure 5.5 Mixture weight (g) vs. time (s) at T = 60 °C. ....	140
Figure 5.6 Solution Procedure for Pressure-Based Coupled Solver. ....	150
Figure 5.7 Effect of mesh size on heptane concentration in vapor phase predicted by CFD model. ....	155
Figure 5.8 Effect of time-step on heptane concentration in vapor phase predicted by CFD model. ....	155
Figure 5.9 Development of wet particles volume fraction over first second after initiation of liquid jet. ....	159
Figure 5.10 Development contours of imbibed liquid height (m) inside pores. Scale is in m. ..	160
Figure 5.11 Concentration of heptane (ppmv) in vapor phase mapping.....	161
Figure 5.12 Experimental data (moving averaged over 5 s) for evaporated liquid concentration in case FCC-1. Vertical and horizontal dashed lines indicate initiation of liquid injection and error margins, respectively for location of SP4, per Fig. 5.1.....	162

Figure 5.13 Average liquid imbibition height (m) vs. time (s) after initiation of liquid injection.  
The dashed line shows the maximum imbibition capacity. .... 163

Figure 5.14 Time-average experimental and CFD results for liquid evaporation at sample points  
SP4 and SP5, per Fig. 5.1. .... 164

Figure 5.15 Experimental results for evaporated liquid concentration (PPMV) at SP4 and SP5 vs.  
time. The circles indicate possible changes of slope, which could suggest multiple drying  
mechanisms. .... 166

Figure 5.16 Experimental results for evaporated liquid concentration (PPMV) at SP4 and SP5  
vs. time (after liquid injection stops). Top sub-figure shows the whole drying curve, and  
bottom one magnifies drying section 3. .... 168

## List of Symbols and Abbreviations

$A$	Hamakar constant, J
$A_b$	cross-sectional area of laser beam, $m^2$
$ALR$	air-to-liquid mass ratio, [-]
$a$	coefficient in Eq. 2.23
$C$	electrical capacitance, F
$C_d$	drag coefficient, [-]
$D$	mass diffusivity of vapor in gas, $m^2/s$
$d$	diameter, $\mu m$
$E$	Young's modulus, $N/m^2$
$e$	coefficient of restitution, [-]
$f_{p,d}$	frequency of collisions between liquid droplets and dry particles, $1/m^3.s$
$f_{pd,w}$	frequency of collisions between dry and wet particles, $1/m^3.s$
$F_g$	gravity force, N
$F_c$	collisional force, N
$F_d$	drag force, N
$F_v$	viscous force, N
$F_{vw}$	van der Waals force, N
$F_{vw\_aa}$	van der Waals force from asperity-asperity contact, N
$g$	gravitational acceleration, $m/s^2$
$g_0$	radial distribution function, [-]
$h$	height above distributor in Chapter 3 and thickness of deposited liquid film in Chapter 5, m
$h_{expanded}$	expanded bed height, m
$h_{imb}$	liquid film thickness after liquid imbibition into particle pores
$h_{mf}$	bed height corresponding to minimum fluidization, m
$h_r$	separation distance at time of collision, m
$H_0$	particle-particle separation distance, m
$J$	impulse, $kg.m/s$

$k_{\theta}$	diffusion coefficient for granular energy, kg/m.s
$l$	length of laser beam exposed to liquid spray jet, m
$m$	mass, kg
$M\%$	moisture content defined in Eq. 4.10, [-]
$N$	number of agglomerates in Chapter 2 and number of liquid droplets in Chapter 4, [-]
$N_{pore}$	number of pores inside particle, [-]
$n$	exponent in Eq. 5.23, [-]
$n_{wet}$	number of wet particles in computational cell, [-]
$P$	pressure, Pa
$P^*_v$	saturation vapor pressure, Pa
$q$	mass transfer rate, kg/m <sup>3</sup> .s
$r$	radius, m
$SAC$	surface area coverage, [-]
$Sc$	Schmidt number, [-]
$St$	Stokes number, [-]
$St^*$	critical Stokes number, [-]
$T_c$	collision duration, s
$U_{mb}$	minimum bubbling velocity, m/s
$U$	superficial gas velocity, m/s
$v$	velocity, m/s
$V$	volume in Chapter 4, m <sup>3</sup>
$V_{evap}$	evaporated liquid volume, m <sup>3</sup>
$V_{film,cell}$	liquid film volume around wet particles in each computational cell, m <sup>3</sup>
$V_{inj}$	liquid injected volume available in droplet form, m <sup>3</sup>
$V_l$	volume of liquid in particle pore in Chapter 5, m <sup>3</sup>
$V_{pore}$	volume of liquid in particle pores, m <sup>3</sup>
$V_{wet}$	total volume of all wet particles in bed, m <sup>3</sup>
$v'$	velocity after collision in Chapter 2 and particle fluctuation velocity in Chapter 5, m/s

$y$	liquid penetration depth, m
$y^*$	vapor molar fraction at saturation, [-]
$y_g$	vapor molar fraction at bulk gas, [-]
$X$	mass fraction of species, [-]
$z$	vertical coordinate, m
$Z_0$	minimum separation distance, m

*Greek letters*

$\beta$	drag coefficient in Chapter 2, kg/m.s, mass transfer coefficient in Chapter 5, m/s
$\gamma$	variable in Eq. 2.4
$\gamma_\theta$	collision dissipation of energy, kg/m.s <sup>3</sup>
$\delta$	distance between particles, m
$\varepsilon$	volume fraction, [-]
$\varepsilon_p$	intraparticle porosity, [-]
$\theta$	granular temperature, J/kg
$\lambda_s$	solid bulk viscosity, kg/m.s
$\mu$	shear viscosity, kg/m.s
$\vartheta$	Poisson ratio, [-]
$\rho$	density, kg/m <sup>3</sup>
$\sigma$	liquid surface tension, N/m
$\tau$	stress tensor, Pa
$\phi$	specularity coefficient used in wall boundary condition
$\varphi_{gs}$	transfer rate of kinetic energy, kg/m.s <sup>3</sup>
$\Omega$	drag correction for flow through porous structure, [-]

*Subscripts*

$0$	initial condition
$a$	agglomerate
$as$	asperity
$ca$	capillary

<i>cv</i>	control volume
<i>d</i>	dry
<i>dry</i>	dry condition
<i>film</i>	liquid film around solid particle
<i>g</i>	gas
<i>gr</i>	gravity
<i>hs</i>	hydrostatic
<i>i,j</i>	index for phases
<i>imb</i>	imbibition
<i>l</i>	liquid
<i>m</i>	index for phases
<i>max</i>	maximum packing
<i>measured</i>	measured data
<i>mf</i>	minimum fluidization
<i>new_agg</i>	agglomerates formed at current timestep in simulations
<i>old_agg</i>	agglomerates formed at previous timestep in simulations
<i>p</i>	particle
<i>pore</i>	particle internal porosity
<i>s</i>	solid
<i>T</i>	temperature
<i>vw</i>	van der Waals
<i>w</i>	wall
<i>wet</i>	wet condition
<i>x,y</i>	x- and y- coordinates

### *Abbreviations*

<i>BCRI</i>	British Columbia Research Institute
<i>CFD</i>	Computational Fluid Dynamic
<i>DEM</i>	Discrete Element Model
<i>DNS</i>	Direct Numerical Simulation

<i>DPM</i>	Discrete Particle Model
<i>EMMS</i>	Energy Minimization Multi Scale
<i>FEM</i>	Filtered Eulerian Model
<i>ICFAR</i>	Institute of Chemical and Fuels from Alternative Sources
<i>PBE</i>	Population Balance Equation
<i>SGS</i>	Sub-Grid Scale

## **Acknowledgements**

I would like to express my sincere gratitude to my outstanding supervisors: Dr. John Grace and Dr. Martha Salcudean for their advice, support, kindness, encouragement and patience throughout my graduate studies. I feel truly blessed and honored to have had the opportunity to work under their supervision. They provided me the best knowledge to improve myself further in the academic world. I also gratefully acknowledge Dr. Christine Hrenya from the University of Boulder, Colorado, for her contributions, technical support and kind assistance during development of models and simulation studies in this work. I also express gratitude to committee members Drs. Fariborz Taghipour and Dana Grecov for their comments and suggestions during my PhD work.

I would like to thank sincerely the contribution and guidance of Dr. Cedric Briens and Dr. Franco Berruti from the Institute of Chemicals and Fuels from Alternative Resources (ICFAR) at Western University in London, ON. I also express gratitude to Masoumeh Farkhondehkavaki, Majid Hamidi and Maryam Mohagheghi who assisted me during my stay at ICFAR to conduct liquid injection experiments.

I express my sincere gratitude to Dr. Xuantian Li and Dr. Anwu Li from British Columbia Research Institute (BCRI) and Dr. Mike Wormsbecker of Syncrude Canada Ltd. who facilitated my access to experimental data.

I am also very grateful to my friends in CHBE and group members for their valuable suggestions and support in this path, in particular: Dr. Subhashini Vashisth and Sina Tebianian.

Finally, I would like to express my everlasting gratitude to my beloved wife, Saviz, for her passion and understanding, and to my parents for their love, support, and tireless deduction.

*To my parents*

# Chapter 1: Introduction

## 1.1 Background

Fluid catalytic cracking (FCC) is used to upgrade low-value refinery gas-oil feedstock to more valuable products. It continues to play a key role in integrated oil refineries as the primary conversion process. For many refiners, the “cat cracker” is the key to profitability, in that successful operation of this unit determines whether or not the refiner can remain competitive in today's market. As of 2006, FCC units were in operation at 400 refineries worldwide (Speight, 2006), with a total processing capacity of over 14.7 million barrels per day (Sadeghbeigi, 2012). The FCC process generates more than 40% of the gasoline in the refinery pool; consequently, any small benefit in this process is very profitable (Ancheyta, 2011).

FCC process hardware, catalysts and operation have continued to co-evolve with ever-changing economic and environmental requirements (Sadeghbeigi, 2012). Dramatic improvements have been achieved in several areas, such as:

- Size of the unit, (elevation, volume, catalyst inventory) and hence cost of a FCC unit per barrel of feed charged and converted.
- Conversion and product selectivity.
- Feedstock flexibility.

FCC technology has experienced a sharp increase in feedstock flexibility since the early 1970s, driven by the first (after-the-war) oil crisis. Also, this arena is shifting significantly. This is happening on the supply side (feedstock supply and quality), as well as with respect to products demand and quality (Sadeghbeigi, 2012).

Fig. 1.1 sketches one typical unit configuration offered by a major technology licensor. Despite different mechanical configurations of FCCs, the common objective of upgrading low-value feedstock to more valuable products remains the same.

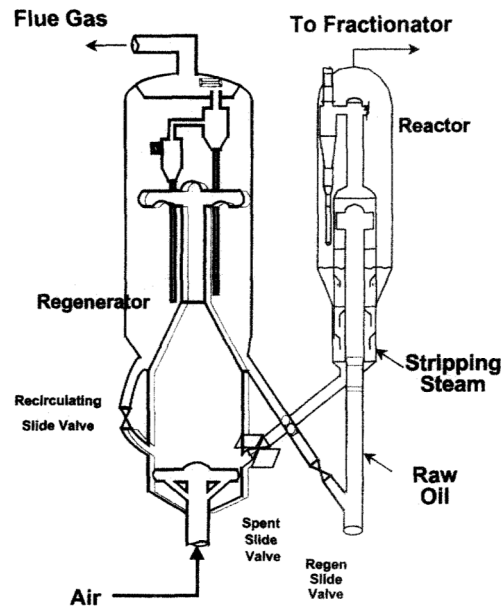


Figure 1.1 Typical schematic of fluid catalytic cracker(Sadeghbeigi, 2012).

Refinery-produced gas oil and any supplemental FCC feedstock are normally heated to a temperature of 260 to 370°C. The preheated feed enters the riser near the base where it contacts regenerated catalyst. The heat absorbed by the catalyst in the regenerator provides the energy to heat the feed to the desired reactor temperature. The overall reaction occurring in the riser is endothermic. The circulating catalyst provides this energy. Typical regenerated catalyst temperatures range from 680 to 730°C.

Catalytic reactions occur in the vapor phase. Cracking reactions begin as soon as the feed is vaporized. The expanding flow of the generated vapors provide the main driving force to carry the catalyst up the riser. The riser is a vertical pipe, usually with a 100 to 130 mm-thick

refractory lining for insulation and abrasion resistance. Typical risers are 0.6 to 2.1m in diameter and 23 to 37 m tall (Sadeghbeigi, 2012).

Efficient contacting between the feed and catalyst is critical to achieve the desired cracking reactions. Steam is commonly used to atomize the feed. Smaller oil droplets increase the availability of feed at the reactive acid sites on the catalyst. After exiting the riser, catalyst enters the reactor vessel. In this vessel further cracking occurs, as well as providing additional catalyst separation. The spent catalyst falls into the stripper where addition of steam removes entrained hydrocarbons from catalyst particles.

## **1.2 Motivation**

In view of the importance of FCC reactors in the oil refinery, a more comprehensive understanding of the riser reactor mechanisms is vital. A thorough review of the research and development related to FCC risers can be divided into three categories (Gao et al., 1999):

- Hydrodynamic behavior of two-phase flow in risers
- Complex feed vaporization phenomena in the feed-injection zone.
- Catalytic cracking kinetic models

The initial process occurring at the bottom of the riser reactor becomes the important step in determining unit performance, even dominating the product distribution and quality (Mauleon & Couelle, 1985; Mirgain et al., 2000). From the numerical modeling point of view, different frameworks exist which are already being utilized in modeling FCC riser reactors. New techniques are being developed that have the advantage of more accurate prediction of the fluid flow inside these reactors, however these require further investigation.

Catalytic cracking chemical kinetic models are not considered in this study. The main emphasis is instead on the numerical simulation of hydrodynamics in these risers. In addition, the application of existing three-phase models for treating the complexity of flow behavior in the feed injection zone is investigated in this work.

### **1.3 Literature review**

#### **1.3.1 Hydrodynamics and numerical methods**

Correct understanding of the hydrodynamic characteristics is essential for proper design and scale-up of FCC reactors. Computational Fluid Dynamics (CFD) has been successfully applied to model the hydrodynamics of gas-fluidized beds. With its increased computational capabilities, CFD has become an important tool for understanding the complex phenomena between the gas phase and the particles in fluidized bed reactors.

According to Sinclair (1997), numerical models describing the flow behavior of gas-solid mixtures can be classified as either Lagrangian or Eulerian based on the framework in which they are developed. In the Lagrangian approach, a separate equation of motion must be solved for each particle in the flow field, whereas in the Eulerian approach, the phases are treated as separate interpenetrating continua, while the interactions between phases are accounted for by supplementary equations. In a Lagrangian framework, a large number of particle trajectories must be calculated in order to determine the average behavior of the system, which is a drawback of the Lagrangian approach. In contrast, in an Eulerian framework, each phase is represented by only one equation of motion. However, these models require a set of closure laws to adequately define the terms in continuum equations requiring solution of a large number of equations. Unlike Lagrangian models, Eulerian models can be applied to flows of practical interest with

relatively little computational effort. Therefore, the present work relies on the Eulerian-Eulerian approach for both solid and gas phases.

Numerical simulation of gas-solid systems usually requires multi-level modeling as shown in Fig. 1.2 (Deen et al., 2007). The most fundamental level is direct numerical simulation (DNS), where all relevant spatio-temporal scales of the fluid and particle phases are resolved and coupled through the no-slip boundary condition at the fluid-particle interfaces; on a higher level are discrete particle/element models (DPM) where the Eulerian approach is used to track the hydrodynamics of the fluid phase, whereas the particle phase is still resolved as in DNS using the Lagrangian framework.

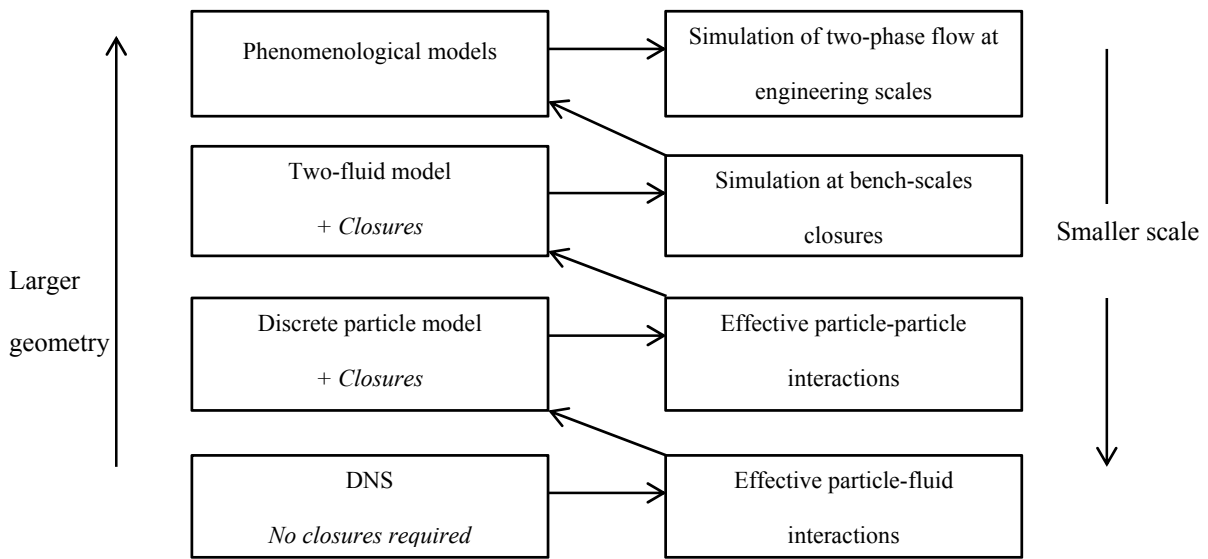


**Figure 1.2 Multi-level modeling schemes (Deen et al., 2007).**

At a higher level are two-fluid/multi-fluid models which utilize the Eulerian-Eulerian framework for solid gas and liquid phases, considered as interpenetrating continua. Simulations based on these models are mostly at bench scales and require phenomenological models to upgrade to engineering scales. To model gas–solid two-phase flows at different scales, one can

choose appropriate combinations of the gas- and solid phase models, depending on preference and the scale of the simulation domain. The basic idea is that smaller scale models, which take into account the various interactions in detail, are used to develop closure laws which can represent the effective ‘coarse-grained’ interactions in larger scale models.

In multi-fluid (as well as two-fluid) models, the particle phase is regarded as a continuum, and the distribution of momentum for the particle phase is obtained by some form of averaging. There are many ways to model two-phase flow problems using partial differential equations (PDEs), depending on the physical phenomena of interest and the nature of the problem. Anderson & Jackson (1967) and Gidaspow (1994) were among the earliest and most cited authors to present detailed fluid mechanical descriptions of fluidized beds. In their methodology, the equation of motion for the center of mass of a single particle is locally averaged over regions large enough to contain many particles, but small with respect to the bounding container. The details of the averaging procedure are well described by Enwald and Peirano (1997). A two-fluid model, i.e. gas-solid model, consists of two continuity equations, two momentum equations in each coordinate direction and two energy equations. Additional closure laws are needed to close the set of equations. A general procedure for developing a two-fluid model is described by Enwald and Peirano (1997). A similar approach can be utilized to obtain three-fluid models. The multi-fluid Eulerian-Eulerian model is less computationally intensive than Lagrangian models and more suitable for practical purposes.

In the classification of fluidized particles by Geldart (1973) which is characterized by the mean particle size and the density difference between particles and gas, FCC particles fall into

group A<sup>1</sup>. The standard Eulerian-Eulerian method for simulation of hydrodynamics in fluidized beds containing Geldart A particles has been often reported to fail in predicting the hydrodynamics of gas fluidized beds (e.g. Wang 2009; Wang et al. 2009; Loezos & Sundaresan 2005; Zimmermann & Taghipour, 2005),- most likely due to inter-particle forces and the existence of significant sub-grid scale heterogeneous structures.

Some research groups claim that the existence of significant inter-particle cohesive forces results in sub-grid scale heterogeneous structures which take the form of agglomerates or clusters (Gao et al. 2008; van Wachem & Sasic 2008); in this context, Kim and Arastoopour (2002) modified the kinetic theory of granular flow, aiming at including a complex cohesive force model. Their approach resulted in derivation of new governing equations and closure models primarily for the stresses of the particulate phase. In a similar approach, Gidaspow and Lu (1998) incorporated the empirically-determined cohesive pressure into the term representing the particle pressure, resulting in a higher predicted particle pressure compared to that obtained by the kinetic theory of granular flow for flows of non-cohesive particles.

Gidaspow and Arastoopour (2014) reviewed the evolution of CFD modeling of Circulating Fluidized Beds (CFB), discussing the application of kinetic theory, turbulence and heat transfer. They emphasized use of a Population Balance Equation (PBE) coupled with CFD to properly account for changes in particle dense phase properties such as agglomeration and breakage. Ye et al. (2005) modified the kinetic theory approach by adding an excess compressibility term that accounts for cohesion between particles. These models contain a number of empirical constants, whose magnitude is not always clear. Hence, the models might

---

<sup>1</sup> Geldart group A particles are mildly cohesive. Their size falls between 20 and 100  $\mu\text{m}$ , and the particle density is less than 2000  $\text{kg}/\text{m}^3$ . Most powder-catalyzed beds, as well as FCC, are in this group.

not be applicable for different operating conditions in all fluidized bed systems (Wang, 2009). Mazzei and Lettieri (2008) investigated the stability of homogeneous gas-fluidized suspensions and the transition from the particulate to the aggregative state. They reported that considering only buoyancy and drag forces in a fluidized bed leads to intrinsic instability of the homogeneous state of fluidization and that incorporation of terms like virtual mass force and lift force does not lead to any significant change in results.

Cocco et al. (2010) reported experimental visual observation of small-scale agglomerates or clusters in and above a fluidized bed of FCC catalyst powders. They suggested that hydrodynamics may not be solely responsible for cluster formation, with cohesive forces such as electrostatics, capillary and van der Waals forces playing a significant role in particle cluster formation. In their study, a mechanism is also proposed for the formation of particle clusters due to granular temperature relaxation via collisional cooling and subsequent cohesive interaction, as shown schematically in Figure 1.3.

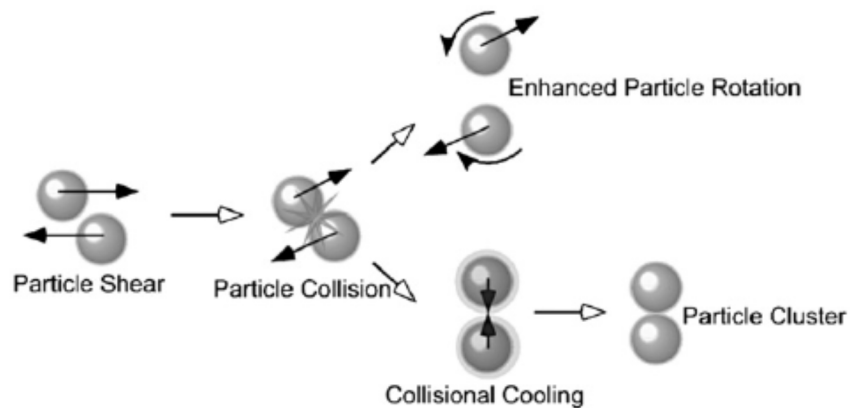


**Figure 1.3 Concept of formation of particle clusters due to granular temperature relaxation via collisional cooling and subsequent cohesive interaction. (Cocco et al., 2010).**

Other research groups (e.g. Wang et al. 2009; Agrawal et al. 2001; Loezos & Sundaresan 2005; Portoghese et al. 2008; Benyahia et al. 2007) claim that inter-particle cohesive forces are

not the dominant factor, and that the poor performance of two-fluid models is primarily due to grid sizes and time steps which are too coarse to fully resolve the mesoscale structure. Wang et al. (2011) studied a bubbling fluidized bed of Geldart A particles by using a discrete particle method and argued that there is no clustering structure in the bed. The difference between the results of Wang et al. (2011) and Cocco et al. (2010) could be due to different operating conditions and fluidizing regimes. However, Wang et al. (2011) stressed that their conclusion does not mean that inter-particle cohesive forces are not important for gas–solid flows in real industrial equipment, usually operated at high operating pressure and/or temperature.

The effects of 2D versus 3D simulations were studied by Cammarata et al. (2003) for the bubbling behaviour in a rectangular fluidized bed. The bed expansion, bubble hold-up, and bubble size calculated from 2D and 3D simulations were compared with the predictions obtained from an empirical correlation. Cammarata et al. (2003) reported that 3D simulations constituted a more realistic model of physical behaviour for fluidization. They also indicated that 2D simulations should only be used for sensitivity analyses.

Several research groups have confirmed that when the grid size and time step are sufficiently small to resolve the spatiotemporal structures, the correct bed expansion and hydrodynamics can be obtained by using standard two-fluid models with the kinetic theory of granular flow (Agrawal et al., 2001; Benyahia et al., 2007; Loezos & Sundaresan, 2005; Portoghese, House, et al., 2008; Wang et al., 2009). These studies stress that mesoscale structures appear as an effect of non-linear interphase interaction and dissipative particle-particle and particle-wall interactions which take the form of bubbles and/or clusters in gas-fluidized beds. The size of these structures varies from the size of a single particle diameter to riser diameter (Wang, 2009), making it difficult and time-consuming for numerical codes to capture

them. On the other hand, numerical codes use computational grids which are coarse with respect to the characteristic length scale of mesoscale structures, to reduce the required computational time. This approach results in failure to consider the effect of unresolved structures on the closure laws. Consequently, conventional Eulerian models fail to predict the hydrodynamics of gas-fluidized beds.

Figure 1.4, adapted from Wang et al. (2009), shows the effect of grid size in capturing the mesoscale structures in a fluidized bed. It can be seen that with decreasing grid size, more and more details of the flow field appear, in agreement with results of other groups (Agrawal et al., 2001; Loezos & Sundaresan, 2005). However, whether or not grid size smaller than that of mesoscale structures can be successfully resolved is controversial in those studies. Some authors have reported that a grid size of about 10 particle diameters is sufficient to fully resolve the flow structure and obtain a grid-independent numerical solution (Agrawal et al., 2001; Benyahia et al., 2007; Loezos & Sundaresan, 2005), while others suggest that the grid size should be of order 2–4 particle diameters (Wang et al., 2009). A possible reason for the differing conclusions could lie in the fact that their systems operated in different fluidization flow regimes. Further study is needed for clarification.

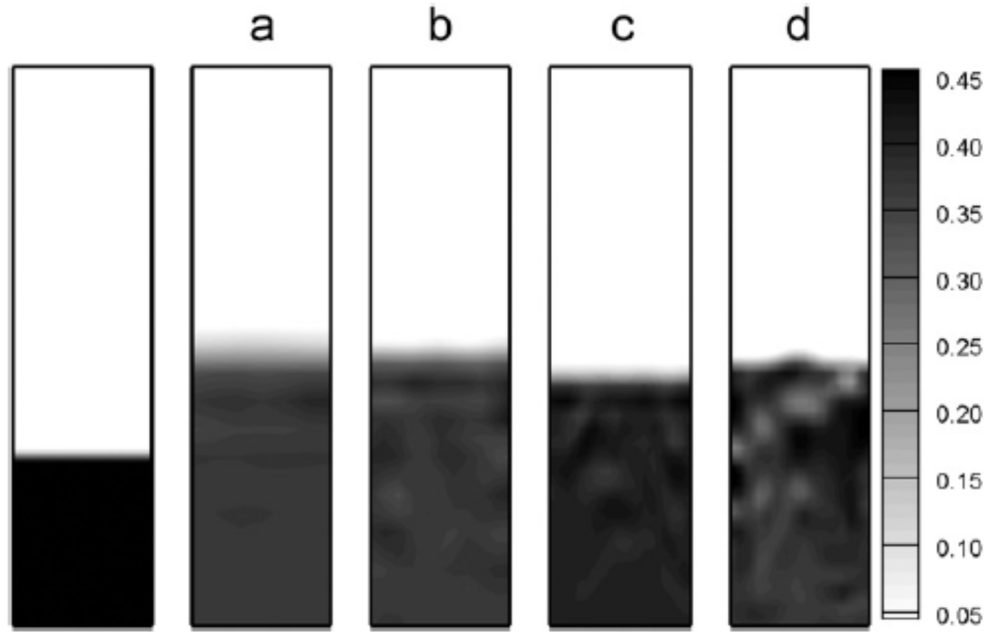


**Figure 1.4** Effect of grid size for the highest gas velocity ( $U = 0.018\text{m/s}$ ). At the far left is the initial bed used in the simulation. The grid sizes are:(a)  $0.5\text{mm}(x)\times 0.2\text{mm}(y)\times 0.6\text{mm}(z)$ , (b)  $0.3\text{mm}\times 0.2\text{mm}\times 0.4\text{mm}$ , (c)  $0.2\text{mm}\times 0.2\text{mm}\times 0.3\text{mm}$ ,and(d) $0.2\text{mm}\times 0.2\text{mm}\times 0.2\text{mm}$ . (Wang et al., 2009).

Researchers have approached the problem of treating small structures through various approximate schemes. Recently, new modeling methods have been developed which account for the effect of mesoscale structures (bubbles and/or clusters) on hydrodynamics through suitable sub-grid-scale (SGS) models for constitutive laws. In a review, Wang (2009) classified available methods for establishing SGS models into six categories: empirical correlation, scaling factor, structure-based, modified drag correlation, Energy Minimization MultiScale (EMMS) and correlative multiscale method. Despite satisfactory results reported by some researchers, empirical correlations, scaling factors and modified drag methods are not generally suitable for operating conditions beyond those for which they were derived. It is difficult to extend them to other systems, and they therefore lose their generality (Wang, 2009). In a structure-based method, it is necessary to adjust the particle diameter in simulations to a diameter larger than the

real diameter of particles, which may be regarded as the diameter of clusters. From this perspective, the fluidized bed does not involve fluidization of individual particles, but of schools of clusters. However, the basic assumption in this method is the existence of clusters in fluidized beds, something which is argued by some researchers to not exist under all conditions in gas-solid fluidized beds (Wang 2009).

The EMMS method, originally developed by Li & Kwauk (1994), assumes that particles move in the form of clusters through a dilute phase composed of the surrounding gas and a few randomly distributed particles. This model is integrated into the Eulerian-Eulerian formalism in the form of a sub-grid drag correction. Clusters are described by 10 parameters, calculated by balance laws and an energy minimization condition (J.-F. Parmentier & Simonin, 2011). Incorporation of the EMMS model into the Eulerian-Eulerian model is similar to that of the scaling factor method discussed above, but now the scaling factor is a variable predicted by the EMMS model. This method has been successful in capturing the effect of mesoscale structures on the transport properties. It has been claimed that the combined EMMS/Eulerian approach can significantly improve the calculation accuracy and the agreement with experimental data (Wang et al. 2008). Records of promising agreement between this approach and experiments were briefly summarized by Wang (2009). Despite the improvement in modeling results using the EMMS/Eulerian approach, tests are required for operating conditions other than circulating fluidized beds, for which the model was originally derived.

In the correlative multiscale method category, a new modeling approach called the Filtered Eulerian Model (FEM) has been developed which accounts for the effect of mesoscale structures (bubbles and/or clusters) on hydrodynamics through suitable sub-grid-scale (SGS) models for constitutive laws (Sundaresan, 2000). This filtered approach is a formalism that

highlights terms in continuum equations that need to be closed when there is no wish to resolve small structures. A similar idea has been applied in single-phase turbulent flow for many years, known as the large eddy simulation (LES) method (J.-F. Parmentier & Simonin, 2011). In this model, all physical variables are grouped into a resolved part and an unresolved part. The resolved part of a variable is the filtered variable, which contains only large-scale structures that can be resolved on a coarse-grid. The unresolved part contains the small scales that cannot be solved on a coarse grid. The continuum equations in the Eulerian model are then rearranged considering the filtered/unfiltered variables. Consequently, new unknown terms appear in the governing equations that need to be closed by highly resolved simulations in small scales (extra-fine meshes). The detailed approach on how to obtain these closures has been outlined by Sundaresan and co-workers (Igci & Sundaresan, 2011; Igci, 2011; Loezos & Sundaresan, 2005; Wang et al., 2011) and the Simonin group (Parmentier, 2010; Parmentier & Simonin, 2011). The most recent work in this category (Igci & Sundaresan, 2011) claims that coarse statistical results obtained by solving the filtered models with different filter lengths were the same and corresponded to those from highly resolved simulations of the kinetic theory model. However, comparison between the outcome of this method and experimental data by the original author showed qualitative agreement only in some regions, and quantitative differences.

In spite of inherent advantages of this method, the procedure to obtain closures for new unknown terms that rely solely on highly resolved simulations needs further improvement to account suitably for the effect of boundaries, and it needs to be numerically verified and validated with experimental results in the future (Wang 2009).

### **1.3.2 Liquid injection (experiments and modeling)**

The effects of feed vaporization and feed-injection configuration have been evaluated in various experimental studies in commercial catalytic cracking reactors and pilot units. There have also been many attempts to simulate entire FCC units, almost all based on the assumption of instantaneous vaporization of feed at the riser entry (Gupta, 2001, 2003). In recent years, attempts have been made to more thoroughly study the mechanism of feed vaporization at the inlet of riser reactors.

Rapid vaporization of liquid droplets in FCC reactors leads to a substantial increase in volumetric gas flow. This can significantly affect gas-solid mixing, temperature distribution, and flow behaviour, and it plays an important role in most applications by affecting process efficiency and product quality (Fan et al., 2001). Liu (2003) conducted experiments to visualize the behavior of evaporating spray jets in dilute gas-solid flows. He measured the temperature distribution of a three-phase mixture near the spray region, which is important for testing the fundamental model of spray jets in gas-solid flows. The experimental results were then utilized to develop a parametric model which includes phase interactions with phase changes. Predictions of this theoretical model were reported to be in good agreement with experimental results.

Research reports have been published of non-evaporative ( Leach et al., 2008; Portoghese, 2007) and evaporative (Du et al. 2006; Gehrke and Wirth 2007) liquid injection experiments using water and liquid nitrogen. Almost all of these studies emphasize the effect of liquid droplet diameter in the injection process. One of the most widely used experimental methods to study liquid dispersion is optical visualization, e.g. by X-ray imaging or Charged-Coupled-Device (CCD) camera recording. This method could provide useful information required to characterize jets in fluidized beds. X-ray imaging is non-intrusive, unaffected by

process conditions and can be used to obtain useful information, such as the jet penetration length and expansion angle. In this method, the pulse-rate frequency of the X-ray beam is synchronized with a video camera, thus ‘freezing’ internal motion and allowing internal flow patterns to be detected and recorded (Bruhns, 2002).

Despite the advantage of X-ray imaging due to its non-intrusive nature, major disadvantages are poor spatial resolution and/or long scan times (Gehrke & Wirth, 2007). Further, the relatively high capital investment required and radiation hazards discourage widespread application of these techniques. Another method uses temperature measurements such as fast response thermocouples, different kinds of probes like suction probes for measuring gas concentrations and capacitance probes for the detection of liquid within the dense gas-solid phase (Ariyapadi 2004). In this method, the evaporation zone corresponds to temperatures near the boiling point (Bruhns & Werther, 2005). Recently, attempts have been made to use a combination of visualization techniques such as X-ray or CCD camera recorders and temperature distribution methods (Bruhns 2002; Gehrke & Wirth 2007).

Electrical capacitance/conductance impedance methods have been utilized as non-intrusive techniques to capture liquid distribution inside fluidized beds (Aidan Leach et al., 2008; Mohagheghi et al., 2013). Despite the possibility of rapid vaporization of liquid feed at the nozzle exit, independent research has disproved the assumption of instantaneous evaporation at the nozzle exit (Gu et al. 1966; Newton et al. 2001; Skouby 1999). The effect of solids concentration on evaporative liquid jets was studied by Zhu et al. (2000). These authors reported that the jet penetration length could be shortened by as much as 45% with a solids concentration of 1.6%, compared to solids-free flow. However, as reported by Bruhns & Werther (2005), these conditions differ significantly from the situation at the injection level of FCC riser-type reactors

where solid volume concentrations are 20–30%. Therefore, more experimental work, in equipment larger than laboratory scale, is required to study the effect of particle concentration on liquid vaporization in FCC reactors.

Among the testing liquids that could be injected in a fluidized bed, water (Bruhns & Werther, 2005) and ethanol (Bruhns, 2002; McMillan et al., 2005; Mohagheghi et al., 2013) have been used to study the contact between liquid droplets and fluidized beds. Bruhns & Werther (2005) injected water and ethanol into fluidized beds of quartz and FCC catalysts on a pilot scale. Based on experimental results, they introduced a new model for the mechanism of liquid injection which assumes instantaneous wetting of the fluidized particles at the nozzle exit and considers the transport of wetted particles by gross solids mixing of the fluidized bed. However, they did not include a detailed comparison between the new model and experimental results.

McMillan et al. (2005) investigated the injection of ethanol into a fluidized bed containing coke particles. They developed a method to determine the local quality of solid liquid mixing on a short time scale. Their measurement technique used temperature to characterize solid-liquid mixing. Mixing was compared for a case where the spray was introduced as a free jet and another case where a draft tube was inserted to promote mixing. Superior mixing was obtained with the draft tube inside the bed.

The effect of particle porosity on liquid-solid mixing inside the bed is a topic of research interest, but there have been few reports on this effect in the literature. Leclere et al. (2001; 2004) developed a method to investigate vaporization of injected liquid inside a fluidized bed based on quenching the bed and creating agglomerates. Emphasizing the effect of liquid droplet size on the time of vaporization, they developed a heat-transfer-based model which predicts the formation of agglomerates when liquid droplets larger than bed particles are injected into a high-

temperature fluidized bed. The importance of the particle porosity was also shown as the experimental data indicated  $> 80\%$  pore filling.

In the context of numerical simulation of liquid evaporation inside fluidized beds, Li et al. (2011) simulated vaporization of liquid feed by investigating three limiting assumptions to simplify the process in a Fluid Coker reactor (which is very similar to FCC reactors in terms of the overall process):

- (a) Liquid feed entirely vaporized at the entrance of the column;
- (b) Liquid feed vaporized immediately upon contact with coke particles;
- (c) Liquid coated uniformly on the particles, with vapor generated uniformly throughout the bed.

Their study reveals that the vaporization rate has a significant impact on the hydrodynamics of the reactor. This complements their previous study on the influence of volume change of the gas phase due to phase change and chemical reactions in the fluidized beds (Li et al. 2010). The temperature was assumed to be uniform in the entire bed for all scenarios studied. Hence, the energy equation was not solved in their system. In addition, agglomeration and associated phenomena were not considered directly.

The effect of nozzle geometry was studied numerically by Pougatch et al. (2012) and Pougatch et al. (2009) who developed a model that resolves the flow through the nozzle, fluidization and droplet-particle interactions. This model showed good agreement with experimental data, but requires high grid resolution in the nozzle and its vicinity that is not practical for large-scale modeling applications. Agglomeration during liquid injection into fluidized beds was studied numerically by Darabi (2011) who considered the effect of both capillary and viscous forces to determine whether or not agglomerates can form.

The proportion of models proposed for liquid injection in fluidized beds that take particle porosity into account is low. More recent models have been developed which do take into account the effect of porosity on liquid distribution (Terrazas-Velarde et al. 2011). Utilizing these models in CFD simulations can improve understanding of the mechanism of liquid distribution inside fluidized beds.

#### **1.4 Summary**

Concluding the research history on hydrodynamic simulations and liquid injections in fluidized beds containing Geldart A particles, the following gaps which require further study are:

- The often-reported failure of two-fluid simulations, incorporating conventional drag models, to capture correct hydrodynamic behavior of fluidized beds containing Geldart A particles is a critical issue. Obtaining a drag correction model which is independent of operating conditions is highly desirable.
- Liquid distribution and vaporization inside a bed containing porous particles is a complex process which has recently been subject to a few experimental and modeling studies. Much effort is needed to understand the underlying mechanism of liquid distribution in fluidized beds containing porous particles, and there is a need to test and improve existing imbibition and evaporation models in CFD simulations, comparing where possible with experimental results.

#### **1.5 Objectives of this thesis**

1- To develop a new drag-correction model to correctly capture hydrodynamics in fluidized beds containing Geldart A (e.g. FCC) particles:

- In view of the profound effects of mesoscale structures on the hydrodynamics of FCC reactors, new hydrodynamic models are required to improve predictions in these reactors. Chapters 2 and 3 are dedicated to development and testing of a new structure-based, subgrid-scale model which can suitably capture the effect of the mesoscale structures and improve CFD predictions of hydrodynamics in gas-solid fluidized beds. The aim is to eliminate the need for scaling/empirical factors that depend on operating conditions.

2- To perform liquid injection experiments in order to understand the mechanism of liquid distribution inside fluidized beds:

- The mechanism of liquid vaporization inside FCC reactors in terms of particle wetting and vaporization is still not sufficiently understood. Distribution of liquid injected into in a fluidized bed was studied using an experimental setup at Western University. Details are presented in Chapter 4.

3- To develop a new approach to perform CFD simulations, utilizing existing models, to study liquid penetration into particle pores, liquid distribution and evaporation inside fluidized beds, and to compare model predictions with experimental data:

- CFD modeling can improve understanding of liquid injection and distribution inside fluidized beds. If a CFD model can be proven to be suitable for capturing the wetting characteristics inside a fluidized bed, it can be further utilized for design and troubleshooting of new or existing units. Chapter 5 is dedicated to numerical modeling of liquid distribution in fluidized beds utilizing existing models, with modifications to more fully capture the physics of the experiments, which are implemented in CFD to study the liquid distribution.

The work presented in this thesis and recommendations for future work are summarized in Chapter 6.

## Chapter 2: Force-Balance (FB) Model

### 2.1 Background

The most widely used particles in industrial catalytic gas fluidized beds are fluid catalytic cracking (FCC) catalyst particles. These are group “A” particles in the Geldart (1973) classification scheme. The design and scale-up of these fluidized beds particles require understanding of the hydrodynamic characteristics, as captured by computational fluid dynamics (CFD). Numerical models describing the flow behavior of gas-solid mixtures can be classified as Eulerian-Eulerian, Eulerian-Lagrangian and Eulerian-Lagrangian Hybrid, based on the framework in which they are developed. Eulerian-Eulerian two-fluid modeling (TFM) has been utilized widely to simulate gas-solid fluidized beds (e.g. Tsuji et al. 1998; Zhang 2002; Gidaspow et al. 2004; Wang & Li 2007; Wu et al. 2009; Liu & Xu 2009; Vejahatiet al. 2009; Chalermssinsuwan et al. 2011). Treating each phase as a continuum in this method, rather than tracking each particle individually, enables modeling of lab-scale or larger fluidized beds. In spite of their advantages, these models require closure equations which can intensify the complexity of modeling fluidized bed systems and contribute to inaccuracies.

While successful TFM studies have been reported on Group B and D particles (e.g. Parmentier et al. 2008, Kashyap & Gidaspow 2011), numerous shortcomings in hydrodynamic predictions of conventional TFM models on Geldart Group A particles have been reported (e.g. Zimmermann and Taghipour 2005; Luand Gidaspow 2003; Taghipour et al. 2005). Formation of agglomerates or clusters in and above a fluidized bed of FCC catalyst particles is believed to be a major cause of inaccuracies in modeling, suggesting that hydrodynamic factors may not be solely responsible for cluster formation, with cohesive forces, such as electrostatic, capillary and van der Waals forces, also playing a significant role (Cocco et al. 2010). Note that a group of

particles brought together by hydrodynamic factors is referred to here as a “cluster”, whereas a group of particles held together by inter-particle forces (e.g. van der Waals forces) is denoted an “agglomerate” (Lewis et al., 1992).

The exact cause of the shortcomings of CFD models for group A materials is not fully understood, but tentative reasons and different modifications have been proposed. In addition to research groups who claim that inter-particle cohesive (e.g. van der Waals) forces result in sub-grid scale heterogeneous structures which take the form of agglomerates or clusters (Gao et al. 2008; van Wachem & Sasic 2008), other groups (Igci et al., 2008; Wang et al., 2009; Wang et al., 2011) claim that inter-particle cohesive forces are not the dominant factor. They propose instead that the under-performance of two-fluid models is primarily due to the grid sizes and time steps in previous studies being too coarse to fully resolve the mesoscale structure, which is between micro and macroscale, including bubbles, clusters and agglomerates.

Most approaches rely on Sub-Grid-Scale (SGS) models to account for these mesoscale structures in Eulerian-Eulerian models. These have been well reviewed by Wang (2009), with the available methods for establishing SGS models classified into six categories: empirical correlation, scaling factor, modified drag correlation, EMMS-model-based, correlative multiscale method and structure-based. The modified drag methods, empirical correlations and scaling factors all modify the drag equation to account for heterogeneous structures. They are generally only suitable for specific operating conditions, so their application is limited.

A correlative multiscale modeling approach, called the filtered Eulerian-Eulerian model, (Sundaresan, 2000; Wang, 2009) accounts for the effect of mesoscale structures (bubbles and/or clusters) on hydrodynamics through sub-grid-scale (SGS) models for constitutive laws. This filtered approach is a formalism that highlights terms in continuum equations that need to be

closed when there is no wish to resolve small structures. This approach has been studied by several researchers (Agrawal et al., 2001; Igci & Sundaresan, 2011; Igci, 2011; Loezos & Sundaresan, 2005). Igci & Sundaresan (2011) reported that coarse statistical results obtained by solving the filtered models with different filter lengths were the same as those from highly resolved simulations of the kinetic theory model. Comparison of the outcome of this method and experimental data (Igci & Sundaresan, 2011) showed qualitative agreement in some regions, but quantitative differences indicate that challenges remain.

The Energy Minimization Multi-Scale (EMMS) method, developed by Li and Kwauk (1994), determines parameters related to the dense and dilute phases by satisfying a stability condition that minimizes mass-specific energy consumption for suspending and transporting particles. It is then incorporated in an Eulerian-Eulerian model to alter the drag calculations, similar to scaling factor methods, but with the scaling factor predicted by the EMMS model. The cluster-based EMMS model has been claimed to significantly improve the accuracy and agreement with experimental data (Benyahia, 2012; Wang et al., 2008). This model is under continuous development. Recently, a bubbling-based EMMS was introduced which is claimed to be more accurate for modeling the bubbling fluidization flow regime (Shi et al., 2011), as well as other flow regimes (Hong et al., 2013).

In structure-based methods, it is necessary to adjust the particle diameter to a diameter larger than the diameter of individual particles. The larger diameter may be regarded as the diameter of clusters (Wang, 2009). One of the first such works (Arastoopour & Gidspow 1979) treated the fluidized bed as a collection of clusters of uniform size. Taking into account the cohesive force, van Wachem & Sasic (2008) utilized the force-balance approach of Zhou & Li

(1999, 2000) to derive an approximate model, taking into account van der Waals and collisional, as well as drag and gravity, forces. They utilized a balance between these forces to estimate the size of local agglomerates in the bed and incorporated it into the continuum (kinetic theory) description of the solid phase. Mckeen & Pugsley (2003a) multiplied the Gibilaro et al. (1985) drag coefficient by an empirical factor of 0.2 to 0.3, to account for agglomerates. They applied the modification to simulate a cold stripper in a subsequent study (Mckeen & Pugsley 2003b).

Gidaspow and Lu (1998) incorporated an empirically-determined cohesive pressure into the term representing the particle pressure, resulting in higher predicted particle pressure compared to that obtained by the kinetic theory of granular flow for non-cohesive particles. In another study (Ye et al., 2005), the kinetic theory approach was modified by adding an excess compressibility term to account for cohesion between particles. These models contain a number of empirical constants whose magnitude is not always clear, restricting their application to different fluidized bed systems.

Electrostatic phenomena in particle handling related processes are complex and unpredictable (Lacks, 2012). There have been recent attempts to include electrostatics in hydrodynamic simulations (Rokkam et. al, 2010; Jalalinejad, 2013), but the requirement of future experimental work to confirm the effects of electrostatics is stressed (Jalalinejad, 2013). Due to complexities and uncertainties, electrostatic forces are not studied in this work, but van der Waals forces are included. A structure-based model is provided which avoids empirical factors or parameters that depend on operating conditions. Details of this new model are presented in the next sections. Two simulation case studies are provided which test the ability of the model to capture the hydrodynamics in fluidization of Geldart Group A particles.

## 2.2 Model description

The approach followed here uses an idea similar to that of van Wachem & Sasic (2008) to derive a non-empirical, structure-based model which predicts the formation of agglomerates in gas-solid fluidized beds and modifies the drag term accordingly. The Kinetic Theory of Granular Flow (KTGF) is utilized, instead of an elastic assumption, to calculate the collisional force. The basis of this approach is a force balance over the control volume for two particles of the same size colliding with each other (Fig. 2.1). The forces considered are collisional ( $F_c$ ), van der Waals ( $F_{vw}$ ), gravity ( $F_g$ ) and drag ( $F_d$ ).

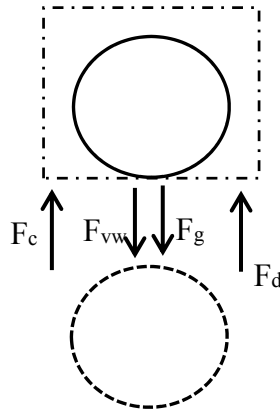


Figure 2.1 Schematic of force balance model.

### 2.2.1 Drag force ( $F_d$ )

In a system containing numerous particles, such as a fluidized bed, the drag forces acting on particles are affected by the voidage. For drag, the force acting on particles in a computational cell inside a fluidized bed can be represented for low Reynolds numbers (Khan & Richardson 1990; ANSYS Inc. 2011; Wen & Yu 1966) by:

$$\vec{F}_d = C_d \frac{1}{2} \rho_g \varepsilon_g |\vec{V}_g - \vec{V}_s| (\vec{V}_g - \vec{V}_s) \frac{\pi}{4} d_p^2 \varepsilon_g^{-2.65} \quad \text{Eq.2.1}$$

where  $\rho_g$  is the gas density,  $\varepsilon_g$  the voidage,  $V_g$  and  $V_s$  are the gas and particle velocities,  $d_p$  the particle diameter and  $C_d$  is the drag coefficient based on the Wen and Yu (1966) correlation (ANSYS Inc., 2011):

$$C_d = \frac{24(1+0.15(\varepsilon_g Re_p)^{0.687})}{\varepsilon_g Re_p} \quad \text{Eq.2.2}$$

with the particle Reynolds number defined as:

$$Re_p = \frac{d_p \rho_g |\overline{V_s} - \overline{V_g}|}{\mu_g} \quad \text{Eq.2.3}$$

The original particles and agglomerates that form based on the force balance approach are all treated as if they are spherical. Agglomerates are assumed to form a single non-porous solid spherical particle. When the agglomerates are formed, two types of voidage appear through which the gas could flow. The space between the particles in each agglomerate creates internal voidage, whereas the outer space surrounding the agglomerates constitutes the external voidage through which interstitial gas passes. Both types of voidage can affect the drag force on agglomerates. The effect of external voidage, which creates space for interaction between particles/agglomerates and surroundings in a fluidized bed, is taken into account in calculation of drag force in Eq. 2.1 by the factor  $\varepsilon_g^{-2.65}$ . The internal voidage allows some gas to flow through the agglomerate, hence reducing the drag force. Neal et al. (1973) proposed a factor  $\Omega$  to account for the effect of the interior flow through the porous structure in reducing the drag force.  $\Omega$  is defined as the ratio of hydrodynamic resistance experienced by a permeable sphere to hydrodynamic resistance experienced by an impermeable sphere of the same radius (Neal et al., 1973). Using the Brinkman's extension of Darcy's law for low Reynolds numbers,  $\Omega$  can be derived (Neal et al., 1973) as:

$$\Omega = \frac{2\gamma^2 \left(1 - \frac{\tanh \gamma}{\gamma}\right)}{2\gamma^2 + 3 \left(1 - \frac{\tanh \gamma}{\gamma}\right)} \quad \text{Eq.2.4}$$

where  $\gamma$  is given (Sutherland & Tan, 1970; Veerapaneni & Wiesner, 1996) by:

$$\gamma = \frac{d_a}{\left(2 \sqrt{\frac{d_p^2}{72} \left[3 + \frac{4}{1 - \varepsilon_i} - 3 \sqrt{\frac{8}{1 - \varepsilon_i} - 3}\right]}\right)} \quad \text{Eq.2.5}$$

Here  $d_a$  is the agglomerate diameter and  $\varepsilon_i$  is the internal porosity. Fig. 2.2 shows the changes in  $\Omega$  with internal porosity for three values of  $\varepsilon_i$  and a particle diameter of 100  $\mu\text{m}$ . For small agglomerates ( $d_a < 6d_p$ ), it is seen that the drag correction factor starts to decrease when the internal voidage exceeds 0.5. However, when agglomerates grow in size, the drag correction factor does not show a sharp decrease with increasing internal voidage, except at higher  $\varepsilon_i$ .

Depending on the arrangements of particles in an agglomerate, the internal voidage could vary considerably. There is no definitive approach to determine how the particles would aggregate to build agglomerates in a fluidized bed. Considering particles and agglomerates to be spherical and utilizing a random style of particle packing, the voidage inside the packing is likely to be between about 0.4 and 0.5, close to random loose-packed values (Jaeger & Nagel, 1992). For these values, the drag correction factor,  $\Omega$ , is very close to 1.0 implying negligible reduction in drag force as a result of flow through internal pores.

Recent numerical study on the effect of Reynolds number (based on particle diameter, gas properties and superficial gas velocity) on drag reduction factor in a particle aggregate, consisting of four particles, show that the flowrate of gas through the internal voidage increases to a considerable extent for Reynolds numbers greater than 10 (Xiao et al. 2013). However, referring to Fig. 2.2, when the agglomerates grow in size, there is more resistance to flow

through internal pores, resulting in less drag reduction. The drag reduction factor caused by the effect of internal porosity in this work is assumed to be unity ( $\Omega = 1$ ), which is appropriate for low particle Reynolds numbers and large agglomerates as described above. The voidage referred to in the next sections of this work is the external voidage. Due to complexities in different possible arrangements of particles in an agglomerate, internal void space between particles is not considered in this study. For simplicity, the agglomerate density is assumed to be identical to the primary particle density.

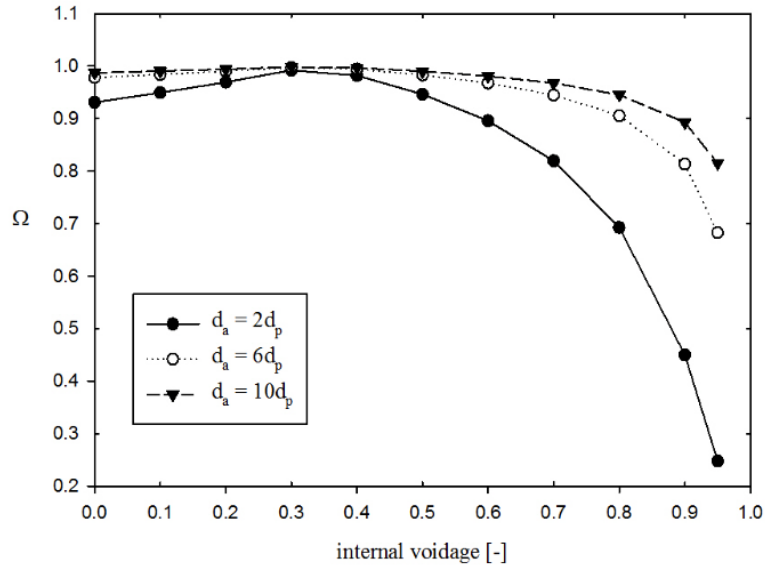


**Figure 2.2 Plot of drag force correction factor ( $\Omega$ ) vs. internal voidage ( $\epsilon_i$ ) for three different agglomerate diameters with  $d_p = 100 \mu\text{m}$  using Brinkman's extension of Darcy equation for low Reynolds numbers.**

### 2.2.2 Collisional force ( $F_c$ )

For two particles colliding with each other (see Fig. 2.1), conservation of total momentum yields:

$$m_1 \vec{V}'_1 + m_2 \vec{V}'_2 = m_1 \vec{V}_1 + m_2 \vec{V}_2 \quad \text{Eq.2.6}$$

$$m_1 \vec{V}_1 = m_1 \vec{V}'_1 - \vec{J} \quad \text{Eq.2.7}$$

$$m_2 \vec{V}_2 = m_2 \vec{V}'_2 + \vec{J} \quad \text{Eq.2.8}$$

where indices 1 and 2 correspond to spherical particle number,  $m_1$  and  $m_2$  are their masses,  $\vec{V}_1$  and  $\vec{V}_2$  are their velocities before collision,  $\vec{V}'_1$  and  $\vec{V}'_2$  are the velocities after collision and  $J$  is the impulse of the force exerted by particle 1 on particle 2. After a dissipative collision, part of the energy of the relative motion is lost. Therefore, after contact the relative velocity is only partly restored. The coefficient of restitution,  $e$ , quantifies this phenomenon:

$$e = - \frac{(\vec{V}'_1 - \vec{V}'_2) \cdot \vec{n}}{(\vec{V}_1 - \vec{V}_2) \cdot \vec{n}} \quad \text{Eq.2.9}$$

where  $\vec{n}$  is the normal unit vector between particle centers and the velocity differences. In an Eulerian-Eulerian modeling framework, all particles are assumed to have identical properties. Therefore, the two colliding particles are assumed to have the same diameter and equal velocity magnitudes before collision ( $m_1 = m_2 = m$ ,  $\vec{V}_1 = -\vec{V}_2 = \vec{V}$ ). Combining equations (2.6) to (2.9) and solving for the impulse yields:

$$\vec{J} = m(1 + e)\vec{V} \quad \text{Eq.2.10}$$

Since impulse is defined as the integral of force with respect to time:

$$\vec{F}_c = \frac{\vec{J}}{T_c} \quad \text{Eq.2.11}$$

where  $T_c$  is the particle-particle collision duration, which can be estimated utilizing Hertzian theory (Stevens & Hrenya, 2005):

$$T_c = 3.21 \times \left( \frac{\pi d_p^3 \rho_p}{8 \sqrt{d_p \left( \frac{E}{2(1-\nu)^2} \right)}} \right)^{0.4} |\vec{V}_{imp}|^{-0.2} \quad \text{Eq.2.12}$$

Here  $d_p$  is the particle diameter,  $E$  the Young's modulus,  $\nu$  the Poisson ratio and  $\vec{V}_{imp}$  is the impact velocity which is not available from continuum equations. The granular temperature serves as a substitute for impact velocity, and Eq. 2.12 is replaced by:

$$T_c = 3.21 \times \left( \frac{\pi d_p^3 \rho_p}{8 \sqrt{d_p \left( \frac{E}{2(1-\nu)^2} \right)}} \right)^{0.4} (\sqrt{3\theta})^{-0.2} \quad \text{Eq.2.13}$$

where  $\theta$  is the granular temperature defined by:

$$\theta = \frac{1}{3} |\vec{V}_s'|^2 \quad \text{Eq.2.14}$$

with  $V_s'$  being the fluctuation velocity of the solid phase which replaces  $\vec{V}$  in Eq. 2.10. Finally, the collisional force is obtained by combining Eqs 2.10 to 2.14 and re-arranging:

$$\vec{F}_c = \frac{\vec{J}}{T_c} = 0.052 \pi \rho_p d_p^3 \left( \frac{8 \sqrt{d_p \left( \frac{E}{2(1-\nu)^2} \right)}}{\pi \rho_p d_p^3} \right)^{0.4} (1 + e) \frac{(\sqrt{3\theta})^{1.2}}{|\vec{V}_s|} \vec{V}_s \quad \text{Eq.2.15}$$

### 2.2.3 Gravitational/buoyancy force ( $F_g$ )

The net gravity force, including consideration of buoyancy, is:

$$\vec{F}_g = \frac{\pi}{6} (\rho_p - \rho_g) d_p^3 \vec{g} \quad \text{Eq.2.16}$$

### 2.2.4 van der Waals force ( $F_{vw}$ )

The dominant cohesive force between particles is the van der Waals force, which for two identical smooth spheres can be expressed (Israelachili, 1992) as:

$$F_{vw} = \frac{A d_p}{24\delta^2} \quad \text{Eq.2.17}$$

where  $A$  is the Hamaker constant (related to the type of material) and  $\delta$  is the distance between particle surfaces. The Hamaker constant is a complex function of several material and interstitial

fluid properties (temperature, dielectric constant of particles, index of refraction of particles and Planck and Boltzmann constants, among others). It is generally assumed to be of order  $10^{-19}$  to  $10^{-23}$  J (van Wachem & Sasic, 2008), with values between  $10^{-19}$  and  $10^{-20}$  J common for Geldart Group A particles (Galvin & Benyahia 2013), and a value of  $10^{-19}$  J (Israelachili, 1992) specifically used for FCC catalyst particles as in this study. The Lifshitz theory can also be applied to calculate this constant (Israelachili, 1992).

The distance between adjacent particles ( $\delta$ ) varies during fluidization and has a profound effect on the van der Waals force. The van der Waals force is essentially negligible at moderate or long inter-particle distances, and only significant at short range. During fluidization, particles contact each other at very short range and travel between contacts (moderate distances from each other). Hence cohesion only plays a role when particles are very close to one another, which is why estimates of the minimum separation distances are used when modeling cohesive forces. van Wachem & Sasic (2008) assumed a separation of 3 to 5 nm in their Eulerian-Eulerian modeling. In DEM simulations, a minimum separation distance, arbitrary or based on inter-molecular distance, can be considered to avoid singularity issues. Hou et al. (2012) chose 1 nm as the minimum separation distance, whereas Chen et al. (2008) and Galvin & Benyahia (2013) adopted an inter-molecular distance of 0.4 nm, a value earlier adopted by Rumpf (1990) in estimating cohesive forces. Changing the separation distance in the range between 0.4 and 4 nm results in variation in cohesive forces by a factor of 100, showing the importance of the distance between particles ( $\delta$ ) in calculating the van der Waals force.

Note that surface asperities, as well as their shape and distribution on the outer surface of particles, have a profound effect on cohesive forces because they determine the closest approach

of a pair of particles. Waitukaitis et al. (2011) and Royer et al. (2009) claimed that the effect of short-range attractive interactions drives structure formation and that the average number of particles in a cluster is directly related to the cohesive strength. Rumpf (1990) and Forsyth & Rhodes (2000) developed models for a single hemispherical asperity on the surface of a larger spherical particle interacting with a flat surface. Their model can be easily modified for colliding spherical particles (Galvin & Benyahia 2013). As shown in Fig. 2.3, Chen et al. (2008) studied the van der Waals force between coated Geldart C particles, utilizing the model to account for the effect of guest-particles (coating) on the surface of host particles. They assumed the contact geometry shown in Fig. 2.3 where one “host” particle, with three guest-particles (asperities), interacts with a second particle. This geometry was then utilized to derive an equation for calculating the van der Waals force, taking into account also the effect of guest-particle radius and Surface Area Coverage (SAC) which is the fraction of particle surface occupied by asperities (Chen et al. 2008). In the present work, the same contact geometry shown in Fig. 2.3 and the same approach are followed, but assuming that the guest particles (asperities) residing on the surface of a host particle are hemispherical. The van der Waals force, which accounts for both particle-particle and particle-asperity forces, can be calculated (Chen et al. 2008) by:

$$F_{vw1} = \frac{A}{12Z_0^2} \left[ \frac{3d_{as}d_p}{d_{as}+d_p} + \frac{d_p}{2\left(\frac{H_0}{Z_0}\right)^2} \right] \quad \text{Eq.2.18}$$

where  $Z_0$  is the minimum separation distance, which in this work is set at an inter-molecular distance of 0.4 nm, the same value as used by Galvin and Benyahia (2013) and by Rumpf (1990) as the distance of closest approach between solid surfaces (particles and/or asperities), “ $d_{as}$ ” and “ $d_p$ ” are asperity and particle diameters,  $H_0$  is the particle-particle distance given by:

$$H_0 = \sqrt{(d_p + d_{as})^2 - \frac{1.21}{SAC} d_{as}^2} - d_p \quad \text{Eq.2.19}$$

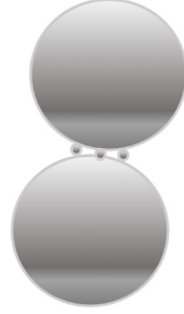


**Figure 2.3 Contact of two-coated cohesive particles and location of guest particles based on Chen et al. (2008).**

SAC is the surface-area-coverage. The total van der Waals force is then:

$$F_{vw} = F_{vw1} + F_{vw\_aa} \quad \text{Eq.2.20}$$

where  $F_{vw\_aa}$  is the van der Waals force magnitude for asperity-asperity contacts. The direction of the total van der Waals force is along the line passing through particle centers and always cohesive. Note that accounting for the van der Waals force between asperities does not affect the distances used to calculate the particle-particle and particle-asperity van der Waals forces in the equation derived by Chen et al. (2008). Hence, the van der Waals force from Eq. 2.18 can still be used to calculate the cohesive forces between particles and particle-asperities. Assuming that each of the three asperities shown in Fig. 2.3 is in contact with asperities close to them,  $F_{vw\_aa}$  for the system portrayed in Fig. 2.3, is given by:

$$F_{vw\_aa} = \frac{3Ad_{as}}{24Z_0^2} \quad \text{Eq.2.21}$$

In order to analyze the effect of asperities on van der Waals forces in Eq. 2.21, a sample case is considered for calculation of the van der Waals force, with results depicted in Fig. 2.4 for different SAC values. The particle-particle van der Waals force dominates on the left-hand

portion of the plot in Fig. 2.4 when the asperities are smaller than 0.02  $\mu\text{m}$ , whereas the particle-asperity and asperity-asperity van der Waals forces dominate on the right side for asperity diameters  $> 0.02 \mu\text{m}$ . Increasing SAC results in slightly less significant particle-particle contact only for large asperity diameters. Otherwise it plays a minor role. Fig 2.4 shows that the asperity diameter has an important influence on the calculated van der Waals forces.

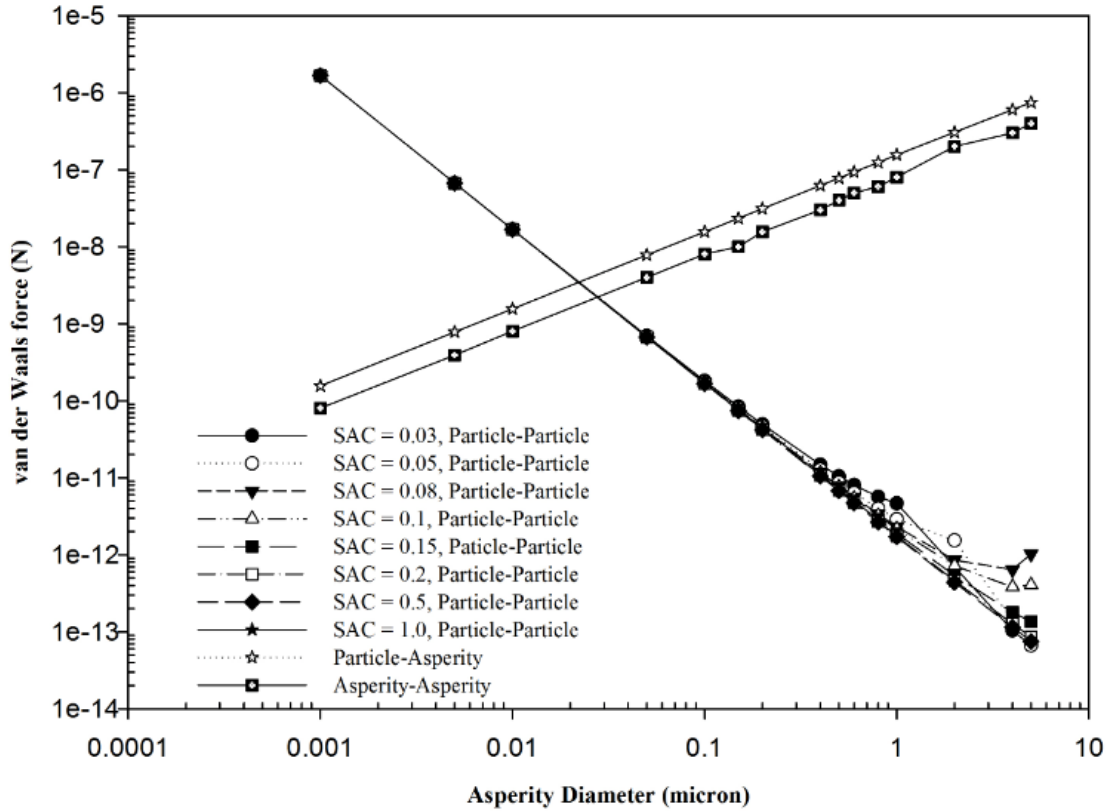


Figure 2.4 Changes of van der Waals force with asperity diameter ( $d_p = 100 \mu\text{m}$ ,  $A = 10^{-19} \text{ J}$ ,  $d = 0.4 \text{ nm}$ , weight of particle =  $8 \times 10^{-9} \text{ N}$ ,  $\rho_p = 1560 \text{ kg/m}^3$ ). Asperity-asperity van der Waals force was calculated

using Eq. 2.21, with particle-asperity from  $\frac{A}{12Z_0^2} \left[ \frac{3d_{as}d_p}{d_{as}+d_p} \right]$  and particle-particle from  $\frac{A}{12Z_0^2} \left[ \frac{d_p}{2 \left( \frac{H_0}{Z_0} \right)^2} \right]$ .

Different values have been reported for asperity radius ranging from 0.1 to 0.5  $\mu\text{m}$  for very small (1  $\mu\text{m}$ ) particles to particle diameters of tens of microns (Galvin and Benyahia 2013;

Xie 1997). In the present study, Scanning Electron Microscopic (SEM) images were captured of typical spent-FCC catalyst particles with a mean particle diameter of 98  $\mu\text{m}$  and density of 1560  $\text{kg}/\text{m}^3$ , the same particles as used in experiments discussed below (Simulation studies: Case I). These FCC catalyst particles have withstood the conditions prevailing in a commercial FCC reactor. Images were taken of particles ranging from 60 to 100  $\mu\text{m}$  in diameter. An interactive MATLAB utility called “Image measurement utility” was utilized to measure the distance between points in SEM images after calibration based on the scale of each image. From the sample pictures of particle surfaces shown in Fig. 2.5 and similar images, it was concluded that asperities cover almost all of the surface of particles (implying Surface-Area-Coverage (SAC) close to 1.0), with asperity diameters ranging from 0.5 to 5  $\mu\text{m}$ , much larger than values previously reported in the literature (Galvin and Benyahia 2013; Xie 1997). Taking the above asperity size range and SAC = 1.0 into account and referring to Fig. 2.4, we see that the magnitude of particle-asperity and asperity-asperity van der Waals forces are much larger than the particle-particle van der Waals force. Therefore, for the FCC particles of interest in this work, the asperity diameter falls into the range of 0.5 to 5  $\mu\text{m}$ , and the particle-particle contribution does not play a significant role in determining the total van der Waals force.

With topographic information, such as asperity diameter and surface-area-coverage, available on particles, Eqs. 2.18 to 2.21 or models proposed by other research groups can be used to estimate the total van der Waals force. However, to simplify the incorporation of these into the FB model, Eq. 2.17 is used to map from the more rigorous cohesion model, which includes the effects of asperities, to the simpler model for smooth surfaces. This mapping is accomplished by taking the cohesive (van der Waals) force at closest approach, and then finding the corresponding separation distance ( $\delta$ ) in Eq. 2.17. Based on this mapping approach for the

particles of interest in this work, the arithmetic mean-average of asperity-asperity and asperity-particle van der Waals forces in Fig. 2.4 is considered for the asperity diameter range of 0.5 to 5  $\mu\text{m}$  to calculate the corresponding separation distance, ( $\delta$ ), between 1.0 and 1.5 nm for particle diameters in the range of 60 to 100  $\mu\text{m}$ :

$$F_{\text{vw}} = \frac{A d_p}{24 \delta^2}$$

$$d_p = 60 \mu\text{m} \rightarrow \delta = 1.0 \text{ nm}$$

$$d_p = 100 \mu\text{m} \rightarrow \delta = 1.5 \text{ nm}$$

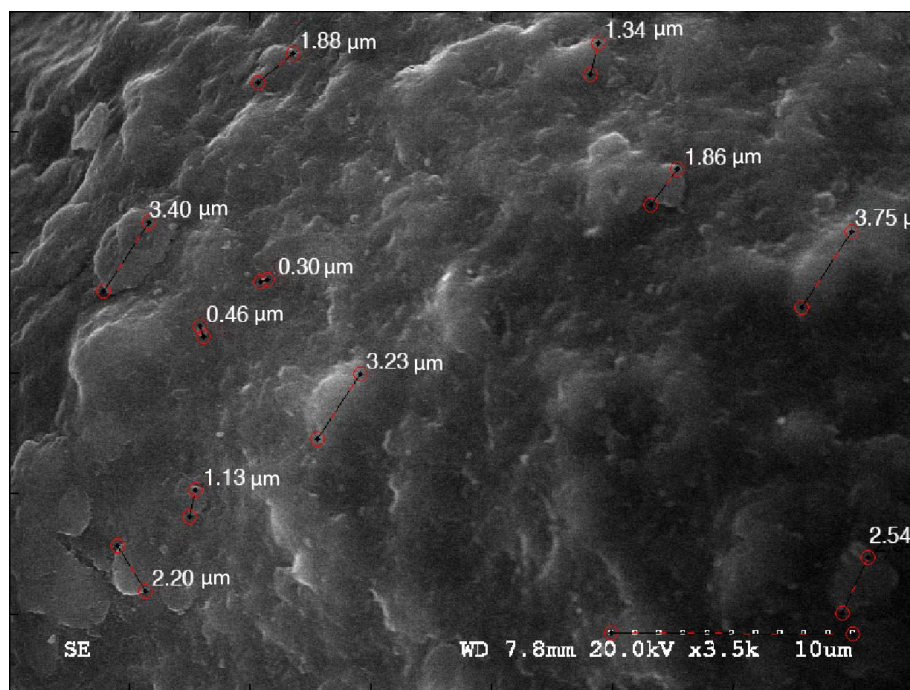
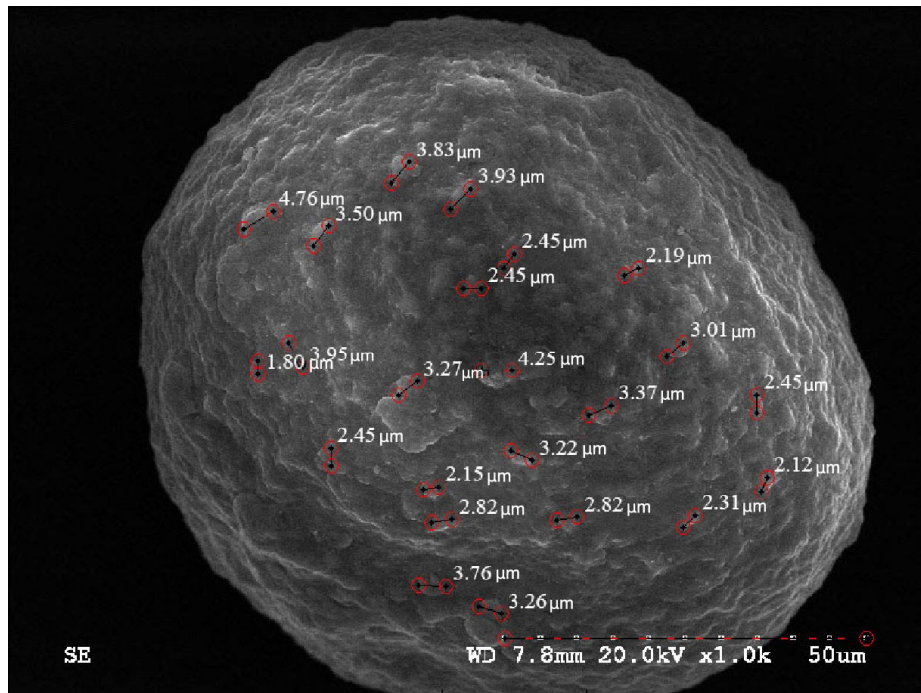


Figure 2.5 SEM images of whole FCC catalyst particles (top) and close-up (bottom) for  $d_p$  of 100  $\mu\text{m}$ .

This simple equation, with the effect of particle asperities included, is then used in “Simulation studies: Case I” below to estimate the van der Waals force.

### 2.3 Analysis of force vectors

Zhou & Li (2000) described agglomerate formation based on a balance of four forces in the form:  $\vec{F}_g + \vec{F}_{vw} = \vec{F}_d + \vec{F}_c$ , with the drag term always on the same side as the collision term. They assumed that wherever  $\vec{F}_g + \vec{F}_{vw} > \vec{F}_d + \vec{F}_c$ , agglomerates cannot disintegrate, instead growing to restore the balance. They further assumed that if the above force balance is not in place, the agglomerates break. A similar approach was followed by van Wachem and Sasic (2008). In the present work, a different approach is adopted where the magnitude of each force vector is calculated and the *direction* of forces analyzed to study the effects of these forces on agglomerate formation. After being formed, agglomerates are assumed to be held together, with the required breakup energy related to properties such as elastic modulus, Poisson ratio and surface energy (Moreno-Atanasio & Ghadiri, 2006). The analysis of agglomerate strength and breakup is a complex issue due to the large number of properties involved and is neglected in the present work. If the balance of forces during collision is not in place, it is assumed that colliding particles or agglomerates bounce back, with no breakup of colliding agglomerates.

Taking into account that the gravity force always acts vertically downward, there are four possible scenarios when considering the vector form of drag, collision, gravity and van der Waals forces, as depicted in Fig. 2.6. Both vertical and horizontal components of these forces are considered when comparing the forces. It should be noted that the direction and size of the vectors in Fig. 2.6 are arbitrary. Given that van der Waals and collisional forces always act in opposite directions, they can be utilized to construct an axis, as shown by the dashed lines in Fig.

2.6. The newly constructed axis between van der Waals and collisional forces and the axis perpendicular to that, the “Reference” axis shown in Fig. 2.6, are selected as the basis for comparison. If any two or three of the forces fall on the same side of the “Reference” axis, their effects are aggregated, whereas if they are on the other side, their effects are considered to be opposite. Forces on the same side of the “Reference” axis as the van der Waals force contribute to agglomerate formation, whereas opposing forces resist formation of agglomerates. This approach for two-dimensional coordinates shown in Fig. 2.6 can be represented, considering the vector form of the forces, by

$$\vec{F} = F_x \cdot \vec{i} + F_y \cdot \vec{j} \tag{Eq.2.22}$$

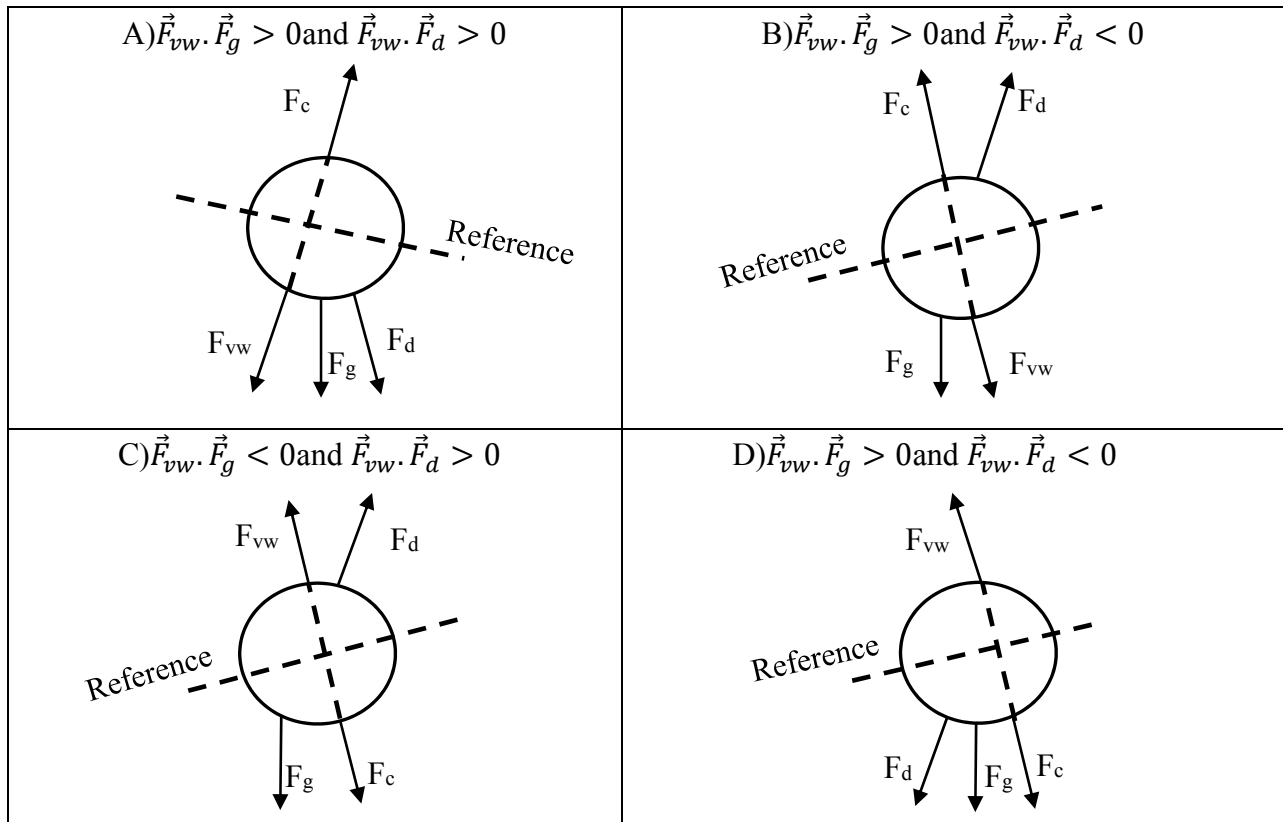


**Figure 2.6 Schematic of possible force scenarios. Each of these scenarios can result in agglomerate formation based on the magnitude and direction of the force vectors.**

The  $F_x$  and  $F_y$  components for each force, calculated utilizing eqs (2.1), (2.15), (2.16) and (2.17) in each computational cell, are shown in Table 2.1. The primary particle diameter is used to calculate van der Waals force, and the agglomerate diameter calculated from the previous time-step is utilized to estimate drag, collision and gravity forces. The dot product between van der Waals force and other forces is then utilized to determine whether the forces in each computational cell reinforce or oppose the van der Waals force with respect to axis “w” in Fig. 2.6. For instance, if  $\vec{F}_{vw} \cdot \vec{F}_g < 0$ , then the van der Waals and gravity forces are on opposite sides of the “Reference” axis, and the possible scenarios could be either case “C” or “D” in Fig. 2.6. If  $\vec{F}_{vw} \cdot \vec{F}_d < 0$  then drag and van der Waals forces are on opposite sides of the “Reference” axis, which leaves case “D” in Fig. 2.6 as the only case. When a scenario is detected, the absolute value of the force vectors are used to determine whether or not an agglomerate can form. If the summation of all forces lying on the same side of the “Reference” axis as the van der Waals force is larger than the summation of all force magnitudes on the other side, then a new agglomerate is assumed to form. Otherwise, no agglomerate formation occurs and the agglomerate diameter calculated in the previous time step is assumed to be conserved for that computational cell. A simplified algorithm for this approach is shown in Fig. 2.7.

## 2.4 Calculation of agglomerate diameter

Based on the possible scenarios depicted in Fig. 2.6, we can write:

$$a_1 d_a^2 + a_2 d_a + a_3 = 0 \quad \text{Eq.2.23}$$

where coefficients ( $a_1$ ,  $a_2$  and  $a_3$ ) are defined in Table 2.2. In this approach, the Reynolds number and other terms which require the agglomerate diameter are treated explicitly in each time step

based on the agglomerate or particle diameter from the previous time step. At the beginning of simulations, the original (non-agglomerated) particle diameter is taken as an initial value, and it is then updated following the algorithm in Fig. 2.7 by solving Eq. 2.23. Particle deformation is ignored during agglomerate formation and the mass of formed agglomerate is taken to be the same as the total mass of the colliding particles. In order to obtain a reasonable estimate of the space filled by the agglomerate for the purpose of drag calculation, the agglomerates are assumed to take the shape of a sphere in 3D simulations or a circular cylinder in 2D simulations. Once the agglomerate diameter has been calculated, the number of primary particles that fit into the agglomerate shape is determined using:

$$\text{a) for a 2D system: } A_{agg\_new} = N_1 \cdot A_{agg\_old} \rightarrow N_1 = \text{roundup} \left[ \left( \frac{d_{agg\_new}}{d_{agg\_old}} \right)^2 \right] \quad \text{Eq.2.24}$$

$$A_{agg\_old} = N_2 \cdot A_p \rightarrow N_2 = \text{roundup} \left[ \left( \frac{d_{agg\_old}}{d_p} \right)^2 \right] \quad \text{Eq.2.25}$$

$$N = N_1 \cdot N_2 \quad \text{Eq.2.26}$$

where  $A_{agg\_new}$  and  $A_{agg\_old}$  are the surface areas of the new agglomerates and the agglomerate at the previous time step, and  $d_p$  is the particle diameter.  $N_1$  is the number of old agglomerates (calculated in the previous time step) that fit inside the newly calculated agglomerate, and  $N_2$  is the number of particles in the agglomerate calculated in the previous time step. Both  $N_1$  and  $N_2$  are then rounded up to the next integer multiple. In this way, the inverse of the number of particles in the new agglomerate ( $1/N$ ) is utilized as a correction factor, accounting for a loose agglomerate size, and it is applied to the conventional Wen-Yu drag term to update the drag function.

b) For a 3D system:

$$V_{agg\_new} = N_1 \cdot V_{agg\_old} \rightarrow N_1 = \text{roundup} \left[ \left( \frac{d_{agg\_new}}{d_{agg\_old}} \right)^3 \right] \quad \text{Eq.2.27}$$

$$V_{agg\_old} = N_2 \cdot V_p \rightarrow N_2 = \text{roundup} \left[ \left( \frac{d_{agg\_old}}{d_p} \right)^3 \right] \quad \text{Eq.2.28}$$

$$N = N_1 \cdot N_2 \quad \text{Eq.2.29}$$

where  $V_{agg\_new}$  and  $V_{agg\_old}$  are the volumes of the new agglomerates and of the agglomerates from the previous time step. The agglomerate diameter, based on  $N$  calculated in Eq. 2.29, is then updated for the next iteration:

$$\text{For 2D system:} \quad d_a = \sqrt{N} \cdot d_p \quad \text{Eq.2.30}$$

$$\text{For 3D system:} \quad d_a = \sqrt[3]{N} \cdot d_p \quad \text{Eq.2.31}$$

The calculated agglomerate diameter is then checked to ensure a physically reasonable value by imposing a condition that the agglomerate volume must not exceed the volume of solid in a computational cell. Otherwise, it is set equal to the volume of the solid phase and the corresponding agglomerate diameter is calculated. This ensures that continuity of the solid phase is taken into consideration in the model.

**Table 2.1 Equations for performing vector calculations**

	$F_x$	$F_y$
$\vec{F}_d$	$0.125\pi C_d \rho_g \varepsilon_g  \vec{V}_g - \vec{V}_s  (\overline{V}_{gx} - \overline{V}_{sx}) \varepsilon_g^{-2.65} d_a^2$	$0.125\pi C_d \rho_g \varepsilon_g  \vec{V}_g - \vec{V}_s  (\overline{V}_{gy} - \overline{V}_{sy}) \varepsilon_g^{-2.65} d_a^2$
$\vec{F}_c$	$0.052\pi \rho_p d_a^3 \left( \frac{4 \cdot \sqrt{d_p} \cdot (E / (2 \cdot (1 - \vartheta^2)))}{\pi \rho_p d_a^3} \right)^{0.4}$ $\times (1 + e)(\sqrt{3\theta})^{1.2} \frac{\overline{V}_{sx}}{ \vec{V}_s }$	$0.052\pi \rho_p d_a^3 \left( \frac{4 \cdot \sqrt{d_p} \cdot (E / (2 \cdot (1 - \vartheta^2)))}{\pi \rho_p d_a^3} \right)^{0.4}$ $\times (1 + e)(\sqrt{3\theta})^{1.2} \frac{\overline{V}_{sy}}{ \vec{V}_s }$
$\vec{F}_{vw}$	$\left( \frac{-Ad_p}{24\delta^2} \right) \frac{\overline{F}_{cx}}{ \vec{F}_c }$	$\left( \frac{-Ad_p}{24\delta^2} \right) \frac{\overline{F}_{cy}}{ \vec{F}_c }$
$\vec{F}_g$	0	$\frac{-\pi}{6} (\rho_p - \rho_g) d_a^3 \vec{g}$

If the agglomerate volume is corrected to the volume of solid phase in the computational cell, then the corresponding agglomerate diameter would be calculated, as well as N1, N2 and N in Eqs 2.24-2.26 or 2.27-2.29. The calculation process is shown in a simplified flowchart in Fig. 2.9. In the computational cells adjacent to the walls, particle-wall collisions occur, as well as particle-particle collisions, but in a different manner. The collisions then take place between moving particles and a stationary wall, with a cohesive force of twice that for the particle-particle contacts (Israelachili, 1992). The mechanism of agglomerate formation near the walls therefore differs from that for particle-particle agglomerate formation described above.

Although the effect of walls on hydrodynamics of lab-scale fluidized beds might be significant, their contribution to the overall hydrodynamics of the system lessens as the reactor

diameter increases. Due to the complexities, the drag term is considered to remain unchanged for the computational cells in the vicinity of the wall ( $N = 1$ ) in the present work.

After each time step and calculation of the agglomerate diameter in each computational cell, it is necessary to trace the movement of agglomerates inside the bed. Only one agglomerate diameter is associated with each computational cell. Tracing the movement of individual agglomerates is not possible here, but changes in agglomerate diameter are traced as agglomerates move from cell to neighboring cells. This is then taken as an approximation of the new agglomerate diameter in each cell at the start of the next time step. For that purpose, solid mass fluxes from neighboring computational cells are considered when calculating the new agglomerate diameter. This approach gives an estimate of “current agglomerate size” based on the agglomerate size and solid fluxes from the previous time step. An example is shown schematically in Fig. 2.8.

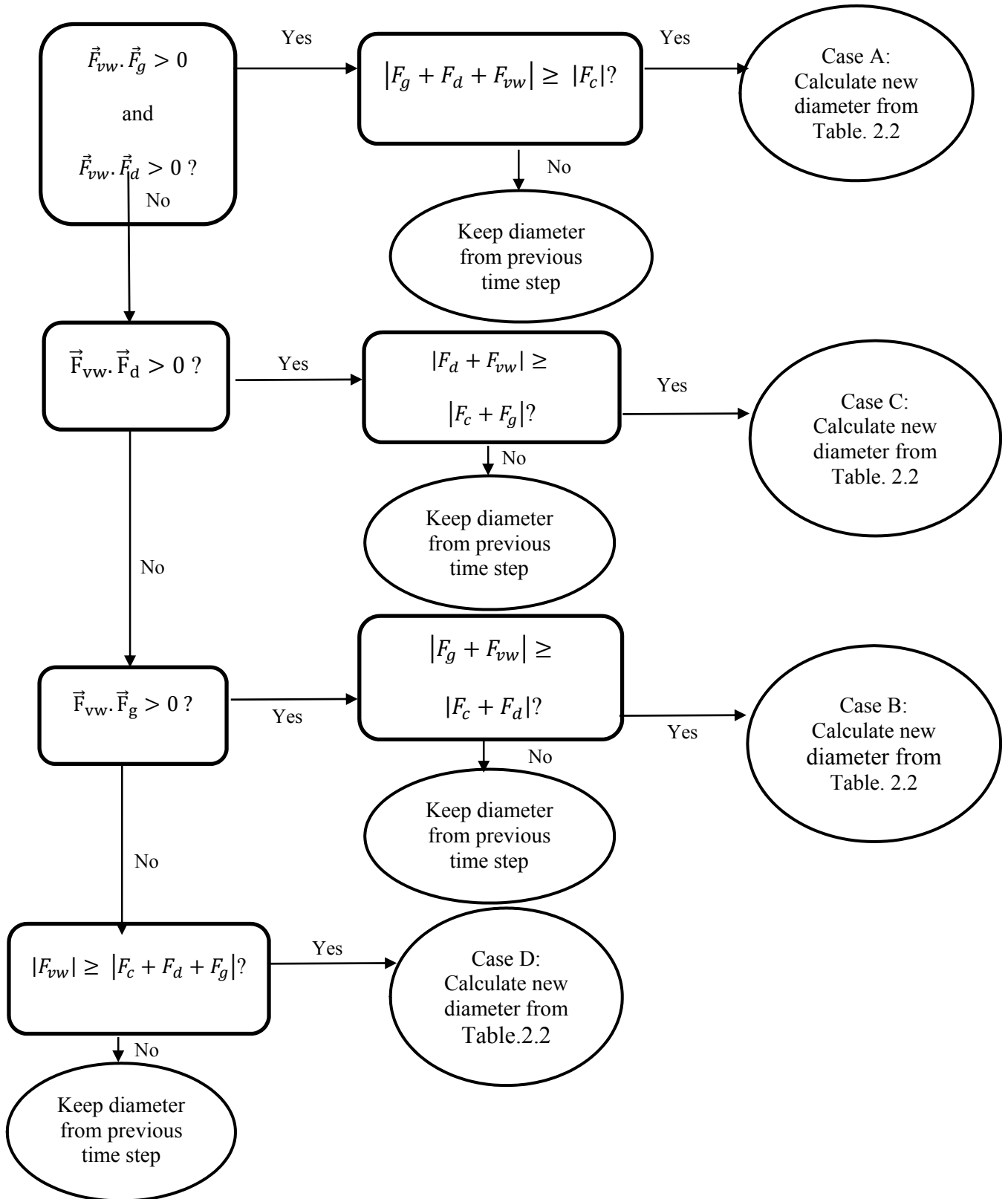


Figure 2.7 Agglomerate diameter calculation procedure repeated in each computational cell.

**Table 2.2 Equations for four possible collision scenarios**

<b>Case A:</b> $(F_d + F_g + F_{vw} = F_c)$	
<b>a<sub>1</sub></b>	$+\frac{\pi}{6}(\rho_p - \rho_g)g - 0.052 \times \pi \rho_p \times \left( \frac{4 \cdot \sqrt{d_p} \cdot (E / (2 \cdot (1 - \theta^2)))}{\pi \rho_p d_p^3} \right)^{0.4} \times (1 + e) \times (\sqrt{3\theta})^{1.2}$
<b>a<sub>2</sub></b>	$+ 0.125\pi \cdot C_d \cdot \rho_g \cdot \varepsilon_g  V_g - V_s ^2 \varepsilon_g^{-2.65}$
<b>a<sub>3</sub></b>	$+\frac{A}{24\delta^2}$
<b>Case B:</b> $(F_g + F_{vw} = F_c + F_d)$	
<b>a<sub>1</sub></b>	$+\frac{\pi}{6}(\rho_p - \rho_g)g - 0.052 \times \pi \rho_p \times \left( \frac{4 \cdot \sqrt{d_p} \cdot (E / (2 \cdot (1 - \theta^2)))}{\pi \rho_p d_p^3} \right)^{0.4} \times (1 + e) \times (\sqrt{3\theta})^{1.2}$
<b>a<sub>2</sub></b>	$- 0.125\pi \cdot C_d \cdot (1 - \varepsilon_g) \rho_g \varepsilon_g  V_g - V_s ^2 \varepsilon_g^{-2.65}$
<b>a<sub>3</sub></b>	$+\frac{A}{24\delta^2}$
<b>Case C:</b> $(F_d + F_{vw} = F_c + F_g)$	
<b>a<sub>1</sub></b>	$-\frac{\pi}{6}(\rho_p - \rho_g)g - 0.052 \times \pi \rho_p d_p^3 \times \left( \frac{4 \cdot \sqrt{d_p} \cdot (E / (2 \cdot (1 - \theta^2)))}{\pi \rho_p d_p^3} \right)^{0.4} \times (1 + e) \times (\sqrt{3\theta})^{1.2}$
<b>a<sub>2</sub></b>	$+ 0.125\pi \cdot C_d \cdot \rho_g \cdot \varepsilon_g  V_g - V_s ^2 \varepsilon_g^{-2.65}$
<b>a<sub>3</sub></b>	$+\frac{A}{24\delta^2}$
<b>Case D:</b> $(F_d + F_g + F_c = F_{vw})$	
<b>a<sub>1</sub></b>	$-\frac{\pi}{6}(\rho_p - \rho_g)g - 0.052 \times \pi \rho_p \times \left( \frac{4 \cdot \sqrt{d_p} \cdot (E / (2 \cdot (1 - \theta^2)))}{\pi \rho_p d_p^3} \right)^{0.4} \times (1 + e) \times (\sqrt{3\theta})^{1.2}$
<b>a<sub>2</sub></b>	$- 0.125\pi \cdot C_d \cdot \rho_g \cdot \varepsilon_g  V_g - V_s ^2 \varepsilon_g^{-2.65}$
<b>a<sub>3</sub></b>	$+\frac{A}{24\delta^2}$

Based on the direction of solid fluxes shown in Fig. 2.8, the inward fluxes from neighboring computational cells #3 and #4, together with the agglomerate diameter in those cells, are used to

calculate the new agglomerate diameter. The value and direction of fluxes are extracted from the CFD solver after each time-step. This approach takes into account the direction of

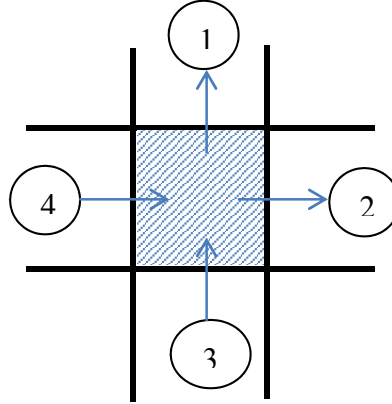


**Figure 2.8 Schematic of solid fluxes from neighboring computational cells for calculation of new agglomerate diameter.**

the flow entering the computational cell from neighboring cells. Therefore, the agglomerate diameter within the hatched cell in Fig. 2.8 is not considered in calculations. Assuming that all computational cells have equal face areas and that the density of the solid does not change, we use the following equation to calculate the average new agglomerate diameter,  $d_{a,new}$ , migrating from neighboring cells in the hatched computational cell in Fig. 2.8:

$$d_{a,new} = \frac{\varepsilon_{s3}V_{s3}d_{a3} + \varepsilon_{s4}V_{s4}d_{a4}}{\varepsilon_{s3}V_{s3} + \varepsilon_{s4}V_{s4}} \quad \text{Eq.2.32}$$

where  $\varepsilon_{s3}$  and  $\varepsilon_{s4}$  are the solid volume fractions in cells #3 and #4,  $d_{a3}$  and  $d_{a4}$  are the corresponding agglomerate diameters, and  $V_{s3}$ ,  $V_{s4}$  are solid velocities in computational cells #3 and #4. Solid fluxes #1 and #2 are not included when calculating the agglomerate diameters in the hatched cell, because they are directed toward neighboring cells. If the face area of the computational cells shown in Fig. 2.8 are unequal, Eq. 2.32 is modified by multiplying each term by the face area of

the corresponding computational cell. This can also be extended to 3D systems and any type of computational grid using the same concept. The new calculated agglomerate diameter is then used in force-balance calculations for the next time step.

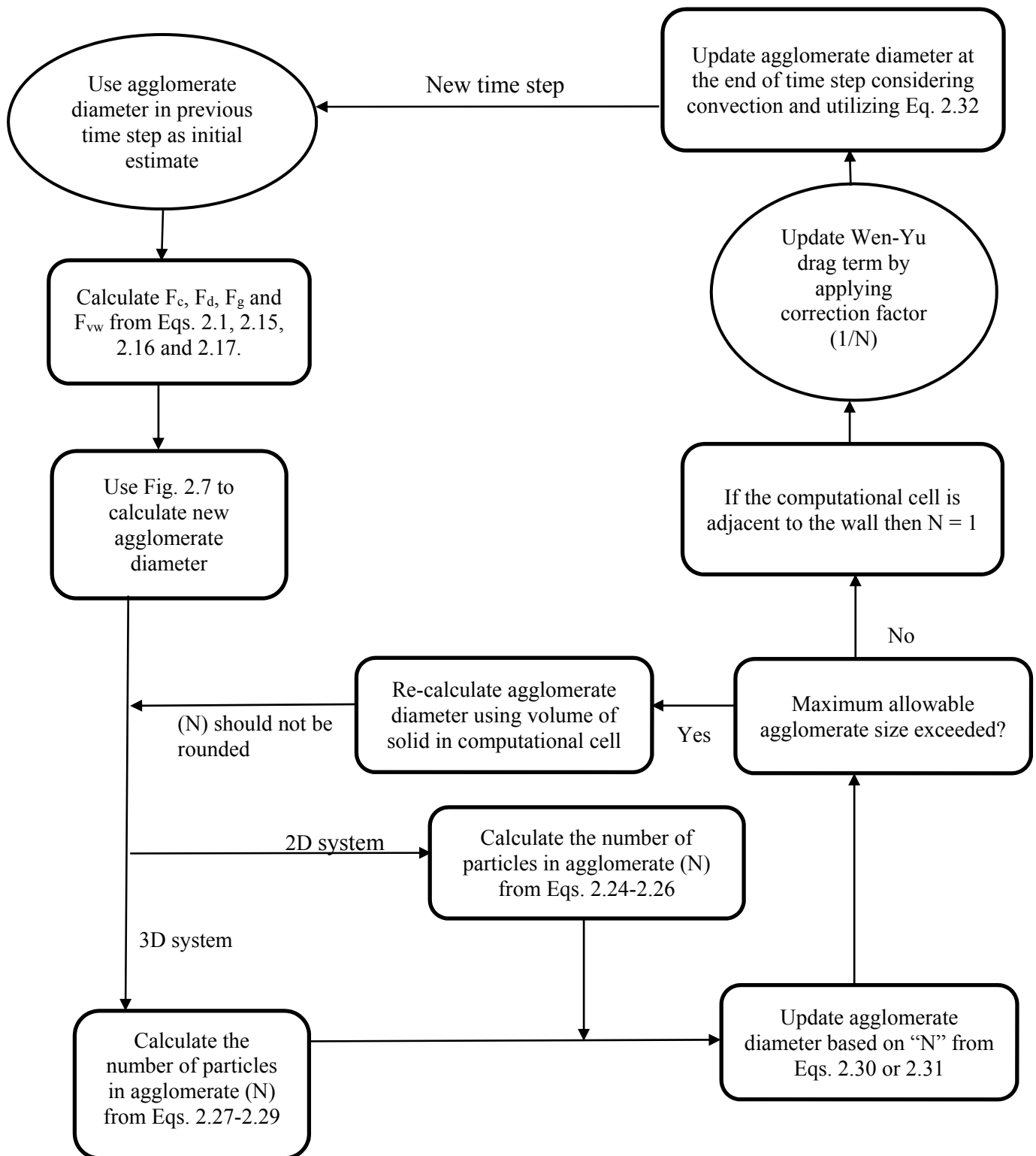


Figure 2.9 Algorithm for calculation of agglomerate diameter.

## 2.5 Summary

A new structure-based model is introduced for modification of the drag term in Eulerian-Eulerian simulations of Geldart Group A particles. It considers a force balance between cohesive (van der Waals), drag, gravity and collisional forces to predict the diameter of agglomerates inside the bed. The novelty of this work is the analysis of direction of force vectors towards finding the agglomerate diameter, and incorporating the effect of particle asperities in the calculation of the van der Waals force. The correction factor calculated by this approach is then applied to the Wen-Yu drag model to correct the drag term. The agglomerate size is accounted for in the drag term only, not in Kinetic Theory of Granular flow (KTGF) closures. A monodisperse KTGF framework is used for simplicity rather than a polydisperse KTGF, to account for a wide range of agglomerate sizes.

Comparison of the modeling results using FB model with experimental data is described in detail in Chapter 3.

## **Chapter 3: Comparison of FB Model Predictions with Experimental Results and Other Models**

The new force-balance (FB) model introduced in Chapter 2 is compared with experimental studies in this Chapter to help determine its accuracy in predicting the hydrodynamics of fluidized beds containing Geldart “A” particles. Three aspects are covered:

- Case I: Fluidization pattern and bed expansion predictions, comparing the conventional Wen & Yu approach with the FB model;
- Case II: Qualitative and quantitative comparisons of hydrodynamic predictions with other existing drag correction models;
- Case III: Prediction of minimum bubbling velocity.

Cases I and II are related to the “traveling fluidized bed” experiments conducted at UBC and other collaborating institutions. The traveling fluidized bed (TFB) column and its auxiliary components were designed to be easily disassembled, transported and remounted, while ensuring identical operation in different locations. Different invasive and non-invasive experimental techniques have been tested in this unit to measure voidage, particle velocity and particle flux. The apparatus details are outlined by Dubrawski et al. (2013). The FCC particles are the same ones as were used for our SEM studies, depicted in Fig. 2.5.

Case III is related to DEM studies by Hou et al. (2012) who measured the minimum bubbling velocity ( $U_{mb}$ ) of spherical Geldart “A” particles.

### **3.1 Case I – Fluidization regime and bed expansion predictions comparing Wen-Yu and FB model**

The failure of two-fluid models (TFMs) to predict correct bed expansion and fluidization regimes is examined in this section. The traveling bed results for FCC catalyst particles of Dubrawski et al. (2013) are chosen as benchmark data for the two-fluid simulations. These authors compared several invasive and non-invasive measurement techniques for voidage measurement at three different superficial gas velocities for FCC catalyst particles.

#### **3.1.1 Simulation setup**

The physical properties and CFD simulation conditions are listed in Table 3.1. In this section, a superficial gas velocity of 0.4 m/s was selected for qualitative study of fluidization pattern and bed expansion. The effect of changing superficial gas velocity is described in section 3.2. Different values have been reported in the literature for the specular coefficient. Li et al. (2010) suggested the optimum value to fall within range of 0.005 to 0.05, in a case where axial gas mixing was predicted by CFD, tending to approach the lower value when the superficial gas velocity increased. Values as high as ~0.5 were reported to be most common in simulating bubbling fluidized beds (Li et al., 2010). In this work, the specular coefficient was set at 0.1, a value reported to give better predictions for FCC catalyst particles (Benyahia, 2012), and the particle-particle restitution coefficient was set at 0.9 (Benyahia, 2012). The effect of particle-wall restitution coefficient was reported to be negligible on hydrodynamic properties in similar studies conducted by Li et al. (2010). Therefore, the same value of particle-particle restitution coefficient was set for particle-wall restitution coefficient. ANSYS Fluent is used for CFD simulations, with a two-dimensional double-precision (2DDP) computational domain.

Convergence criteria of  $10^{-3}$  for the continuity and momentum equations and  $10^{-4}$  for granular temperature are specified for absolute error monitoring. The laminar model is solved for the gas phase using the Phase-Coupled SIMPLE algorithm for pressure-velocity coupling. Second-order upwind discretization schemes are applied for the convection terms, and a time step of  $10^{-4}$  s was found to be suitable to reach convergence, while being small enough to ensure negligible numerical errors.

**Table 3.1 Simulation conditions and physical properties for traveling fluidized bed of Dubrawski et al. (2013) with air as the fluidizing gas.**

<u>Property</u>	<u>Value</u>
Superficial gas velocity	0.3 and 0.4 m/s
Gas density	1.2 kg/m <sup>3</sup>
Gas viscosity	1.8×10 <sup>-5</sup> kg/(m.s)
Mean particle diameter	103 μm
Particle density	1560 kg/m <sup>3</sup>
Column diameter	Lower section: 0.13 m, upper section: 0.18 m
Column height	Lower section: 1.0 m, upper section: 0.55 m
Static bed height	0.8 m
Minimum voidage	0.454
Young's modulus	10 <sup>11</sup> N/m <sup>2</sup> (Petersen et al., 2000)
Poisson ratio	0.2 (Petersen et al., 2000)
Wall Condition	No slip for gas and partial slip for solid (Johnson & Jackson 1987)
Specularity coefficient	0.1
Particle-wall restitution coefficient	0.9
Particle-particle restitution coefficient	0.9

The physical properties, as well as the simulation conditions, are depicted in Table 3.1.

The hydrodynamic model equations adopted in this study are listed in Table 3.2. In the averaging approach used in deriving the equations in Table 3.2, the variables are averaged over a

region that is large compared with the particle spacing but much smaller than the flow domain. The new FB model is utilized to obtain a drag correction factor which is then applied to the Wen and Yu (1966) drag correlation as shown in Table 3.2. Note that the particle diameter, used in the KTGF equations shown in Table 3.2, remains unchanged, with only the calculated agglomerate diameter only utilized to correct the drag term.

For the particle size in this case study, a particle separation distance of 1.5 nm was selected to capture the effect of asperities, consistent with the experimental SEM results described in Chapter 2. The Hamakar constant was set at  $10^{-19}$  J, a common value for FCC catalyst particles (van Wachem & Sasic, 2008; Galvin & Benyahia, 2013; Israelachili, 1992). Simulations were run for a real time of 15 s, which was found to be sufficient for the purpose of this study, since the changes in time-average values were not significant after 15 s. The results were averaged over the last 10 s. Plots of time-averaged void fraction and vertical component of particle velocity were analysed at different heights along the fluidized bed, to check for mesh independency.

Table 3.2 Hydrodynamic equations for gas-solid system

<p><b>Governing Equations</b></p> <p>Conservation of mass for phase m (s: solids and g: gas):</p> $\frac{\partial(\rho_m \varepsilon_m)}{\partial t} + \nabla \cdot (\rho_m \varepsilon_m v_m) = 0$
<p>Conservation of momentum for gas phase:</p> $\left[ \frac{\partial(\rho_g \varepsilon_g v_g)}{\partial t} + \nabla \cdot (\rho_g \varepsilon_g v_g v_g) \right] = -\varepsilon_g \nabla P + \nabla \cdot \tau_g + \beta(v_g - v_s) + \varepsilon_g \rho_g g$
<p>Conservation of momentum for solid phase:</p> $\left[ \frac{\partial(\rho_s \varepsilon_s v_s)}{\partial t} + \nabla \cdot (\rho_s \varepsilon_s v_s v_s) \right] = -\varepsilon_s \nabla P - \nabla P_s + \nabla \cdot \tau_s + \beta(v_s - v_g) + \varepsilon_s \rho_s g$
<p>Granular energy conservation:</p> $\frac{3}{2} \left[ \frac{\partial(\rho_s \varepsilon_s \theta)}{\partial t} + \nabla \cdot (\rho_s \varepsilon_s v_s \theta) \right] = (-P_s \bar{I} + \bar{\tau}_s) : \nabla v_s + \nabla \cdot (k_\theta \nabla \theta) - \gamma_\theta + \varphi_{gs}$
<p><b>Interphase momentum exchange (Drag) term</b></p> <p>FB model (applied to Wen &amp; Yu, 1966):</p> $\beta = \left( \frac{1}{N} \right) \cdot \frac{3}{4} C_D \frac{\rho_g \varepsilon_g \varepsilon_s  v_g - v_s }{d_p} \varepsilon_g^{-2.65}$ $C_D = \begin{cases} \frac{24}{(\varepsilon_g Re)} \left[ 1 + 0.15(\varepsilon_g Re)^{0.687} \right] & Re < 1000 \\ 0.44 & Re > 1000 \end{cases}, Re = \frac{\rho_g \varepsilon_g  v_g - v_s  d_p}{\mu_g}$ <p><b>Constitutive equations for gas and solid phases</b></p> <p>Stress-strain tensor for phase m (s: solids and g: gas):</p> $\tau_m = \varepsilon_m \mu_m (\nabla \cdot v_m + \nabla \cdot v_m^T) + \varepsilon_m \left( \lambda_m - \frac{2}{3} \mu_m \right) \nabla \cdot v_m \bar{I}$

**Table 3.2 Hydrodynamic equations for gas-solid system (continued)**

Solid pressure:

$$P_s = \varepsilon_s \rho_s \theta + 2\rho_s(1+e)\varepsilon_s^2 g_0 \theta$$

Radial distribution function:

$$g_0 = \left[ 1 - \left( \frac{\varepsilon_s}{\varepsilon_{s,max}} \right)^{1/3} \right]^{-1}$$

Solid viscosity model:

$$\mu_s = \mu_{s,col} + \mu_{s,kin}$$

Collision term:

$$\mu_{s,col} = \frac{4}{5} \varepsilon_s \rho_s d_p g_0 (1+e) \left( \frac{\theta}{\pi} \right)^{1/2}$$

Kinetic term:

$$\mu_{s,kin} = \frac{10\rho_s d_p \sqrt{\theta\pi}}{96\varepsilon_s(1+e)g_0} \left[ 1 + \frac{4}{5} g_0 \varepsilon_s (1+e) \right]^2$$

Solid bulk viscosity:

$$\lambda_s = \frac{4}{3} \varepsilon_s \rho_s d_p g_0 (1+e) \left( \frac{\theta}{\pi} \right)^{1/2}$$

Diffusion coefficient:

$$k_\theta = \frac{150\rho_s d_p \sqrt{\theta\pi}}{384(1+e)g_0} \left[ 1 + \frac{6}{5} \varepsilon_s g_0 (1+e) \right]^2 + 2\rho_s d_p \varepsilon_s^2 g_0 (1+e) \left( \frac{\theta}{\pi} \right)^{1/2}$$

**Table 3.2 Hydrodynamic equations for gas-solid system (continued)**

Collisional dissipation of energy:

$$\gamma_{\theta} = \frac{12(1 - e^2)g_0}{d_p\sqrt{\pi}} \rho_s \varepsilon_s^2 \theta^{3/2}$$

Transfer of kinetic energy:

$$\varphi_{gs} = -3\beta\theta$$

**Partial-slip wall boundary condition (Johnson and Jackson 1987):**

Shear stress at wall:

$$\tau_s = -\frac{\pi\phi\rho_s\varepsilon_s v_{sw}g_0\sqrt{3\theta}}{6\varepsilon_{s,max}}$$

Granular temperature at wall:

$$k_{\theta}\nabla\theta = \frac{\pi}{6}\sqrt{3}\frac{\varepsilon_s}{\varepsilon_{s,max}}\rho_s g_0\sqrt{\theta}v_{sw}^2 - \frac{\pi}{4}\sqrt{3}\frac{\varepsilon_s}{\varepsilon_{s,max}}(1 - e_w^2)\rho_s g_0\theta^{3/2}$$

### 3.1.2 Results and discussion

The flow patterns at different times (5, 10 and 15 s) are illustrated in Fig. 3.1 for a superficial gas velocity of 0.4 m/s. As shown, the conventional Wen-Yu model leads to expansion throughout the entire bed. There is no bubble formation, and streams of particles are predicted to leave the system. On the contrary, for the new FB model, the flow pattern shows discrete bubbles rising in the bed, as observed experimentally (Tebianian, 2014) for the operating conditions summarized in Table 3.1.

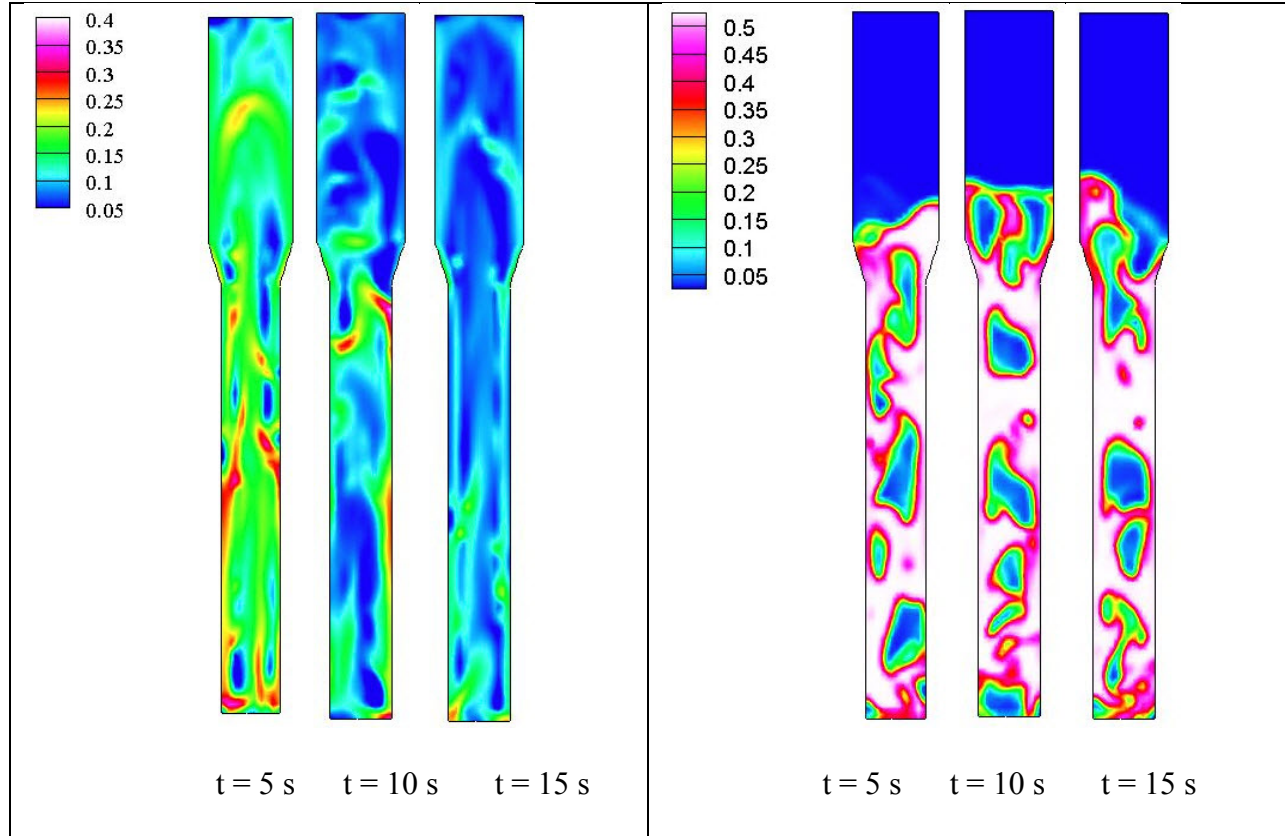


**Figure 3.1 Fluidization pattern showing solid volume fraction at different times with properties in Table. 3.1 for Conventional Wen-Yu drag model (Left) and FB model with Wen-Yu drag model (Right).**

According to Dubrawski et al. (2013), the overall bed voidage for the expanded state for a superficial gas velocity of 0.4 m/s was 0.61. Therefore, the expanded bed height can be estimated from:

$$h_{expanded} = h_{mf} \cdot \left( \frac{1 - \varepsilon_{mf}}{1 - \bar{\varepsilon}} \right) \quad \text{Eq.3.1}$$

where  $h_{mf}$  is the bed height corresponding to minimum fluidization, set equal to the static bed height in Table 3.1,  $\varepsilon_{mf}$  is the voidage at minimum fluidization and  $\bar{\varepsilon}$  is the overall bed voidage equal to 0.61 (Dubrawski et al., 2013). Using the values shown in Table 3.1, the expanded bed height is calculated to be 1.12 m, close to the experimental measured value of about 1.10 m

obtained by visual observation for superficial gas velocity of 0.4 m/s (Tebianian, 2014). The bed expansion predictions from the CFD model were obtained using the time-average solid volume fraction profile, as depicted in Fig. 3.2. The highest point where the transition from dense region (with void fraction ranging from 0.6 to 0.5) to dilute region (with void fraction  $< 0.2$ ) occurs, is taken as the basis for determination of bed expansion. The CFD predicted expanded bed height ( $\sim 1.1$  m in Fig.3.2), using the FB drag model, is almost the same as the calculated expanded bed height and very close to the experimental range. The bed expansion predictions, using the FB model, are compared to experimental results in Table 3.3 for  $U = 0.3, 0.4$  and  $0.5$  m/s. It is shown that a good agreement exists between the experimental data and CFD predictions.

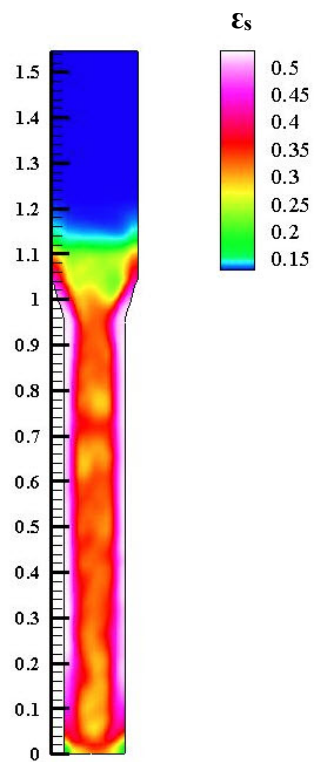


**Figure 3.2 Bed expansion predictions (Y-axis given in meters) by FB model from contour of time-averaged solid volume fraction for  $U = 0.4$  m/s.**

**Table 3.3 Expanded bed height predictions**

U (m/s)	Experiments (m)	FB Model (m)
0.3	1.020	1.037
0.4	1.100	1.098
0.5	1.165	1.175

### **3.2 Case II– Qualitative and quantitative comparison of hydrodynamic predictions with other drag correction models**

The radial profiles of time-average voidage are selected for further comparison with the experimental results of Dubrawski et al. (2013), average values of voidage obtained using different measuring techniques. The time-average voidage data for the same set-up as described in section 3.1 are compared with modeling predictions using different drag models. All the experimental data obtained from Dubrawski et al., (2013), where the detailed local flow structures inside the bubbling fluidized bed of FCC are reported. Experiments were carried out in the same fluidization column, 0.96 m long x 0.133 m ID dense bed section, containing FCC particles, with a median particle size of 103  $\mu\text{m}$  and a particle density,  $\rho_p$ , of 1560  $\text{kg/m}^3$  at superficial air velocities of 0.3-0.6 m/s. The focus of this experimental work was to compare several non-invasive measurement methods (electrical capacitance tomography, X-ray computed tomography, radioactive particle tracking) with invasive techniques (optical probes) for voidage measurement and to highlight the pros and cons of alternative measurement methods.

The numerical work carried out in this section aims to broadly compare the ability of existing drag models to predict the hydrodynamics of Geldart A particles.

### 3.2.1 Boundary and initial conditions

Table 3.4 summarizes the particle properties and operating conditions of the fluidized bed used in the simulations. The mass of solids in the bed was kept constant in this study. A uniform velocity is specified at the inlet. A constant atmospheric pressure boundary condition is employed at the outlet. The no-slip boundary condition is used for the gas phase at the wall, while the partial slip boundary (Johnson&Jackson, 1987) is used to model the solid phase with three different specular coefficients, as listed in Table 3.4. A pressure boundary serves as the outlet of the freeboard with a constant pressure (atmospheric) set. The upper part of the fluidized bed is the freeboard, which makes sure that the particle concentration at the top of the column is negligible. Second order upwind discretization schemes for volume fraction and momentum terms were used. Time steps of 0.0001 and 40 iterations per time step were chosen to achieve numerical convergence. A convergence criterion of  $10^{-4}$  for each scaled residual component was fixed for the relative error between successive iterations. At some time-steps, the solution did not reach full convergence, but was very close to the convergence criteria, The CFD solver continued to the next time-step after 40 iterations. The phase-coupled PC-SIMPLE algorithm was used for pressure-velocity coupling.

**Table 3.4 Input parameters used in the Case II simulation**

Geometry	2D and 3D
Vessel dimension	0.96 m long x 0.133 m id (dense bed section) 1.36m long x 0.190 m id (freeboard section)
Minimum voidage	0.454

**Table 3.4 Input parameters used in the Case II simulation (continued)**

Gas superficial velocity	0.3, 0.4, 0.5 m/s
Gas viscosity	$1.8 \times 10^{-5}$ kg/(m.s)
Gas density	1.2 kg/m <sup>3</sup>
Bed depth	0.80
Particle size distribution	As in Dubrawski et al. (2013)
Sauter mean particle diameter	103 $\mu$ m
Particle density	1560 kg/m <sup>3</sup>
Boundary conditions	Uniform velocity inlet; Pressure outlet; Gas wall : no –slip; Solid-wall: partial slip
Drag models	EMMS-Shi (Shi et al. 2011), EMMS-Hong (Hong et al., 2013), FB (Ahmadi Motlagh et al., 2014)
Gas flow type	Laminar
Simulation time	15s
Time step	0.0001s
Pressure-velocity coupling	SIMPLE
Particle-particle restitution coefficient	0.99
Specularity coefficient	0.001, 0.01, 0.1

### 3.2.2 Data collection and analysis:

2D and 3D CFD simulations were carried out in the Ornicus server of Canada's West Grid computer cluster using the commercial software, ANSYS Fluent V14. The FB drag model

was incorporated using user-defined functions (UDF) in Fluent. The computational domain was created and meshed in ANSYS Workbench.

A schematic of the 2D computational domain is shown in Fig. 3.3. The voidage profiles and velocity distribution were recorded at different heights,  $z = 0.24$  m, 0.4m and 0.56 m and at several radial locations. In order to attain the area-averaged data in 3D simulations, 9 circular rings were made at each cross-section, located at the positions listed above. The voidage of every position was recorded and then averaged over the entire area of each ring. For 2D simulations, the time-average data were extracted along linear cross-sections heights = 0.24 m, 0.4 m and 0.56 m. Simulations lasted for 15s of physical time, with the time-average variables obtained over the last 10 s.

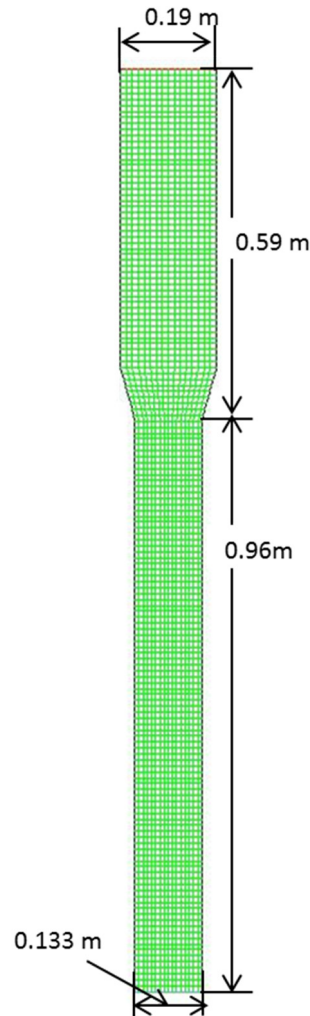


Figure 3.3 Schematic of computational domain (2D).

### 3.2.3 Results and discussion

#### 3.2.3.1 2D-CFD simulation analysis

##### Effect of mesh size

Mesh resolution can affect the simulation results considerably. For Geldart A particles, too coarse a mesh may lead to over-estimation of bed expansion by TFM models(Wang, 2009). In this study, several different mesh sizes were used for 2D simulations, and a noticeable effect was observed on hydrodynamics. This is clearly seen in Fig. 3.4 where refining the mesh from

2480 to 9600 cells not only resulted in contraction of the bed, but also led to prediction of smaller bubbles, which was not expected based on the operating conditions at  $U = 0.4$  m/s and experimental observations of a combination of bubbles and slugs (Tebianian, 2014). After studying the issue in depth, it was observed that when the agglomerate size exceeded the mesh sizes, which is the case for  $> 3900$  cells, the convection mechanism in the FB model which considers movement of agglomerates inside the bed, as described in section 2.4, results in propagation of the large agglomerates formed in some computational cells to a large portion of the bed. This effect results in suppression of drag to very low values over the entire bed which leads to unrealistic bubble sizes and denser regions appearing in the bed. This effect could fade away after some seconds of fluidization, but its effect is significant enough to affect the results. This way, no matter how long the simulations last, the effect will be carried on to the next time-steps. On the contrary, when the agglomerate sizes fall within the range of mesh size, we do not see such behavior in the bed, and agglomerates freely move inside the bed with slight variations in size. Therefore, it is recommended to check the size of agglomerates during 2D simulations to ensure that they fit within a computational cell.

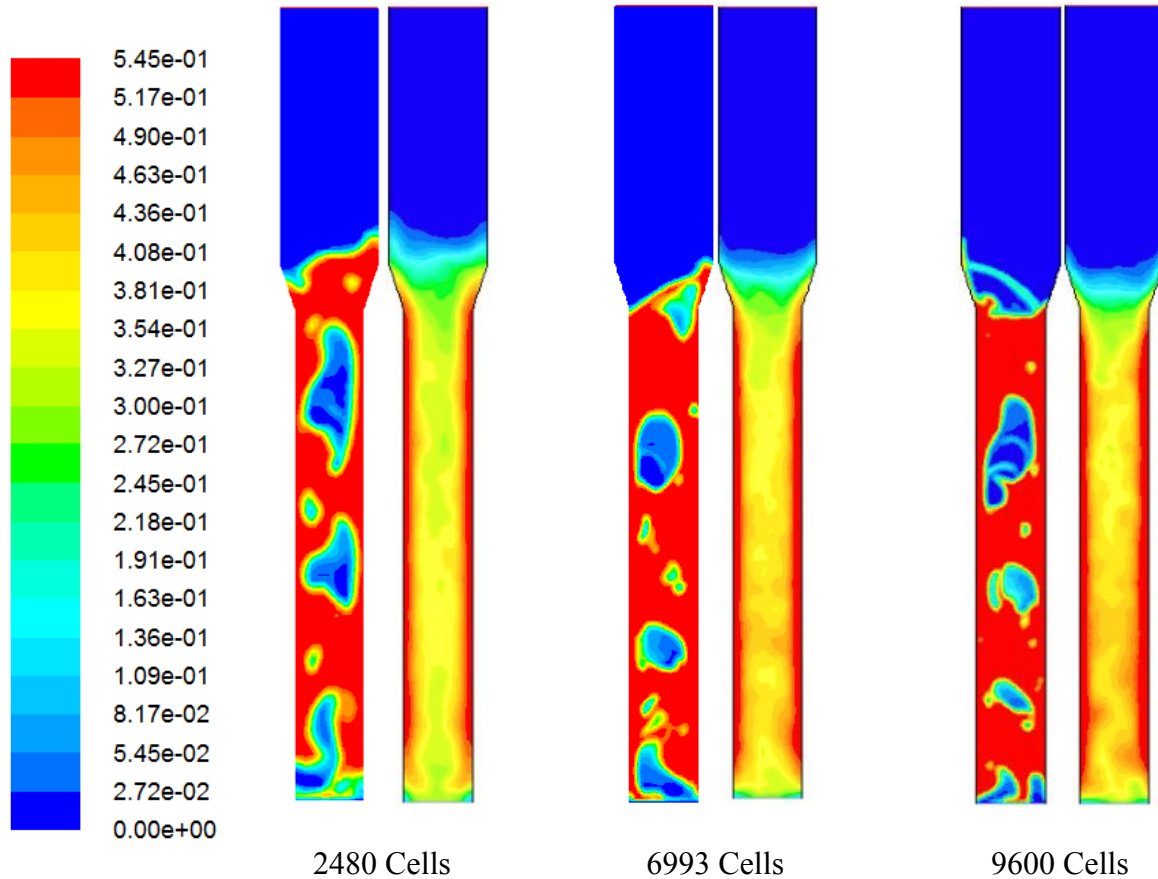


**Figure 3.4** Contours of solid volume fraction at  $U = 0.4$  m/s,  $d_p = 103$  mm,  $\phi = 0.001$ . Left side in each case represents snapshot at  $t=15$  s, whereas right side provides time-average over last 10 s.

Hence, refining the mesh beyond a certain point does not result in more accurate predictions in 2D simulations. In order to select the most appropriate mesh size, both qualitative and quantitative analysis should be considered. Fig. 3.5 shows how the particle velocity changes at certain heights with the number of cells. Mesh numbers greater than 2480 computational cells led to similar results for particle velocity at different locations along the fluidized bed. Combining the results of Figs. 3.4 and 3.5 and considering the expected flow behavior at operating conditions studied here, 2480 cells was selected as the appropriate number of mesh elements for the 2D simulations.

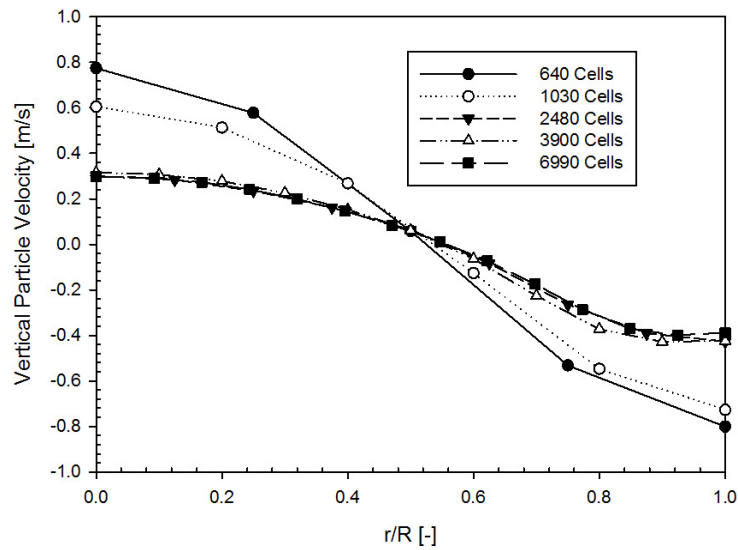
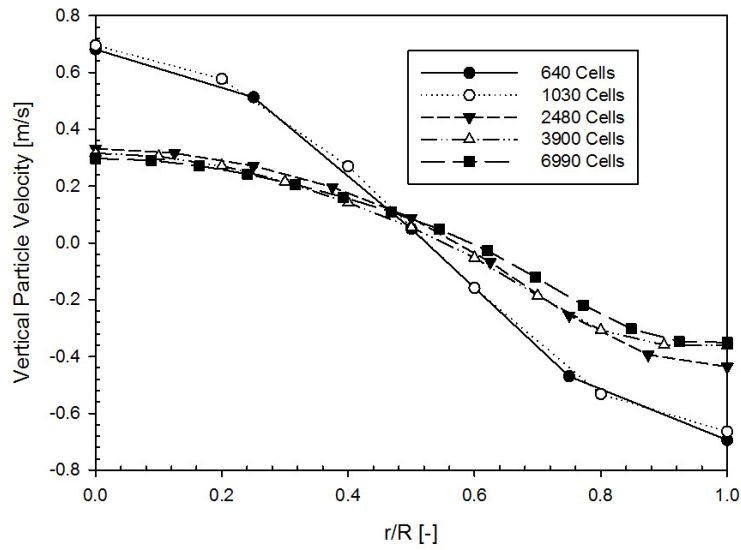
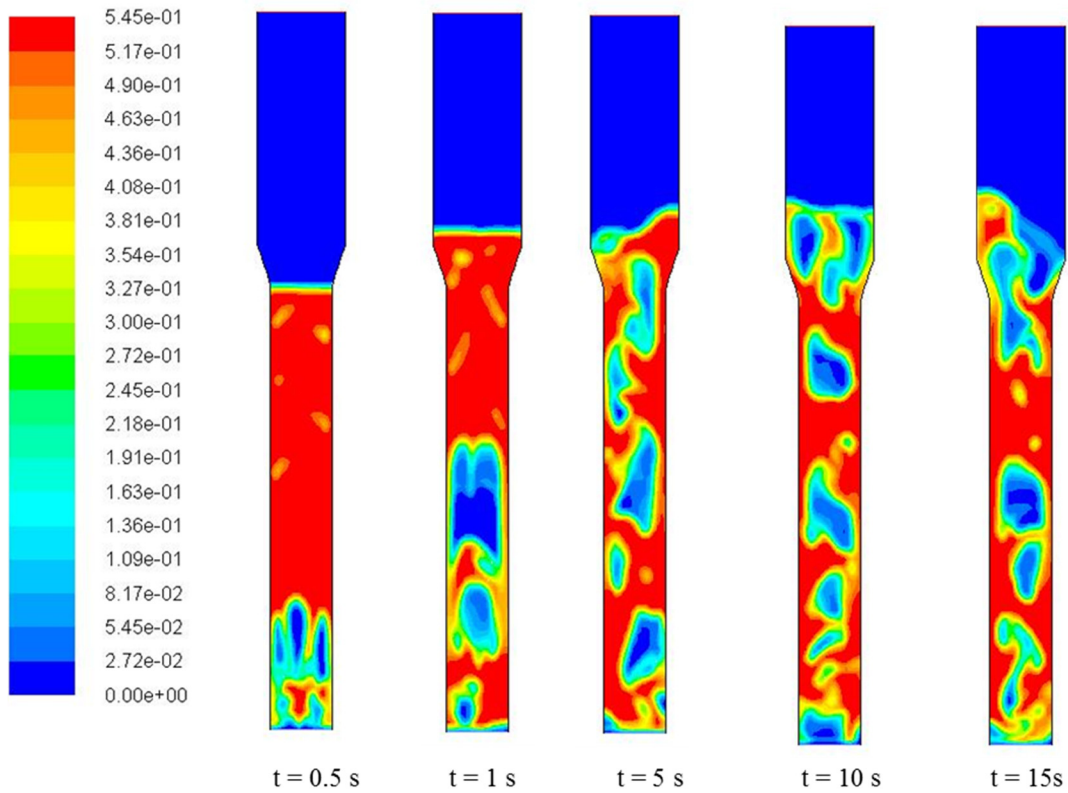


Figure 3.5 Radial profiles of time-average particle velocity at heights of 0.4 m (top figure) and 0.56 m (bottom figure) predicted by FB model.

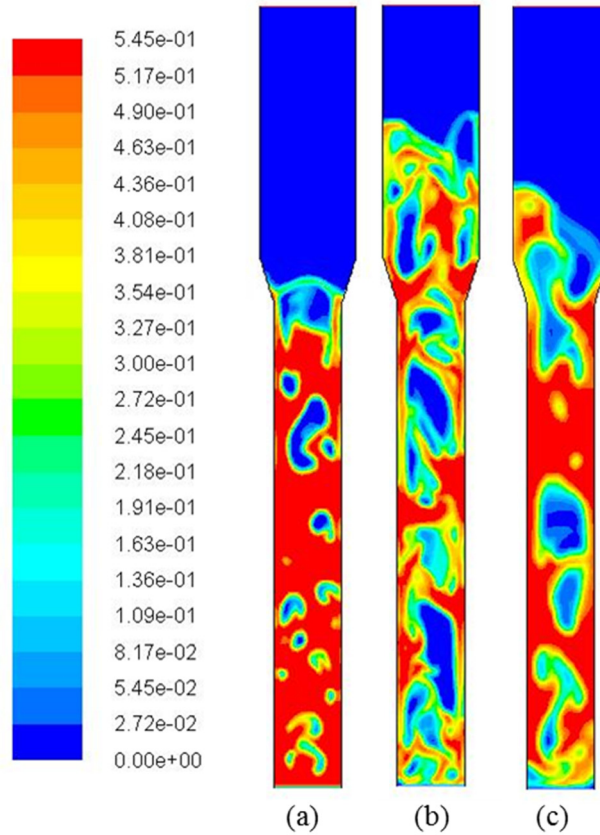
### Qualitative analysis of particle volume fraction

Figure 3.6 illustrates the instantaneous particle volume fraction predicted by the FB model. It can be seen that for  $U = 0.4$  m/s, a heterogeneous gas-solid system was observed with

agglomerates forming and dissolving dynamically. The particles aggregate, form agglomerates and are then carried away by the rising gas. The formation of aggregates is well captured by the incorporation of particle-particle force-balance concept in the drag model, unlike the conventional drag models. Figure 3.7 presents a qualitative comparison of particle volume fraction prediction employing different drag models at  $t = 15\text{s}$  for (a) Energy minimization multi-scale (EMMS) of Shi et al. (2011); (b) EMMS by Hong et al. (2013); and (c) FB model.



**Figure 3.6** Instantaneous particle volume fraction of FCC at  $U = 0.4\text{ m/s}$ ,  $d_p = 103\text{ mm}$ ,  $\phi = 0.1$ .



**Figure 3.7 Qualitative comparison of particle volume fraction of FCC at  $U = 0.4$  m/s,  $d_p = 103$  mm,  $\phi = 0.1$ ,  $t = 15$ s (a) EMMS-Shi model (b) EMMS-Hong model (c) FB model.**

The EMMS-Shi drag model captures the formation of very small bubbles. The modified version of this drag model designed specifically for bubbling fluidized bed, the EMMS- Hong and the FB model give good agreement with the experimental observations in predicting the bubbles and particles clusters. However, the bed expansion is over-estimated. Numerical simulation with the FB model is able to capture the bed expansion consistent with the experimental results of Dubrawski et al. (2013).

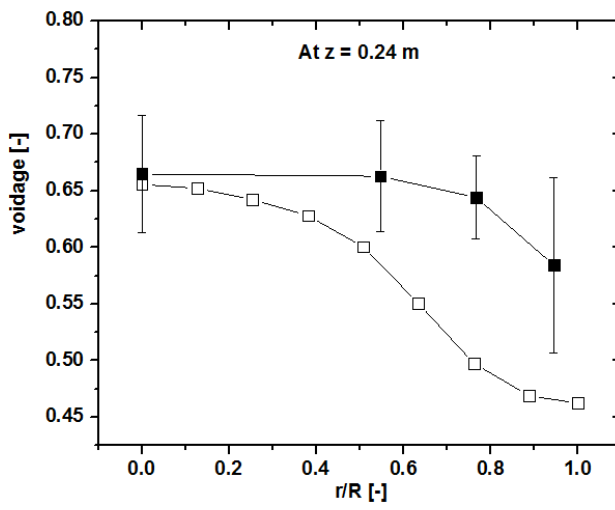
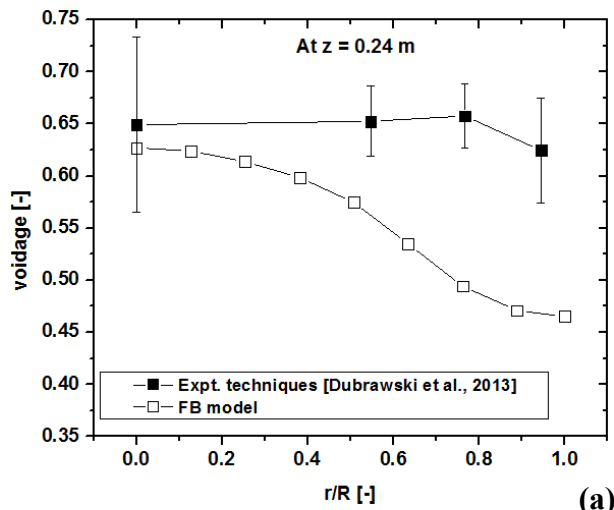
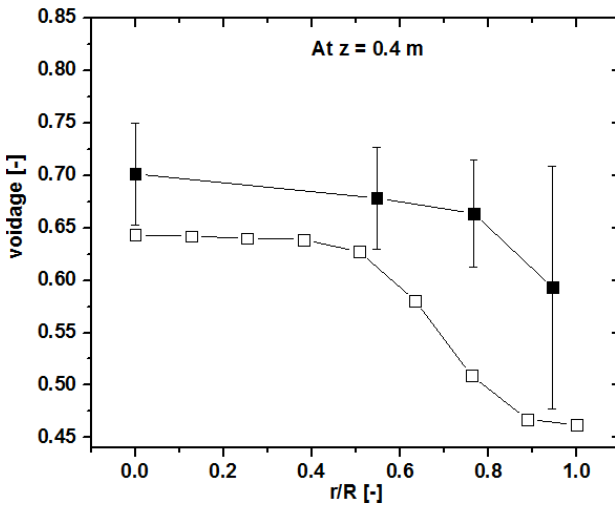
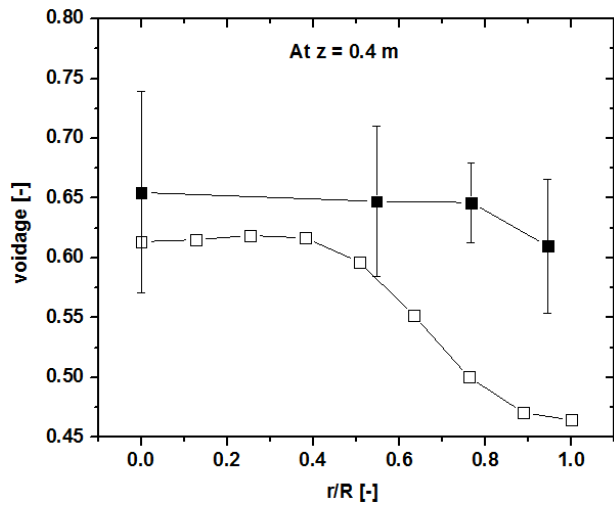
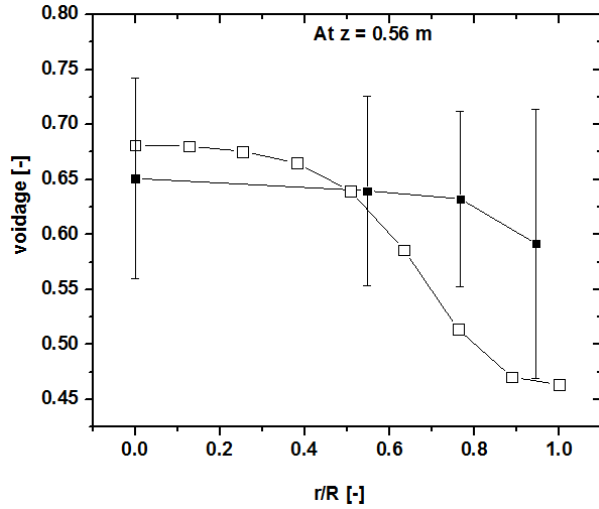
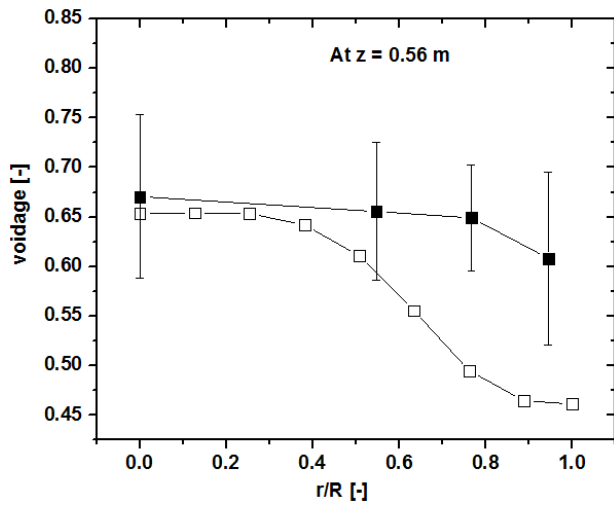


Figure 3.8 Radial profiles of time-average voidage at different heights for a)  $U = 0.3$  m/s and b)  $U = 0.4$  m/s.

Figure 3.8 shows time-average voidage profiles at  $U = 0.3$  and  $0.4$  m/s for  $d_p = 103 \mu\text{m}$  and a specular coefficient of  $\phi = 0.1$ . The experimental data obtained from different measurement techniques (Dubrawski et al. 2013) were averaged and shown with 95% confidence intervals as shown in Figure 3.8. Both experimental and FB model simulation results are folded due to axial symmetry with respect to the centerline at heights of 0.24, 0.4, 0.56 m. The voidage increases with increasing superficial gas velocity at each level. The higher voidage in the central region is due to non-uniform radial distribution of bubbles. At the walls, a higher concentration of particles is predicted, consistent with the experimental observations. It can be seen that the particles are mostly rising in the center of the bed and descending close to the wall. Significant difference between the experimental results and simulations is observed near the walls, which might be due to strong walls effects.

Figure 3.9 shows the effect of specular coefficient on the predicted radial distribution of time-averaged voidage. Simulated and measured voidages are high in the central region and lower near the wall. This suggests the presence of streamers of particles descending near the wall. The predicted results are within the range of the experimental dataset. In this study,  $\phi = 0.1$  was chosen for data extraction and further comparison of results.

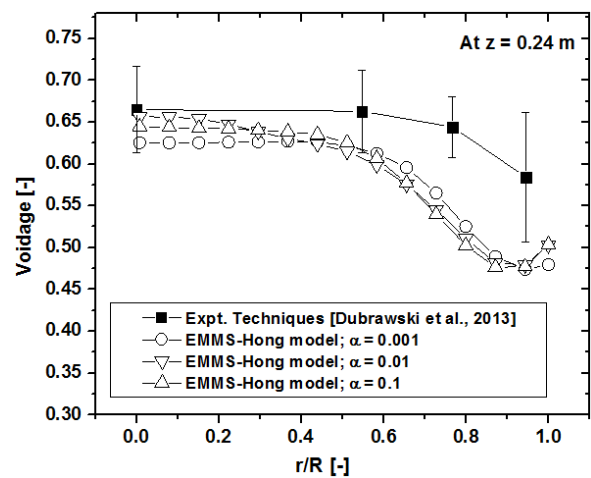
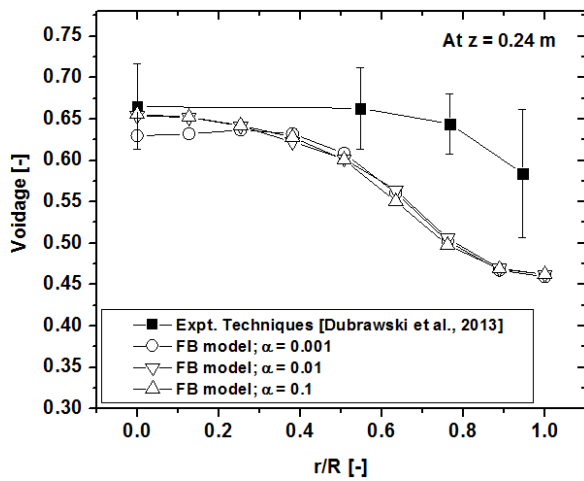
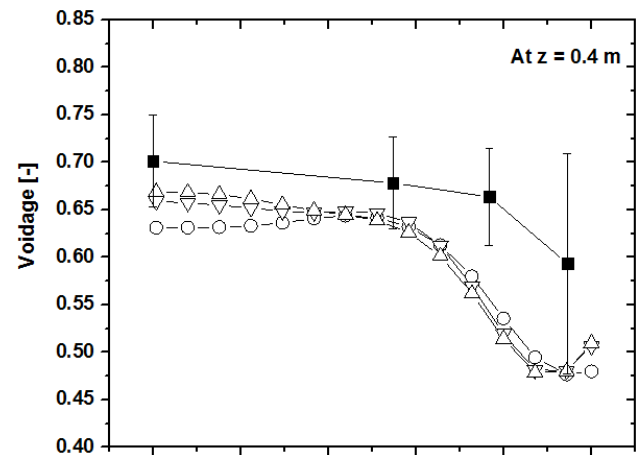
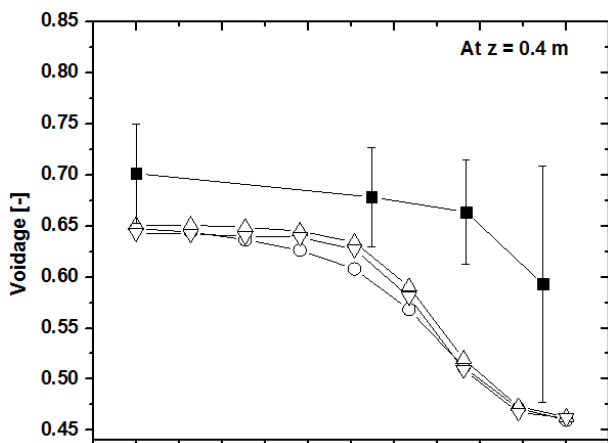
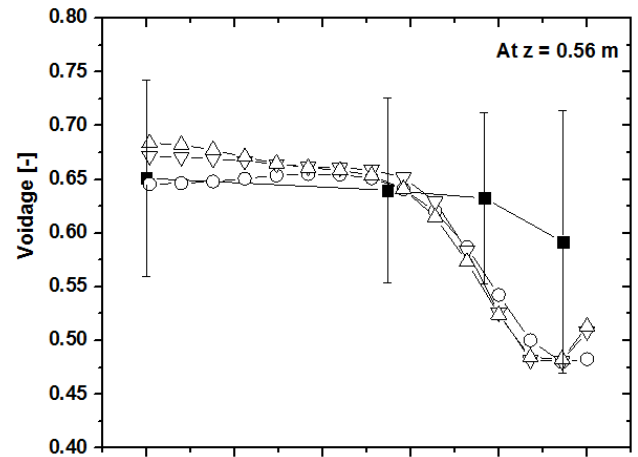
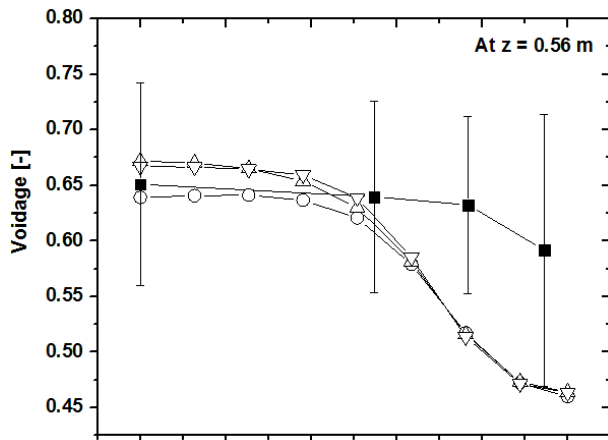


Figure 3.9 Effect of specularity coefficient on radial profile of voidage for  $U = 0.4$  m/s,  $d_p = 103$   $\mu$ m. Top row at  $z=0.56$  m, middle row at  $z=0.4$  m, bottom row at  $z=0.24$  m.

### 3.2.3.2 3-D simulation analysis

#### Mesh refinement study

After conducting mesh studies for 3D simulations, different conclusions were reached compared to the 2D simulations discussed in section 3.2.3.1. Having an additional dimension in the model provided sufficient room for agglomeration in view of the requirement that agglomerate size could not exceed the mesh size in the cases studied here. Therefore, the irregular phenomenon observed in 2D simulations in section 3.2.3.1 was not repeated in 3D simulations when refining the mesh size. The bed expansion and qualitative shape of bubbles/slugs for different mesh sizes were in agreement with experimental observations for the operating conditions of interest in this study. Figure 3.10 plots the mesh refinement test results for 3D CFD simulation of bubbling fluidized bed for  $U = 0.4$  m/s, demonstrating the voidage and particle velocity profiles using the FB drag model. It can be seen that the model predicts similar voidage and particle velocity profiles for the range of mesh sizes considered. It is also shown that the coarsest mesh (2332 cells) shows deviations at the wall for voidage and at the center for particle velocity compared to the other mesh sizes tested.

Considering the extensive computational requirements for utilizing more refined meshes for the 3D simulation and based on the results discussed above, a grid number of 3528 was found to be sufficient to obtain the CFD results, and this number was therefore selected for data extraction.

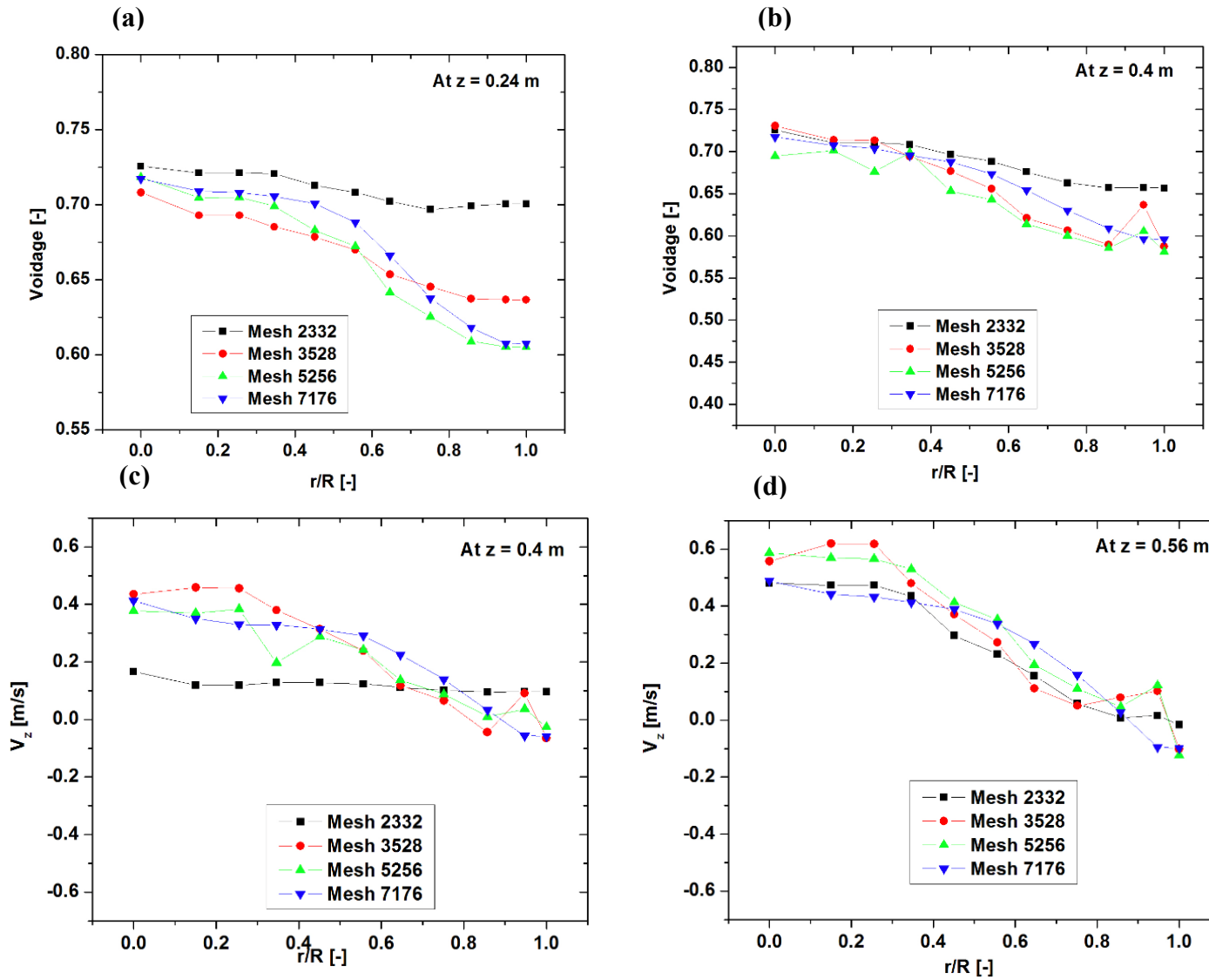


Figure 3.10 Mesh studies at  $U = 0.4$  m/s,  $d_p = 103$  mm and  $\phi = 0.1$  at different heights. (a) and (b) represent radial profiles of time-average voidage, whereas (c) and (d) show radial profiles of time-average particle velocity in axial direction

### **Qualitative analysis of instantaneous particle concentration using CFD**

As the fluidization proceeds, bubbles split and coalesce continuously due to wall effects and bubble interactions. The bubble formation causes bed expansion, increasing with increasing superficial gas velocity. Furthermore, higher gas velocity causes formation of large bubbles. This has also been reported by others (e.g. Zimmermann and Taghipour 2005). The formation of large bubbles in the central region due to coalescence is well captured. The flow field was stable after 20 s; the solid volume fraction distribution data thereafter are similar to each other.

The simulated velocity vectors for the granular and gas phase for the CFD-FB drag model in the vertical plane crossing the vertical axis are shown in Figure 3.11. The macroscopic solid circulation patterns observed in the experiments are captured in the simulations. Particles rise in the center due to bubble motion and subsequently return with breakup of bubbles. The particles tend to descend near the wall. This phenomenon led to gross circulation patterns. Particles descending along the walls move into the wake of the slugs and are then carried upwards.

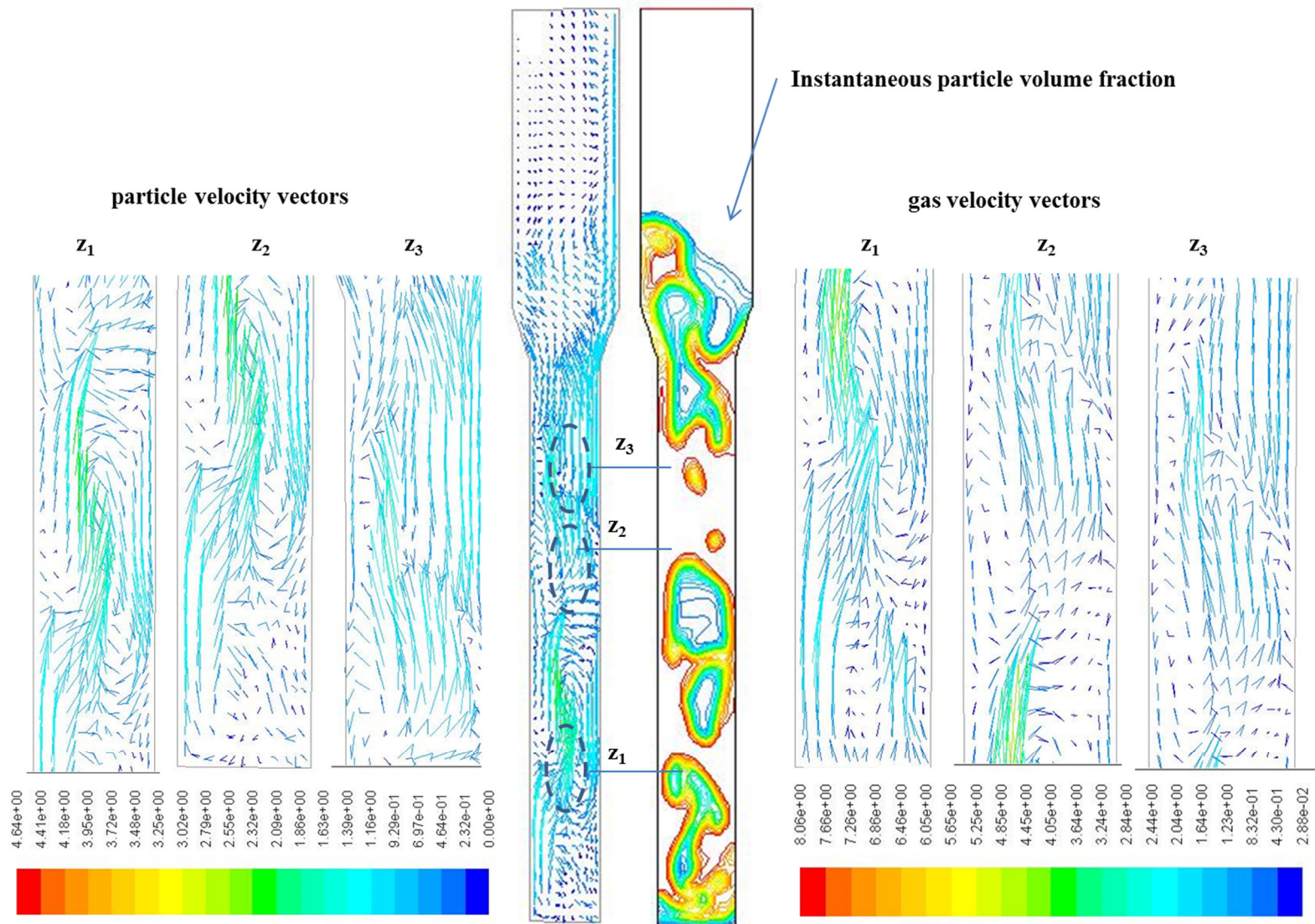


Figure 3.11 FB model prediction of instantaneous gas and particle velocity vectors at  $U = 0.4$  m/s and  $t = 15$  s.

### **Effect of different drag models**

Comparison of different drag models can be useful in testing the validity of models and how they perform in different situations. In this section, the drag correction model from the Energy-Minimization-MultiScale (EMMS) method described in Chapter 1 is compared with the FB model. Two recent versions of the EMMS model referred to as EMMS-Shi (Shi et al., 2011), specifically developed for the bubbling flow regime, and EMMS-Hong (Hong et al., 2013) are investigated in this study. The heterogeneity index, which is the correction factor calculated in EMMS method and applied to the conventional drag model, was obtained for the operating conditions in this study through personal communications (Wei, 2013). Mesh studies were conducted for both 2D and 3D simulations with the EMMS models. By comparing voidage and particle velocity profiles and taking computational time into consideration, 8178 Cells (compared to 2480 Cells for the FB model) for 2D studies and 5256 Cells (compared to 3528 for the FB model) for 3D studies were selected as most appropriate for the EMMS-Shi and EMMS-Hong models.

Figure 3.12 shows the profile of the average solid hold-up as a function of height. This shows that the average solid holdup changes very little with varying height above the distributor in the range of 0 – 0.98 m, suggesting that the granular distribution in the main body of the fluidized bed is relatively homogenous. Accordingly, the actual expanded bed height is about 1-1.1 m. There is a significant difference between the prediction of the FB drag model and the EMMS-Shi model, the version of the EMMS model specifically intended for the bubbling fluidization flow regime (Shi et al., 2011). However, the EMMS-Hong model gives results comparable to the FB model.

Major differences in predicting bed expansion are evident. Bed expansion results are compared in Fig 3.13 for the EMMS-Hong and FB models. Referring to the experimental value of 1.1 m for bed expansion in the previous section, it can be seen that the EMMS-Hong model over-predicts the bed expansion compared to the FB model. Fig 3.14 qualitatively compares 2D snapshots for FCC at  $U = 0.4$  m/s,  $\phi = 0.1$ ,  $t = 15$ s using different drag models: (a) Wen-Yu model; (b) EMMS-Shi model; (c) EMMS-Hong model; and (d) FB model. There are evident differences in prediction of bed expansion using these four models. The EMMS-Shi model predicts small bubbles compared to the two models which predict slugs forming in the bed, as expected based on the operating conditions.

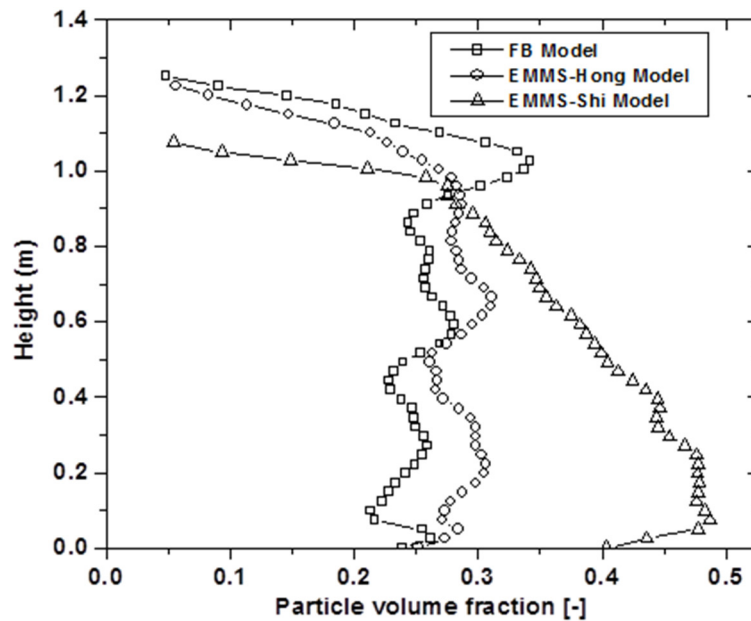


**Figure 3.12** Variation of axial profile of particle volume fraction averaged over last 10 s of simulation with height at  $U = 0.4$  m/s for different drag models.

2D simulation results showed that among the EMMS-Shi, EMMS-Hong and FB models, the first of these was unsuccessful in capturing the expected flow regime and hydrodynamics in the bed, while the latter two models were able to capture the flow characteristics in the bed. However, bed expansion results indicated that only the FB model obtained promising predictions compared to the experimental results. In view of this finding, only the EMMS-Hong and FB models are applied to the 3D simulations in the next section.

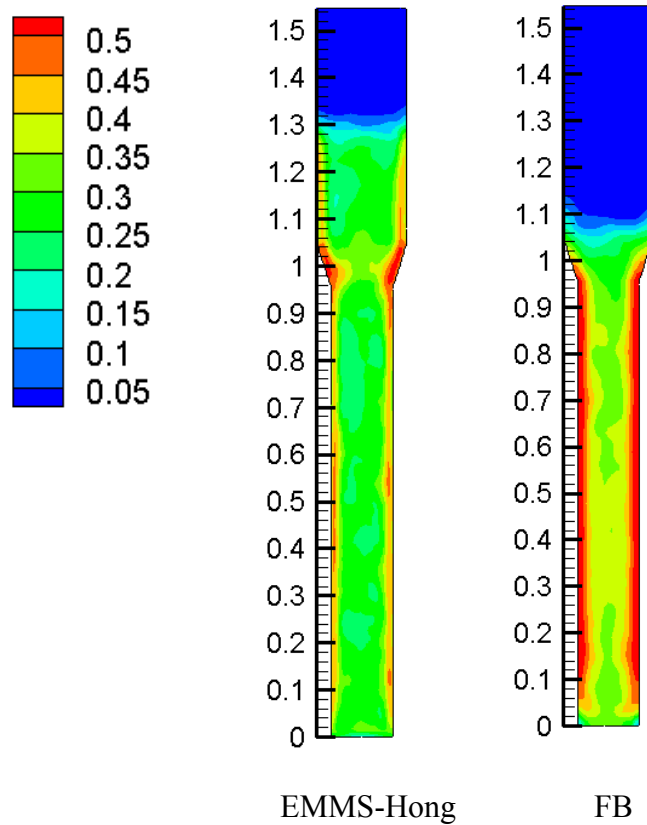


**Figure 3.13** Contours of time-average solid volume fraction at  $U = 0.4$  m/s for bed expansion comparing EMMS-Hong and FB models.

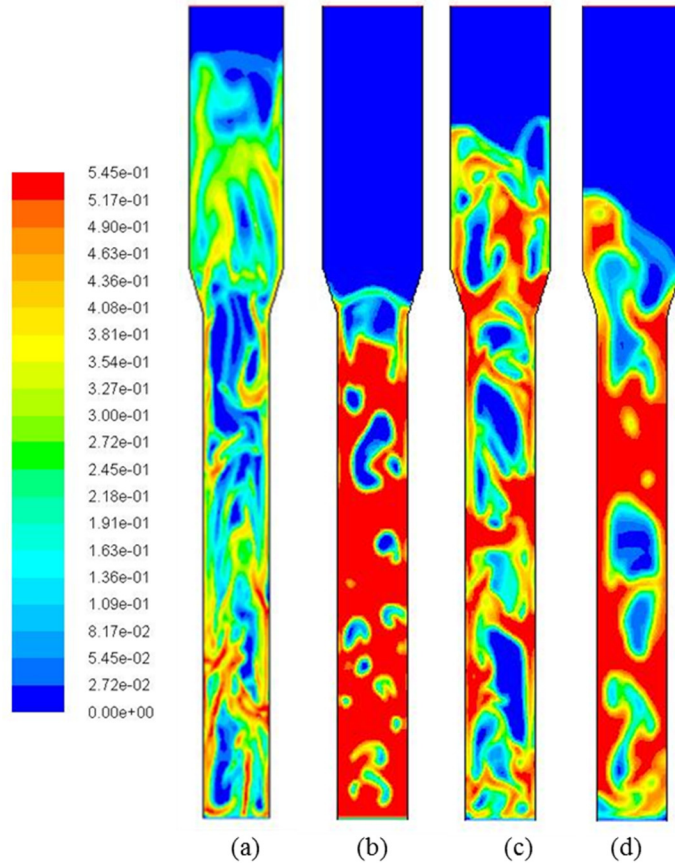


**Figure 3.14 Qualitative analysis of 2D snapshots of FCC volume fraction at  $U = 0.4$  m/s,  $\phi = 0.001$ ,  $t = 15$ s: (a) Wen-Yu (b) EMMS-Shi (c) EMMS- Hong (d) FB model.**

### 3.2.3.3 3D models and comparison with 2D simulations

3D modeling is more realistic in considering the wall effects in a fluidized bed compared to 2D simulations. Despite the drawbacks of 2D simulations, they have the benefits of faster computational speed and can be used to analyse the qualitative behavior of the flow. However, quantitative 2D results should be regarded with caution as they can differ significantly from 3D simulation results.

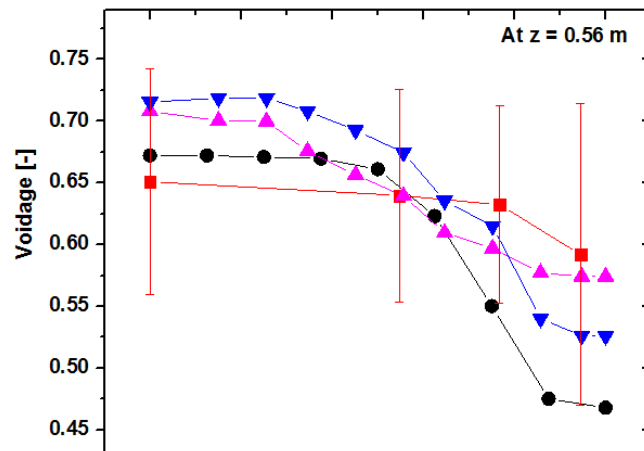
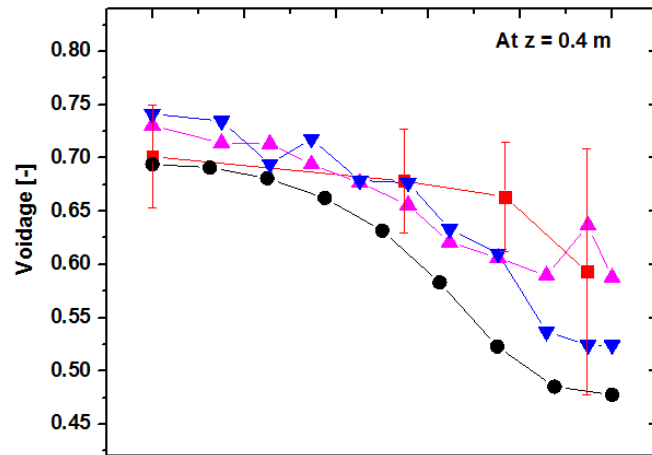
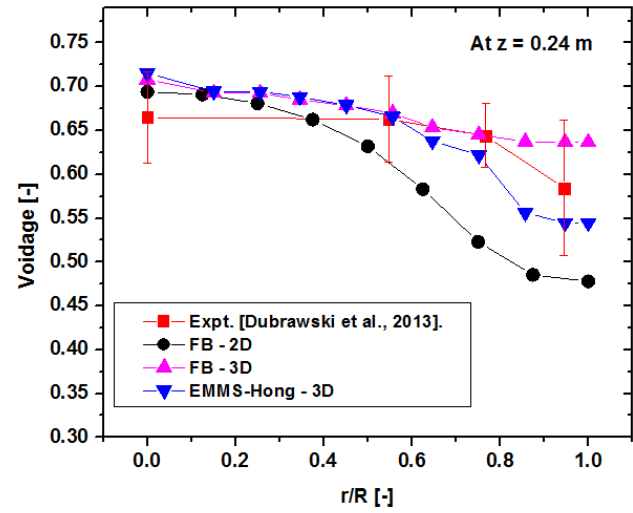
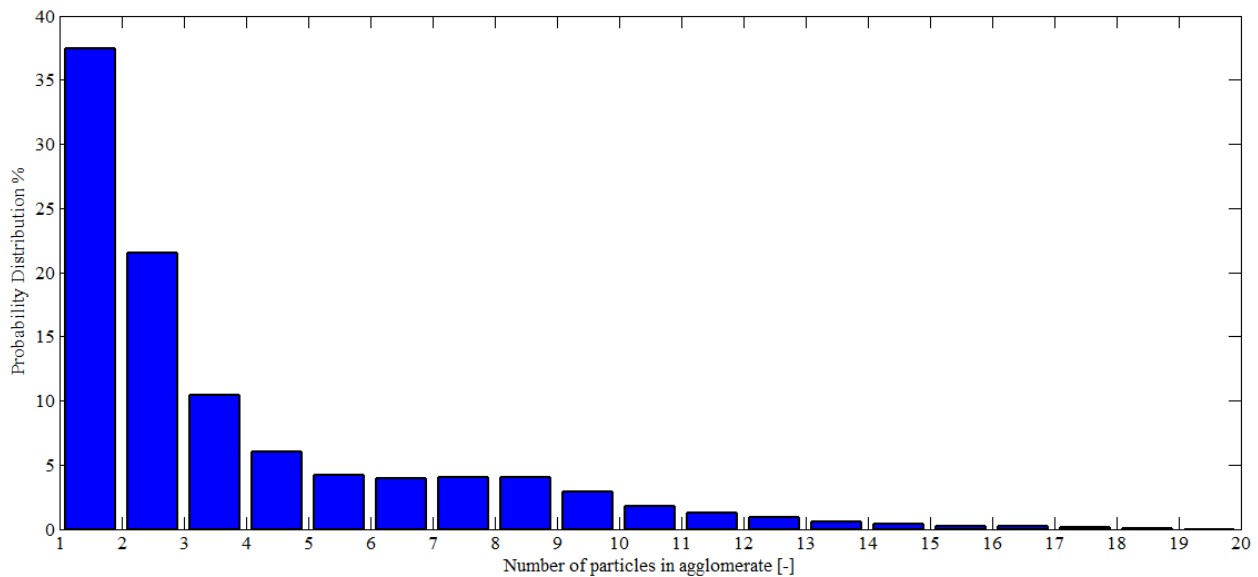


Figure 3.15 Comparison of radial profiles of time-average voidage from 2D and 3D simulations with experimental results at  $U = 0.4$  m/s.

Time-average radial voidage over the last 10 s of the 15 s simulation time at different heights from 2D/3D simulations and experiments are compared in Fig. 3.15. Both the FB and EMMS-Hong models obtained satisfactory results which fall within the experimental range for 3D simulations but 2D simulation results show deviations near the wall boundary. Qualitative comparison of the results also confirms the ability of FB and EMMS-Hong models to predict the fluidization flow regimes and bed expansion.

Fig. 3.16 shows the probability distribution of the number of particles in agglomerates (“N” in equation 2.29) obtained from 3D simulations for superficial gas velocity of 0.4 m/s over the last 5 s of modeling. It is shown that more than 55% of the distribution is for agglomerates which contain 3 particles or fewer. The probability of formation for larger agglomerates (> 3 particles and less than 10 particles) are close to 35% with further reduction for agglomerates containing between 10 and 20 particles. There were few agglomerates with > 20 particles.



**Figure 3.16 Probability distribution plot for number of particles in agglomerate obtained from 3D simulations at  $U = 0.4$  m/s.**

### 3.3 Case III– minimum bubbling velocity, $U_{mb}$

By definition, Geldart group “A” particles have an interval of homogeneous expansion beyond minimum fluidization, not yet reaching the onset of bubbling. The gas velocity at which the first bubbles appear is defined as the minimum bubbling velocity,  $U_{mb}$ . The transitions from homogenous expansion to a bubbling bed and the prediction of minimum bubbling velocity,  $U_{mb}$ , have been subjects of considerable interest.

Although some numerical simulations using a DEM framework have been reported to be successful in predicting the minimum bubbling velocity (Hou et al. 2012; Wang et al. 2010), TFM studies have shown that conventional Eulerian-Eulerian models fail to predict  $U_{mb}$  correctly. Wang et al. (2010) investigated this issue using coarse and fine grid simulations with the conventional Wen-Yu model in the Eulerian-Eulerian framework. They concluded that the effect of gas and particle properties on the minimum bubbling velocity can be correctly captured by the KTFG-based two-fluid model when a sufficiently fine grid is used, such that the meso-scale bubble structure can be resolved. Due to the limitation of computational resources, the extremely small grid size required to resolve the meso-scale bubble structure did not allow them to simulate a laboratory-scale fluidized bed. They reported that a grid size of about  $3d_p$  was needed to capture correct hydrodynamic behavior and to predict accurately the minimum bubbling velocity.

In this study,  $U_{mb}$  predictions are investigated further based on a comparison between simulations performed with the new FB model and DEM simulations of the identical case reported in the literature.

### 3.3.1 Simulation Setup

The simulation conditions were set to match the DEM simulations of Hou et al. (2012). Table 3.5 lists the physical properties as well as the simulation parameters. A particle diameter of 100  $\mu\text{m}$  was selected based on one of the cases studied by Hou et al. (2012) for group A particles. The Hamaker constant was set at  $2.1 \times 10^{-21}$  J, the same value as in the DEM studies. 2D Eulerian-Eulerian simulations were performed in ANSYS Fluent V14, utilizing the conventional Wen-Yu relationship with implementation of the new FB model to correct the drag term. Periodic boundary conditions (meaning that when an object passes through one side of the unit cell, it re-appears on the opposite side with the same velocity) the same as for DEM simulations, were used at the walls, with uniform velocity at the bottom and a mass outflow condition at the top boundary of the bed. In the DEM simulations of Hou et al. (2012), asperities were not explicitly considered when calculating the van der Waals forces, but a cut-off value of 1 nm was selected in their work as the particle separation distance. In this work, the same separation distance (1 nm) is adopted to make the cohesive models of DEM and Eulerian-Eulerian simulations identical. This differs from case I, in which asperities are considered, since the particles used in the experiments related to that case were rough. The input values for the new FB model are chosen to facilitate direct comparison with experimental or DEM work. Because the particles in DEM study by Hou et al. (2012) were supposed to be smooth, frictional viscosity was neglected in our simulations.

A time step of  $10^{-4}$  was found to be suitable to reach convergence, while being small enough to ensure negligible numerical errors. The laminar model was solved using the Phase-Coupled SIMPLE algorithm for the pressure-velocity coupling and second-order upwind

discretization schemes for the convection terms. A mesh size of 10 particle diameters was selected for the simulations.

Hou et al. (2012) started their DEM simulations with 10,000 particles in the bed. In the present work, simulations were initiated assuming that particles are at minimum fluidization with the minimum voidage and the volume of particles as provided by Hou et al. (2012), The corresponding initial static height and other key properties appear in Table. 3.5.

**Table 3.5 Physical and simulation parameters used in modeling based on values given by Hou et al. , (2012).**

<u>Property</u>	<u>Value</u>
Superficial gas velocity	Varied between 0.0 to 0.02 m/s
Gas viscosity	$1.8 \times 10^{-5} \text{ kg.m}^{-1}.\text{s}^{-1}$
Mean particle diameter	100 $\mu\text{m}$
Particle density	$1440 \text{ kg/m}^3$
Domain width	0.006 m
Domain height	0.02 m
Static height	0.0035 m
Young's modulus	$10^7 \text{ N.m}^{-2}$
Poisson ratio	0.3
Minimum voidage	0.39
Particle-particle restitution coefficient	0.8

### 3.3.2 Results and discussion

The minimum bubbling velocity definition is based on the appearance of the first bubble in the bed (Geldart, 1973). Visual observations of the first bubble were reported in previous CFD studies, with bubbles defined as regions where the solid volume fraction is less than 0.2 (Yates et al. 1994) or 0.15 (Wang et al., 2010). However, defining the threshold limit makes this technique subjective.

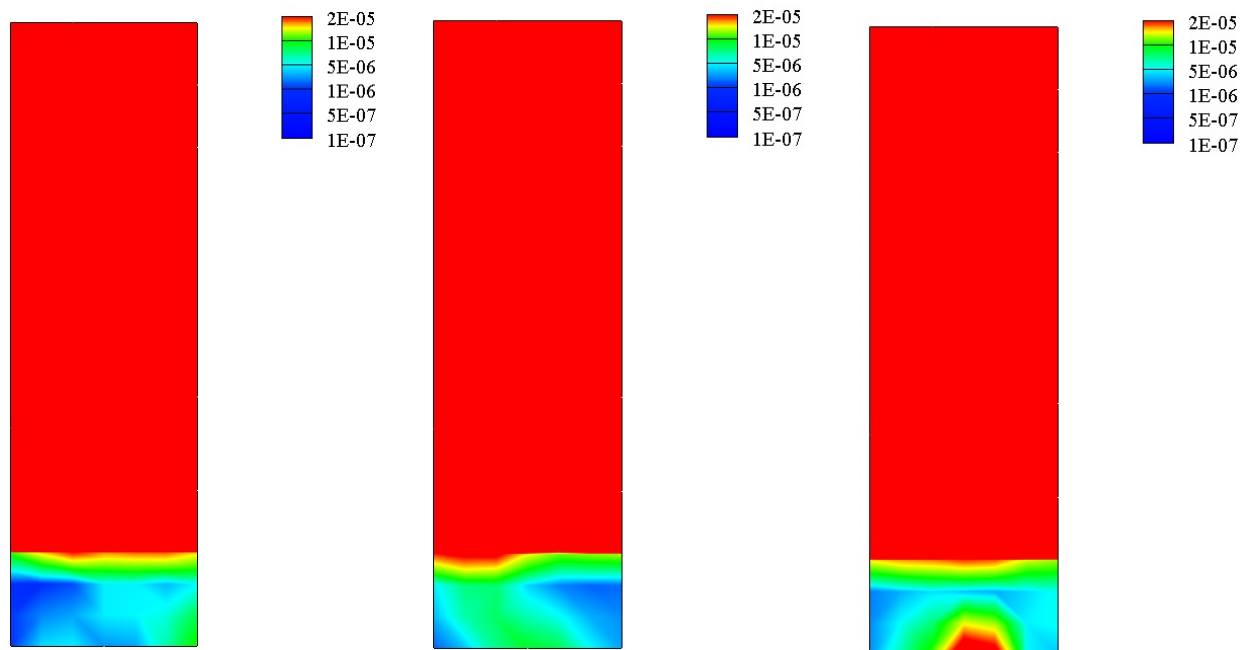


**Figure 3.17** Contours of mean granular temperature ( $\text{m}^2/\text{s}^2$ ) for superficial gas velocities of 0.007 m/s (left), 0.01 m/s (middle) and 0.012 m/s (right) with mesh size =  $10 \times d_p$

A new criterion for determination of  $U_{mb}$  was introduced (Wang et al. 2010) based on the granular temperature of particles in the bed. In the present work, sudden changes in granular temperature, e.g. by two order of magnitudes, as suggested by Wang et al. (2010), are utilized to determine  $U_{mb}$ . At very low velocities, both the mean and local granular temperatures show a value of  $10^{-7} \text{ m}^2/\text{s}^2$ , which increases as the superficial gas velocity escalates. The contours of

time-averaged granular temperature for three different superficial gas velocities are depicted in Fig. 3.17. When the superficial gas velocity reaches 0.012 m/s in the bottom section of the simulation domain, the time-average granular temperature climbs above  $10^{-5} \text{ m}^2/\text{s}^2$  (shown by the white region in Fig. 3.17), two orders of magnitude larger than the initial value of  $10^{-7} \text{ m}^2/\text{s}^2$ . The contour of local granular temperature at sample time = 4 s is shown in Fig. 3.18, with the two orders of magnitude escalation of granular temperature again shown by the white patch, in this case at the left boundary of the domain. Similar increases in local granular temperature were observed at different time frames for a superficial gas velocity of 0.012 m/s.

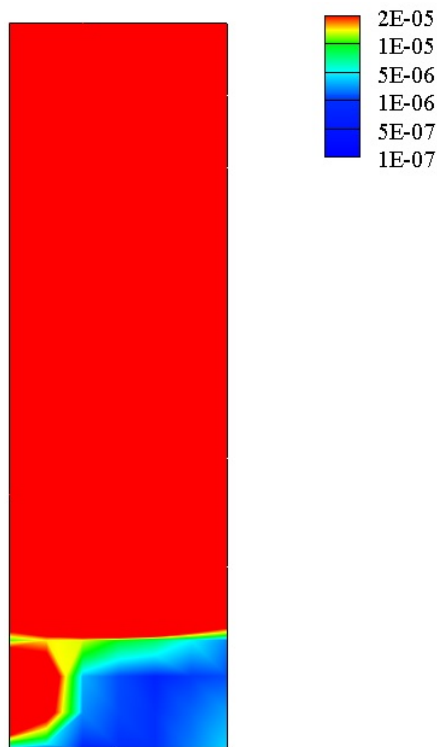


**Figure 3.18** Contour of local granular temperature ( $\text{m}^2/\text{s}^2$ ) for a superficial gas velocity of 0.012 m/s at  $t = 4 \text{ s}$  with mesh size =  $10 \times d_p$ .

Based on the granular temperature  $U_{mb}$  determination criterion, the results of CFD simulations with the FB drag model show 0.012 m/s as the minimum bubbling velocity. Using

the same criterion with the conventional Wen-Yu model predicts much larger  $U_{mb}$ , near 0.09 m/s. The DEM results of Hou et al. (2012) and Eulerian-Eulerian simulations using the conventional Wen-Yu model are within a factor of 9, whereas  $U_{mb}$  predicted by the DEM and FB models are much closer. These results show promising agreement between Eulerian-Eulerian simulations using the new FB drag model and DEM simulations for the same case. However, since the particles in this case were ideal, with neither asperities nor particle size distribution included, more studies are required to test the ability of the proposed model to determine the minimum bubbling fluidization velocity of a wide range of group A particles.

### **3.4 Summary**

Hydrodynamic characteristics such as minimum bubbling velocity, radial and axial voidage distribution, particle volume fraction profiles, bed expansion, agglomeration, and circulation patterns in a bubbling fluidized bed were investigated with CFD. Two versions of the EMMS drag models and the FB model were employed in the CFD simulations, and their predictions were compared. The drag models predicted different flow in the granular phase, influencing the predicted bed expansion and particle concentration in the dense phase regions of the bed. The FB model is capable of predicting the agglomerate formation, while the EMMS models take into account cluster formation in the bed.

The FB model was able to capture the gross solid circulation phenomena. The voidage profile and bed expansion predictions from both 2D and 3D simulations using the FB model are consistent with experimental data. On the other hand, qualitative comparison of results from 2D simulations showed that only the FB and EMMS-Hong models show promising agreement with experimental observations except for bed expansion with the EMMS-Hong model. 3D

simulations utilizing the EMMS-Hong model also predicted radial profiles of time-average voidage in good agreement with experiments. It is noteworthy that the number of cells utilized for the EMMS models was considerably larger than the number used for the FB model. This can be a potential benefit for the FB model, with substantial computational savings when performing large-scale simulations. However, careful mesh studies should be conducted, especially in 2D simulations, where increasing the number of cells does not necessarily improve CFD predictions for the FB model. The agglomerate size vs. grid size should be checked during simulations to ensure that agglomerates in the bed do not exceed the grid size. Both qualitative and quantitative comparisons should be conducted for mesh studies utilizing the FB model.

Minimum bubbling velocity predictions from the FB model were compared with predictions from DEM simulations by Hou et al. (2012) for an ideal case with uniform smooth particles. DEM simulations were chosen in this work to enable a comparison with physical properties as identical as possible for better investigation of the effect of cohesive forces on predictions of  $U_{mb}$ . The parameters of the cohesive part of the proposed Eulerian-Eulerian model were set to provide fair comparison with the DEM simulations of Hou et al. (2012). Good quantitative agreement was obtained between the Eulerian-Eulerian FB and DEM simulations, whereas the conventional Wen-Yu relationship over-estimated  $U_{mb}$  by an order of magnitude. This shows that including the effect of cohesive forces can improve the prediction of hydrodynamic properties. The same conclusion was drawn in DEM simulations for the prediction of minimum bubbling velocity (Hou et al., 2012). The good agreement between two-fluid modeling using the FB model and DEM simulations is encouraging, but further investigation is needed for other systems.

Despite the fact that the new FB model is capable of predicting important hydrodynamic properties for Geldart Group A group, a definitive conclusion on the effectiveness of the model requires further simulations and comparisons with experimental data. More work is required in the future to cover a wider range of superficial gas velocities and to compare systems with other hydrodynamic properties to experimental results.

## Chapter 4: Liquid Injection Experiments at ICFAR

### 4.1 Background

Injection of liquid is an important component of FCC fluidized bed reactors, playing a key role in determining their overall performance. Effective contacting of the liquid droplets and solid particles is necessary to obtain high yields. Considering this importance, investigation of liquid injection has been a subject of considerable interest in recent years.

There are a number of research reports on non-evaporative (Leach et al. 2008; Ariyapadi 2004) and evaporative (Du et al., 2006; Gehrke & Wirth, 2007) liquid injection experiments involving injection of water or liquid nitrogen. Ethanol has also been used by some research groups to study the contact between liquid droplets and particles in fluidized beds. Bruhns (2002) and Bruhns & Werther (2005) performed experimental studies on the injection of water and ethanol into fluidized beds of quartz and FCC catalysts on a pilot scale. Based on the results from these experiments, they introduced a new model for the mechanism of liquid injection which assumes instantaneous wetting of the fluidized particles at the nozzle exit and considers the transport of the wetted particles by gross solids mixing within the bed. However, their basic assumptions of particle wetting with ethanol and the degree of liquid mixing inside the bed have not been tested experimentally.

McMillan et al. (2005) investigated the injection of ethanol into a fluidized bed containing coke particles experimentally. They developed a method to determine the local quality of solid liquid mixing on a short time scale. This technique uses temperature to characterize solid-liquid mixing. They compared solid-liquid mixing for a case where the spray

was introduced as a free jet with another where a draft tube was inserted to promote mixing. They reported superior mixing with the draft tube present in the bed.

The effect of particle porosity on liquid-solid mixing inside the bed is a topic of importance, but it has received little attention in the literature. Leclère et al. (2001, 2004) developed a method to investigate vaporization of injected liquid inside a fluidized bed based on quenching the bed and creating agglomerates<sup>2</sup>. Emphasizing the effect of liquid droplet size on the time of vaporization, they developed a heat-transfer-based model which predicts the formation of agglomerates when liquid droplets larger than bed particles are injected into a hot fluidized bed. The particle porosity was shown to be important as the experimental data indicated > 80% pore filling.

A number of liquid measurement techniques such as X-ray imaging, CCD camera recording and electrical capacitance/conductance impedance methods (Leach et al., 2008, 2009) have been utilized by different research groups. These methods are non-intrusive, unaffected by process conditions, and can be used to obtain useful information such as jet penetration length, expansion angle, agglomeration and local liquid dispersion.

## **4.2 Objectives**

Understanding the mechanism of liquid jet mixing inside FCC reactors is crucial. As discussed above, there are still areas which require more research. Experimental findings would be useful to help understand the interaction between phases in the injection region. For this purpose, liquid injection experiments were conducted by the author at the Institute of Chemical

---

<sup>2</sup>“Agglomerate” in Chapters 4 and 5 denotes the presence of interface liquid that fills the space between particles, holding the particles together.

and Fuels from Alternative Resources (ICFAR) of Western University in London, Ontario. The electrical capacitance (EC) impedance measuring technique previously used at ICFAR (Leach et al. 2008, 2009) was again utilized in this work, with ethanol as the injected liquid due to its favorable electrical capacitance characteristics and its volatility. The main objectives of these experiments were:

- To compare liquid mixing in fluidized beds containing (porous) FCC and (non-porous) silica sand.
- To make qualitative and quantitative measurements of liquid dispersion in fluidized beds containing FCC particles. No previous reported quantitative analysis of an evaporative liquid inside the bed using the EC measuring technique has been reported.
- To analyze liquid mixing inside the bed.
- To investigate liquid vaporization related to mass transfer inside the bed.
- To determine the extent of liquid diffusion inside FCC particle pores.

Liquid injection into a fluidized bed containing silica sand was explored to provide quick comparison with later injection into a FCC bed. Due to poor wettability of sand with ethanol, as discussed below, no quantitative analysis was performed on the sand bed.

### **4.3 Experimental apparatus**

The experiments were performed in a Plexiglas fluidization column of rectangular cross-section, 0.49, 0.1 m in cross-section and 0.92m high. A dipleg of diameter 25 mm was installed inside the column as depicted in Fig. 4.2. Twenty electrodes were evenly spaced at different heights on one side wall of the column. These electrodes were 0.05m high x 0.1 m wide metal strips. A common electrode (0.4 m high x 0.5 m wide) was placed on the opposite side of the

column, facing the 20 electrodes on the other side. These electrodes were connected to an electrical board which had been specifically designed for this project by ICFAR personnel. The measuring circuit in this board was an AC-based capacitance meter with a differential noise canceling system and a sampling frequency of 10 Hz for each electrode. It used a sine-wave voltage as the excitation source to produce an AC input current and an amplifier to convert this current into an AC voltage. The output signal from the capacitance meter was then sent to a data acquisition card and recorded by a computer utilizing a MATLAB code. More details on the capacitance circuit can be found in the work of Yang (1996).

The injection nozzle was 210 mm above the inlet gas distributor, and a sampling port was installed 80 mm directly above the injection nozzle. In our tests, before operation, the column was filled with enough solid particles to cover completely all the area exposed to electrodes to a static bed height of 410 mm above the gas distributor.

The EC measuring system and the connections to the column are shown schematically in Fig. 4.1. The numbering system for electrodes is shown there, as well as the key dimensions of the column and clearances.

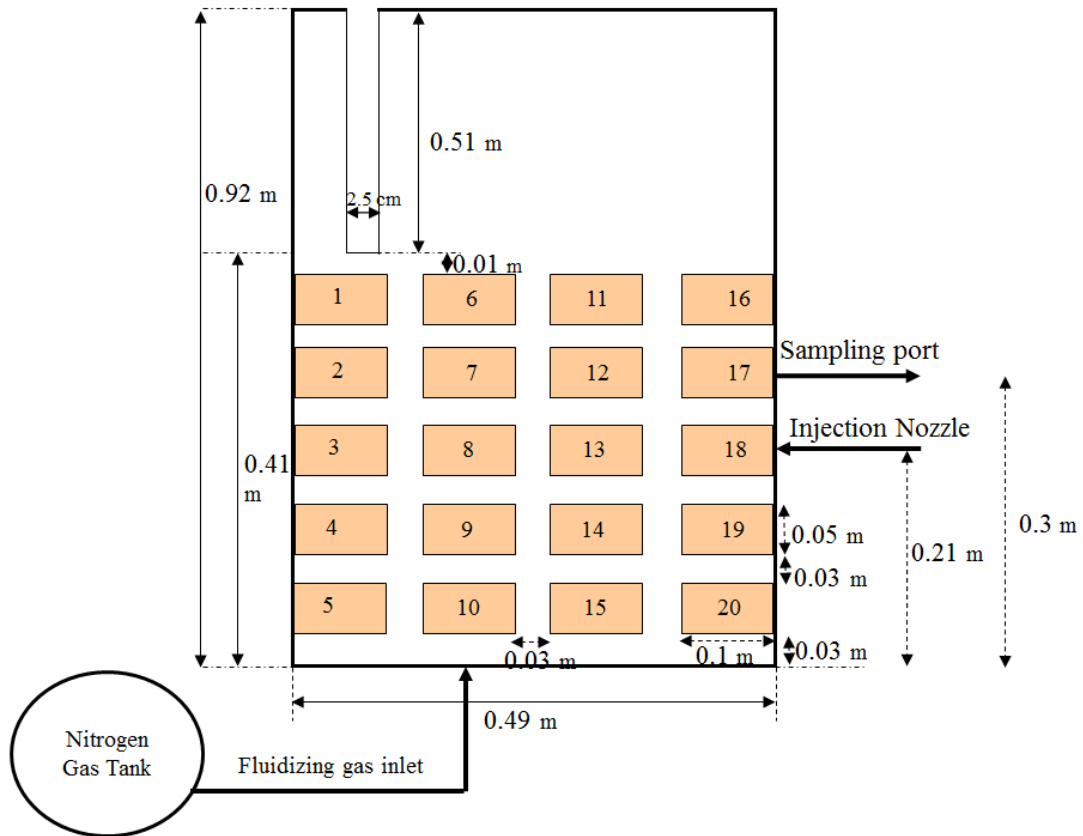


Figure 4.1 Electrode configuration and numbering scheme (not to scale) for ICFAR column.

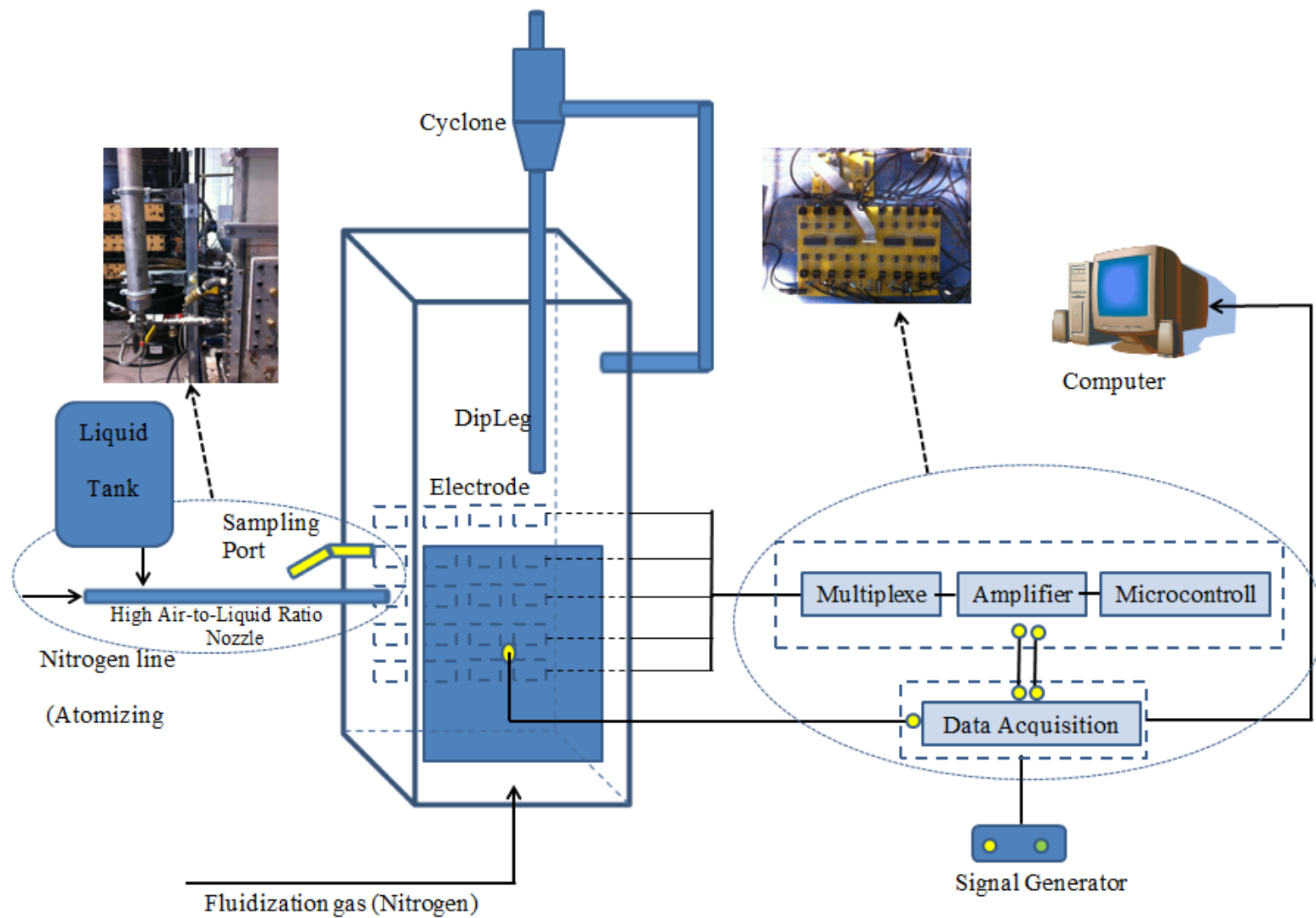


Figure 4.2 Schematic of Experimental Equipment.

### 4.3.1 Liquid injection assembly

In this study, a high air-to-liquid mass flow ratio (ALR) nozzle was used, through which a sufficiently large volumetric flow (up to 0.15 m<sup>3</sup>/min) of atomization gas passed to provide excellent dispersion of injected liquid onto fluidized particles (ALR  $\approx$  45%). The ALR is the ratio of atomization gas (N<sub>2</sub>) mass flow to injected liquid mass flow. Since the high-ALR nozzle minimizes agglomerate formation, it is suitable for studying dispersion of free moisture inside the bed.

Fig. 4.3 shows a schematic of the injection assembly used in our study. It was comprised of a premixer where gas and liquid were introduced separately, and an atomization nozzle. The liquid was introduced into the premixer in the direction forming a 30° angle with the nozzle, whereas gas was introduced at a 20° angle. A static pressure transducer located between the premixer and nozzle inlet (PT in Fig. 4.3) measured the nozzle upstream pressure. The nozzle tip intruded 67 mm into the bed horizontally. The liquid injection assembly was equipped with a liquid line connected to a liquid tank to inject liquid into the fluidized bed, and a nitrogen line to atomize the liquid into small droplets. Atomization nitrogen was supplied from a manifolded bank of high-pressure cylinders at constant pressure controlled by a pressure regulator, with its mass flow rate controlled by a sonic orifice of diameter 1.6 mm.

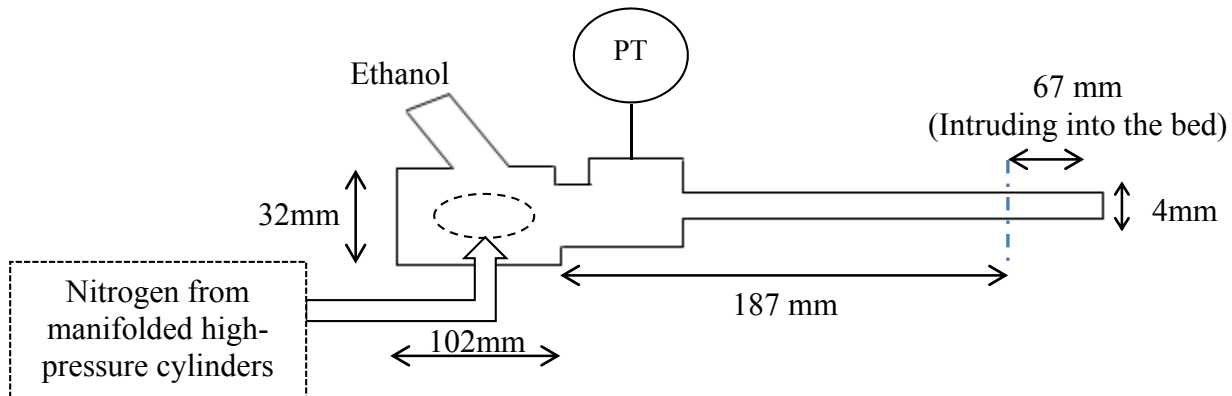


Figure 4.3 Schematic of liquid injection assembly (not to scale).

## 4.4 Dry experiments (with no liquid injection)

### 4.4.1 Sand

The sand used in this study was Barco 71 silica sand from Opta minerals with a Sauter mean diameter of  $185\mu\text{m}$ , size distribution shown in Fig. 4.4 and a density of  $2650\text{ kg/m}^3$ . In each experiment, the column was filled to a height of 410 mm, corresponding to 33 kg of dry sand. The superficial gas velocity was varied from 0.20 to 0.35 m/s. Higher velocities could not be achieved due to severe vibration of the setup.

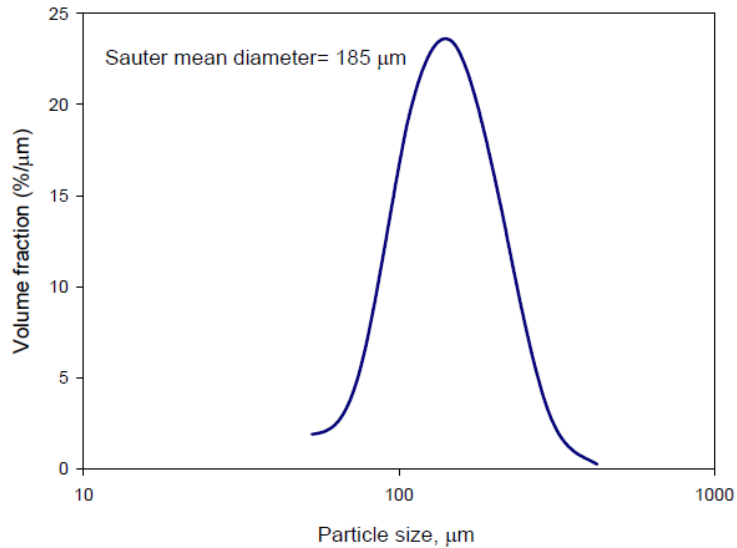


Figure 4.4 Particle size distribution for the silica sand particles (Farkhondehkavaki et al., 2012).

### 4.4.2 FCC

The FCC particles tested in this study were spent catalyst particles obtained from Coanda Research and Development Company. The density of these FCC particles was determined using a liquid pycnometer to be  $1600\text{ kg/m}^3$ . The cumulative particle size distribution, shown in Fig. 4.5, was determined by a HELOS/CUVETTE laser diffraction device from Sympatec GmbH. The Sauter mean diameter (SMD) and median diameter were determined to be  $70\mu\text{m}$  and  $101\mu\text{m}$  respectively. In each experiment, the column was filled to a static bed height of 410 mm

corresponding to an inventory of 22 kg of FCC. The superficial gas velocity was varied from 0.15 to 0.30m/s.

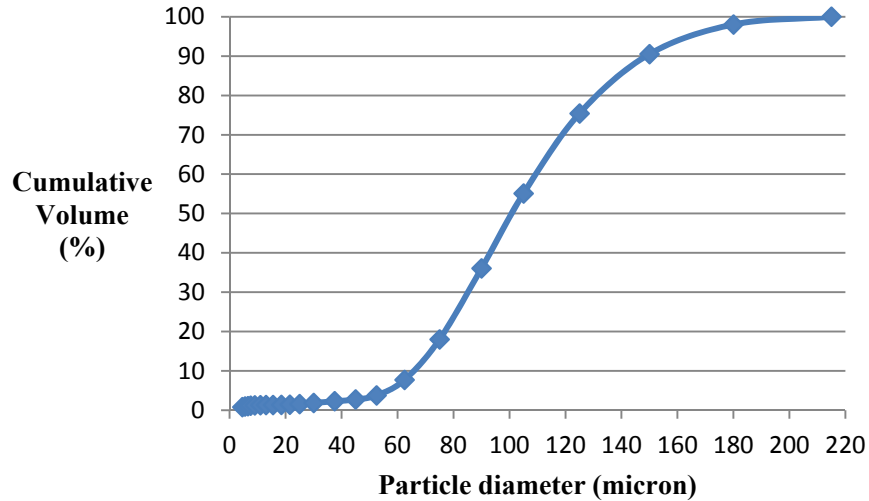


Figure 4.5 Cumulative particle size distribution of FCC particles

#### 4.4.3 Voidage measurements

One of the main variables measured during the dry tests was the local voidage. For that purpose, the measured electrical capacitance is normalized based on the following formula to give the normalized local voidage:

$$\text{Local voidage} = C_{\text{Norm}} = 1.0 - \frac{C_{\text{local}} - C_{\text{min}}}{C_{\text{max}} - C_{\text{min}}} \times (\text{Maximum solid packing}) \quad \text{Eq.4.1}$$

where “C” represents the capacitance, with  $C_{\text{max}}$  corresponding to a de-fluidized (packed) bed of sand or FCC, and the minimum capacitance corresponding to an empty column. The bulk solid packing ( $\epsilon_b$ ) was estimated from:

$$\epsilon_b = \frac{W}{\rho_s g A H_s} \quad \text{Eq.4.2}$$

where  $W$  represents the weight of solid particles inside the de-fluidized bed,  $\rho_{s}$  is the bulk density,  $A$  is the bed cross-sectional area and  $H_s$  represents the height of solid particles inside the de-fluidized bed.

#### 4.5 Liquid droplet size analysis

Determination of liquid droplet size after injection into the bed is vital for comparing experimental data with CFD models. The procedure outlined by Portoghese et al. (2008) at ICFAR was followed in this study. Open-air experiments were conducted using the system depicted in Fig. 4.6, with the liquid droplet size determined from the attenuation of a laser beam intersecting the gas-liquid spray.

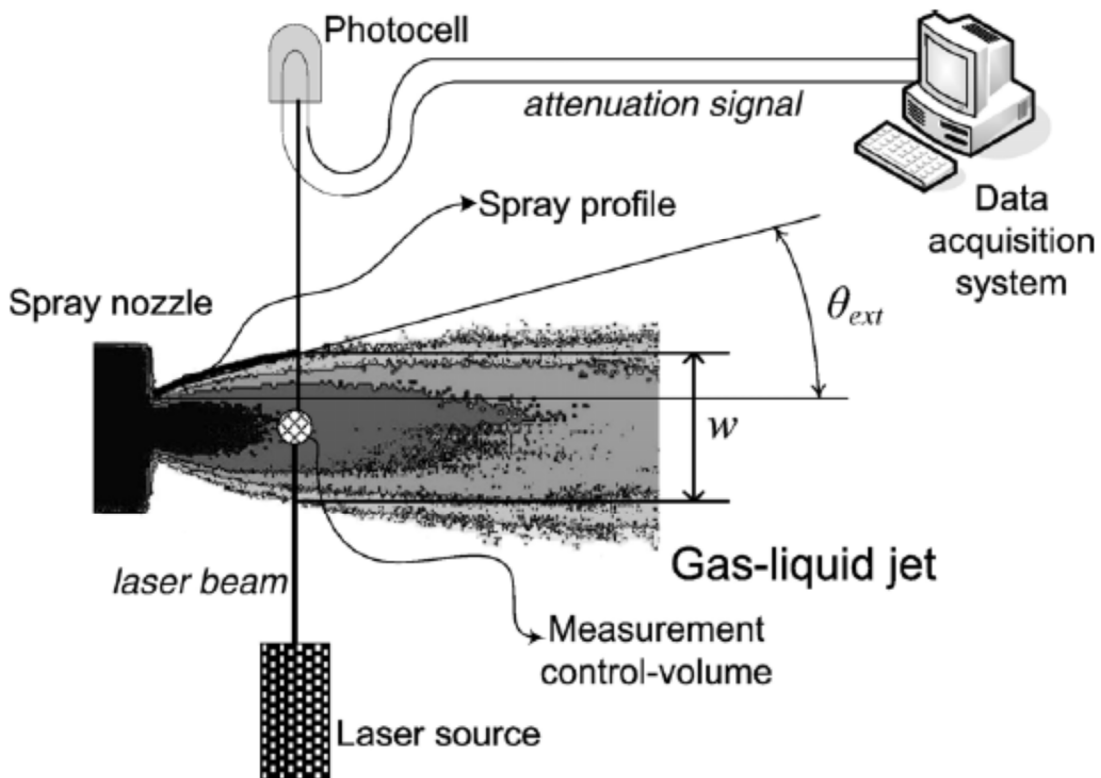


Figure 4.6 Laser-photocell arrangement used for open-air experiments (adapted from Portoghese et al. (2008)).

In order to estimate droplet diameters from the laser attenuation method, two major assumptions were adopted:

1- It is assumed that the sprayed liquid droplets are equi-sized spheres.

2- The number of droplets projected in the cross-sectional area of the control volume shown in Fig. 4.6 is the same as the number of droplets in that control volume. This means that it is assumed that no overlapping occurs between droplets in the control volume and that all passing droplets have the same effect on laser attenuation.

The linear dependence of laser attenuation on the number of droplets is rationalized by using the two assumptions above, so that each droplet passing through the laser beam attenuates light in the same manner related to its size. The postulates that all droplets are equi-sized (assumption 1) and that droplets are not overlapping each other in the control volume (assumption 2) suggest that the attenuation changes linearly with the number of passing droplets, as assumed by Portoghese et al. (2008).

According to Portoghese et al. (2008), the liquid volumetric fraction can be expressed as:

$$\varepsilon_v = \frac{1}{1 + \frac{ALR \rho_l}{100 \rho_g}} \quad \text{Eq.4.3}$$

Based on the definition of liquid volumetric fraction, the following equation could also be used to estimate the liquid volumetric fraction:

$$\varepsilon_v = \frac{N_{cv} \cdot \pi \cdot d_l^3}{6 \cdot V_{cv}} \quad \text{Eq.4.4}$$

where  $N_{cv}$  and  $d_l$  are the number and diameter of liquid droplets in the control volume of volume  $V_{cv}$  shown in Fig. 4.4. A similar definition could be used to calculate the liquid fraction in cross-section area ( $\varepsilon_a$ ) of the control volume shown in Fig. 4.4:

$$\varepsilon_a = \frac{N_a \cdot \pi \cdot d_l^2}{4 \cdot A_b} \quad \text{Eq.4.5}$$

where  $N_a$  is the number of liquid droplets, positioned in the cross-sectional area of the control volume, and  $A_b$  is the cross-section area of the laser beam which is maintained constant by the laser emitting source. From the second assumption above and the relationship between  $V_{cv}$  and  $A_b$ , we can write:

$$N_a = N_{cv} \quad \text{Eq.4.6}$$

$$V_{cv} = A_b \cdot l \quad \text{Eq.4.7}$$

where  $l$  is the length of laser beam exposed to the liquid spray jet. The laser beam source was located as close as possible to the spray nozzle in order to ensure that the length of laser beam can be approximated reasonably as the spray nozzle diameter.

Combining equations (4.3) to (4.7), one arrives at the following equation for calculation of the droplet diameter:

$$d_l = 1.5 \times \left( \frac{1}{\left(1 + \frac{ALR}{100} \times \frac{\rho_l}{\rho_g}\right) \cdot \varepsilon_a} \right) \times l \quad \text{Eq.4.8}$$

When droplets passed through the laser beam, signals were attenuated and transmitted from a photo cell to the data acquisition system, as shown in Fig. 4.6. The LabView module from National Instruments was utilized to process the signals and to construct voltage vs. time curves. In order to relate the generated voltage to the droplet diameter, a calibration procedure was needed. With no droplet passing through the laser beam, the generated signal corresponds to  $\varepsilon_a = 0$ , whereas, when the entire cross-section of the laser beam is occupied by liquid, the attenuation signal corresponds to  $\varepsilon_a = 1$ . For the experimental case when there is liquid injection, the attenuation lies between the two limiting values corresponding to  $\varepsilon_a = 0$  and  $\varepsilon_a = 1$ .

As depicted in Fig.4.7b, the  $\varepsilon_a = 1$  condition was approximated by deliberately blocking the whole cross-section of laser beam by placing paper in front of the laser beam source and measuring the voltage. This value, together with the value corresponding to  $\varepsilon_a = 0$ , were used to construct the calibration curve. Linear behaviour was assumed for the attenuation versus number of passing droplets as described earlier. Therefore, linear fitting was used to construct the curve shown in Fig. 7c. The liquid injection was initiated after 5 s for the same conditions as described in section 4.3.1. Experimental results are shown in Fig. 4.7a, The signals show oscillations around a mean value of 0.16V. With the aid of the calibration curve, the mean droplet diameter was estimated (using Eq. 4.8) to be 130  $\mu\text{m}$ .

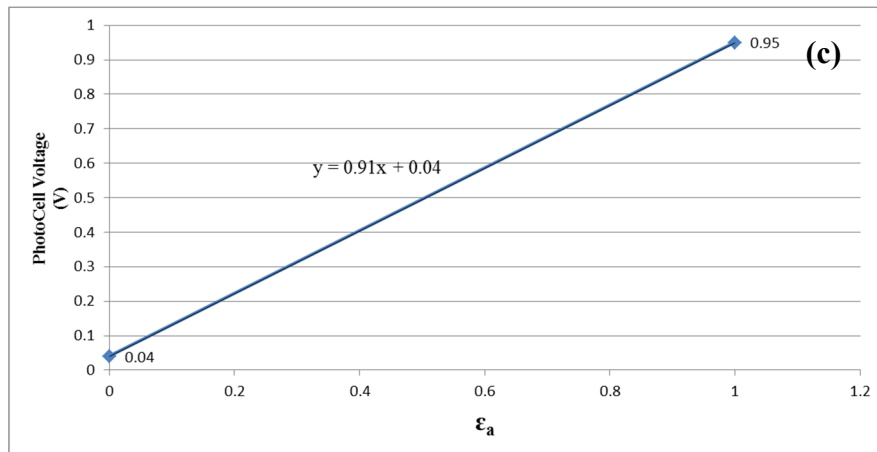
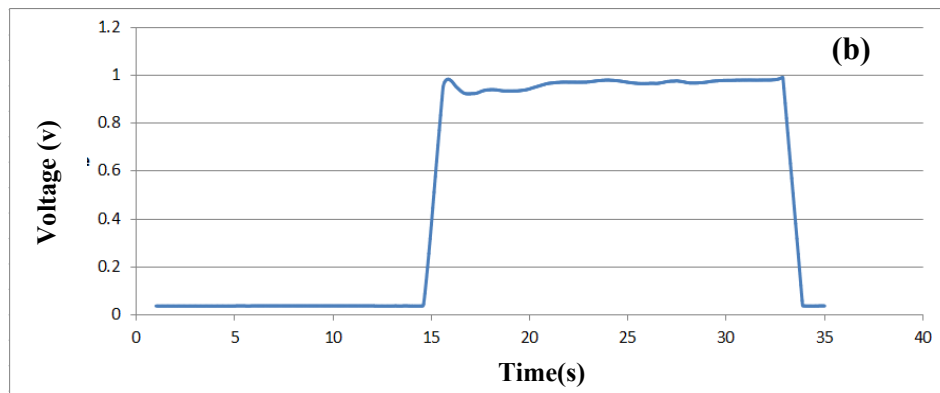
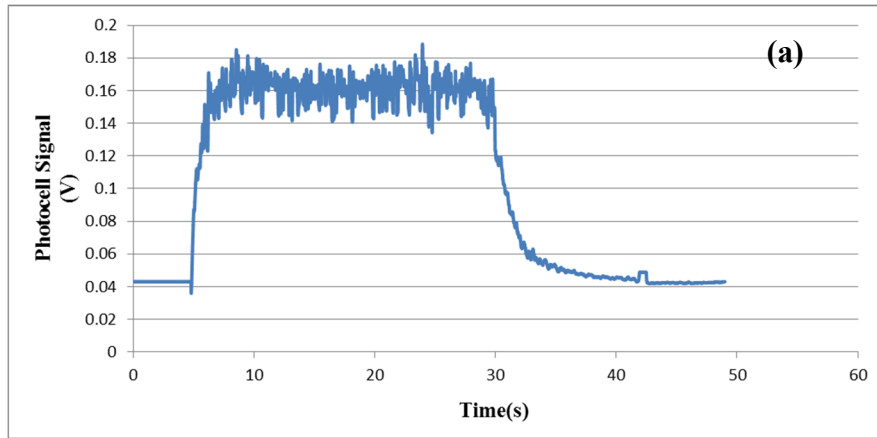


Figure 4.7 Laser-photocell curves used for the open-air experiments. (a) Experimental values for injection of 200 ml of Ethanol initiated at  $t=5$  s, (b)  $\epsilon_a = 0$  for  $t \leq 15$  s and  $\epsilon_a = 1$  for  $15 < t < 35$  s, (c) Calibration linear curve.

## **4.6 Liquid injection experiments (ethanol)**

There were two major criteria for selection of the liquid to be injected: low heat of vaporization and appreciable sensitivity to capacitance measurements. Although simple hydrocarbons like pentane have low heats of vaporization, ethanol (95 wt. %) was selected due to its much greater capacitance sensitivity.

### **4.6.1 Experimental procedure**

Different volumes of ethanol (150 and 200 ml) were injected at superficial gas (nitrogen) velocities of 0.10 to 0.20 m/s for sand and 0.15 to 0.30 m/s for FCC. Physical properties and dimensions are listed in Table 4.1. In each test, the bed was fluidized at a constant superficial gas velocity, and liquid was then injected after 150 s of fluidization for durations of both 30 s to inject a total of 200 ml, and 23 s to inject 150 ml of ethanol, respectively. The fluidization was then maintained for a relatively long time (1000 to 2000 s), with capacitance data continuously recorded.

Three to four particle samples in the case of sand and eight to ten in the case of FCC, were withdrawn from the bed through the sample port shown in Fig. 4.2. All samples were withdrawn after injection of the liquid. Samples were immediately taken to be tested for the moisture content by a HB43-S Halogen moisture analyzer manufactured by Mettler Toledo. In this manner, the vaporization effect was considered when constructing the calibration curves to relate the local free moisture to the measured capacitance.

**Table 4.1 Physical properties and dimensions for injection experiments**

<b><u>Property</u></b>	<b><u>Value</u></b>
Superficial gas velocity	0.10 to 0.20 m/s for sand; 0.15 to 0.30 m/s for FCC
Sauter-mean-diameter (SMD) of particles	185 $\mu\text{m}$ for sand, 70 $\mu\text{m}$ for FCC
Liquid droplet diameter	130 $\mu\text{m}$
Particle density	2650 $\text{kg/m}^3$ for sand, 1600 $\text{kg/m}^3$ for FCC
Column width	0.10 m
Column length	0.49 m
Column height	0.92 m
Static bed height	0.41 m
Column temperature	Ambient ( $\sim 25^\circ\text{C}$ )
Column Freeboard pressure	Atmospheric

#### **4.6.2 Experimental data on capacitance and liquid content**

When using the capacitance measuring technique, local capacitance readings were obtained for each electrode as shown in Fig. 4.1. However, these data are not useful unless one can relate them to the local liquid content inside the bed. Mohagheghi et al. (2013) reported in literature that capacitance value changes linearly with variations of moisture content inside the bed. As a first step, the local capacitance data were normalized by:

$$C_{\text{Norm}} = \frac{C_{\text{Measured}}}{C_{\text{Dry}}} \quad \text{Eq.4.9}$$

where “Dry” corresponds to the period prior to injection when there was no liquid in the bed and “Measured” values are local capacitance readings before and after liquid injection at a data sampling rate of 10 Hz. Therefore, the normalized capacitance before injection was 1.0, and it is reasonable to expect  $C_{\text{Norm}}$  to be  $> 1.0$  just after injection, decreasing to 1.0 gradually during the drying period. This behavior is depicted in Figures 4.8 and 4.9 for two of the cases studied in this work where liquid injection was initiated after 150 s. The ordinate axis in Fig. 4.8 shows the average normalized capacitance, which is the mean value of  $C_{\text{Norm}}$  calculated from all 20 electrodes. The fluctuations in this figure are due to gas mixing inside the bed and bubbles passing through the bed. The bubbles decreased the local capacitance, resulting in lower normalized capacitance.

As shown in Figs 4.8 and 4.9, ethanol vaporized very quickly in sand compared to FCC. The bed was completely dry after 350s for sand, whereas in the case of FCC, it took considerably longer to dry the bed. The likely reason is that the FCC particles were porous, imbibing a considerable amount of liquid inside the pores which then required more time to vaporize. Greater wettability and faster liquid mixing in the FCC bed might also have played key roles, as discussed in the next paragraph.

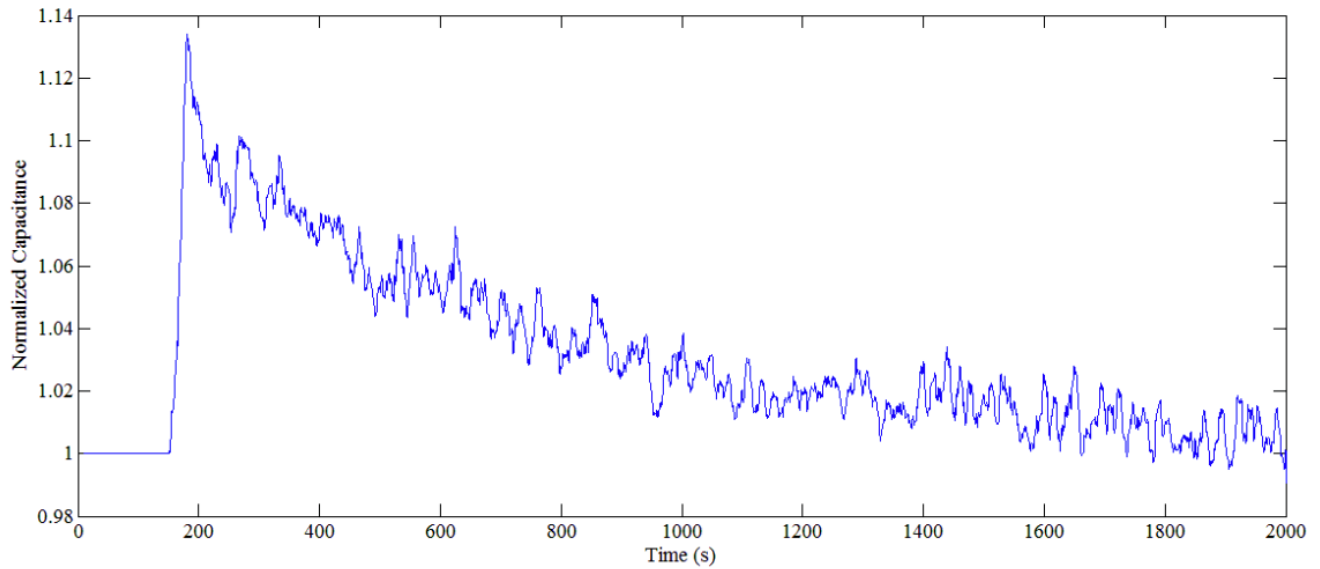


**Figure 4.8 Normalized capacitance vs. time for FCC and ethanol (Injection started at  $t=150$  s with a liquid flowrate of  $0.0004$   $\text{m}^3/\text{min}$ , superficial gas velocity =  $0.2$   $\text{m/s}$ .)**

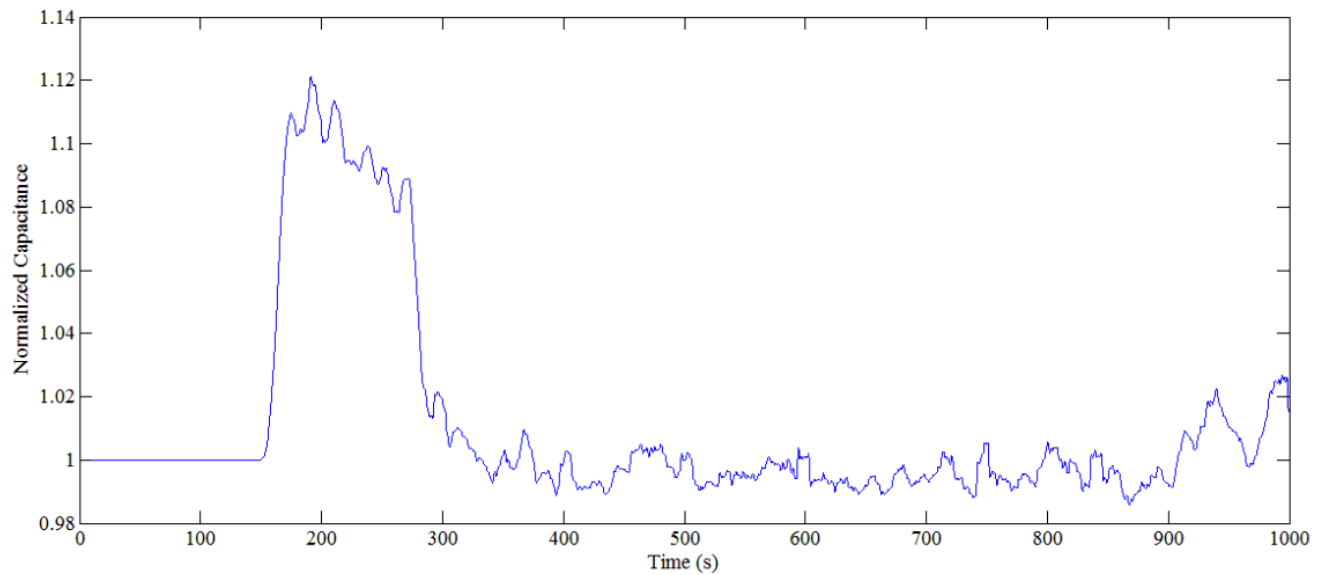


**Figure 4.9 Normalized capacitance vs. time for sand and ethanol (Injection started at  $t=150$  s with a liquid flowrate of  $0.0004$   $\text{m}^3/\text{min}$ , and superficial gas velocity =  $0.2$   $\text{m/s}$ .)**

A better understanding of the mixing effect can be obtained from the normalized capacitance contours shown in Fig. 4.10, which are based on time-averaged normalized capacitance data. Comparing the FCC fluidized bed to the sand bed shows that mixing was

significantly faster with FCC, making the FCC bed more homogenous. In the case of sand, mixing was relatively slow and the distribution of liquid inside the bed was not as homogenous as for FCC. The reason was investigated using the Washburn method (Czachor 2007; Galet et al. 2010) for wettability. This method uses the capillary rise data of liquid in a sample bed of particles which is analyzed using the previously determined parameters to obtain the contact angle. It was concluded that sand is not wettable by ethanol, whereas FCC is almost perfectly wetted by ethanol. This issue was not addressed by Bruhns (2002) nor by Bruhns and Werther (2005) who investigated the injection into a quartz sand fluidized bed. Because of the poor wettability, quantitative analysis of ethanol injection into a sand bed was not considered further in the present work.

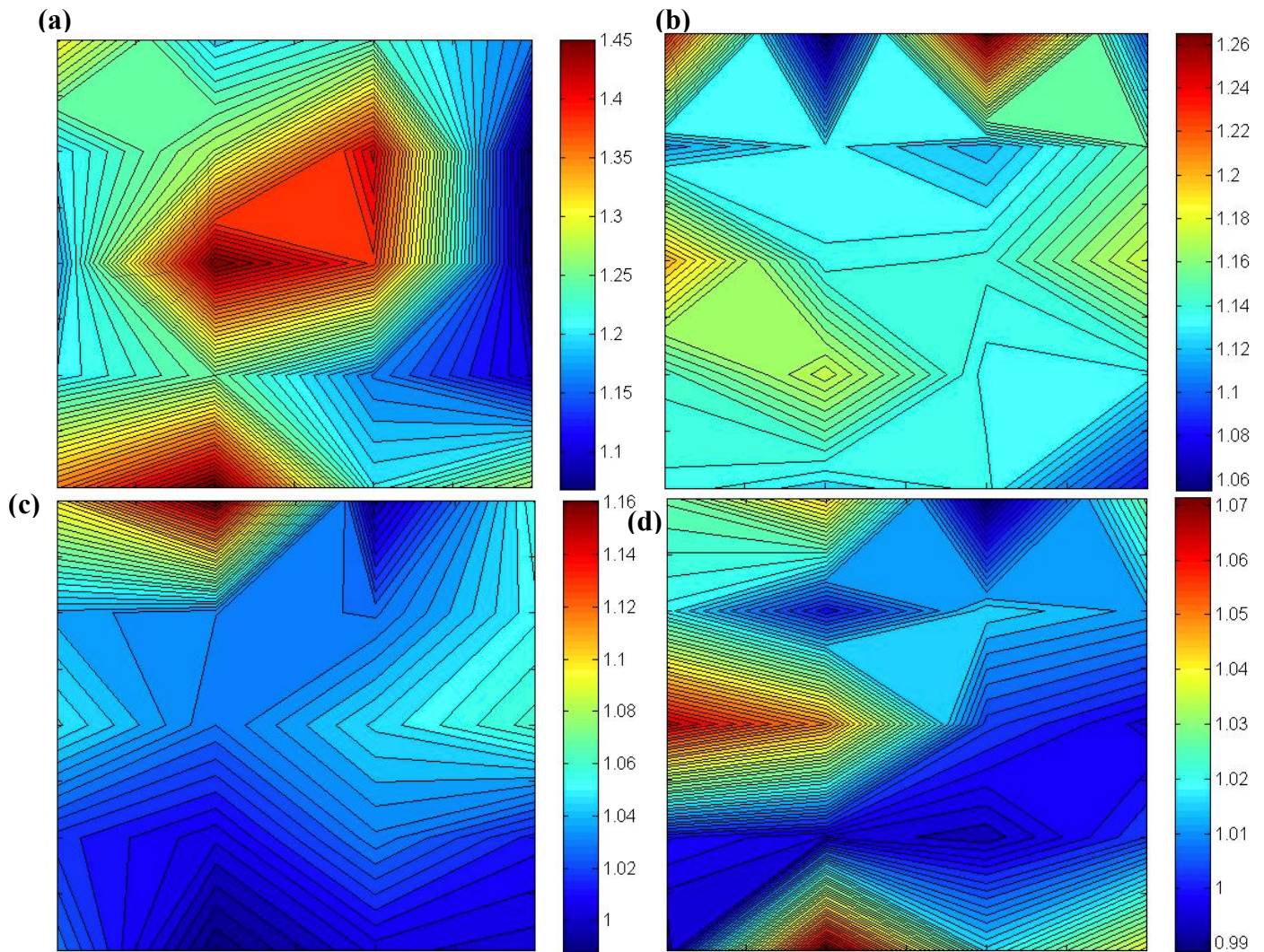


**Figure 4.10 Time-averaged local normalized capacitance of whole bed (after injecting 200 ml ethanol at  $t = 150$  s for duration of 30 s at superficial gas velocity of 0.2 m/s). (a) and (b): FCC (averaged from  $t=160$  to 180s and 220 to 240 s respectively), (c) and (d): sand (averaged from  $t=160$  to 180s and 220 to 240 s, respectively).**

Liquid content measurements are required to relate the normalized capacitance readings to the amount of moisture inside the bed. Small laboratory sample boxes were used to collect wet FCC discharged from the sampling port shown in Fig. 4.2. This port was opened at time intervals shown in Table 4.2 (after liquid injection) for a duration of less than 5 s to completely fill the

sample box. Samples were then immediately transported to the analytical lab to determine their moisture contents by a moisture analyzer.

The HB43-S Halogen Mettler Toledo moisture analyzer, displayed (and printed) the moisture content of each sample as a percentage of the dry weight. The results were printed out as "%M" (Moisture Content) (e.g. -2.33 %M) and shown as negative values. During drying, the current measured value was continuously displayed as a percentage, and a final value was shown after about 5 minutes of drying, representing the actual M% of the sample. The M% can be interpreted as liquid-to-solid ratio of the sample, given by:

$$M\% = - \frac{\text{Wet mass (g)} - \text{Dry mass (g)}}{\text{Dry mass (g)}} \times 100\% \quad \text{Eq.4.10}$$

For each test, the M% readings should be calibrated based on the moisture content of a sample before liquid injection ( $M_0$ ) according to:

$$M_{\text{calibrated}}\% = M_{\text{Measured}}\% - M_{\text{initial}}\% \quad \text{Eq.4.11}$$

This was applied separately for each experiment to improve the accuracy. The moisture content of dry particles (taken from the bed before fluidization) is represented in Eq. 4.11 as " $M_{\text{initial}}\%$ ". In the case of the FCC particles, the effect of moisture in the initial sample was significant due to humidity inside the FCC pores.

The frequency of sampling, together with the amount of liquid injected, superficial gas velocity and measured liquid-to-solid ratio for FCC and ethanol are summarized in Table 4.2. The dashed lines in some columns indicate that the readings were inaccurate or taken at different times. The data clearly show that the liquid-to-solid mass ratio depended on the superficial gas velocity.

**Table 4.2 Liquid-to-solid mass ratio measurements at different superficial gas velocities for FCC/ethanol system with properties listed in Table 1 (22 kg of FCC inventory)**

Case No.	U (m/s)	Vol. of Inj. Liq. (ml)	Liquid-to-solid mass ratio ( $M_{\text{calibrated}}\%$ ) measured at sample times (minutes after injection of ethanol that lasted 23 s for 150 ml and 30 s for 200 ml injections)									
			5min	6min	7min	9min	10min	12min	16min	17min	20min	26min
			Sample #1	Sample #2	Sample #3	Sample #4	Sample #5	Sample #6	Sample #7	Sample #8	Sample #9	Sample #10
a	0.15	150	-	0.34	0.25	-	0.24	-	-	0.17	-	0.00
b	0.20	200	0.50	0.44	0.41	0.35	-	0.34	0.23	-	0.18	0.16
c	0.25	200	-	0.60	0.54	0.45	-	0.44	0.34	-	0.20	0.11
d	0.30	200	1.27	1.15	1.10	1.02	-	1.00	-	-	-	-

Fig. 4.11 plots the data from Table 4.2 for three fluidization velocities. Of primary interest are the higher liquid-to-solid ratios for a superficial gas velocity of 0.30 m/s compared to the two lower gas velocities. This could result from a temporary flow regime change inside the bed resulting in more rapid mixing of liquid, causing a larger portion of liquid to enter the FCC pores.

The trend lines for each data series indicate that when the superficial velocity increased, the rate of change of liquid-to-solid mass ratio also increased. Since the liquid injections occurred over quite brief periods of time (lasting only about 20-30 s) at a high ALR, significant formation of agglomerates is unlikely. Therefore, the drying mechanism which leads to vaporization of liquid is thought to be mainly from liquid inside the pores and then the film around the particles. The noticeable effect of superficial gas velocity on drying seems to not only affect the convection drying from the outer surface of the particle, but also vaporization from

inside the pores. For  $U = 0.3$  m/s, the data appears to be non-linear. This issue is further studied in Chapter 5 where CFD modeling is utilized to investigate a similar case.

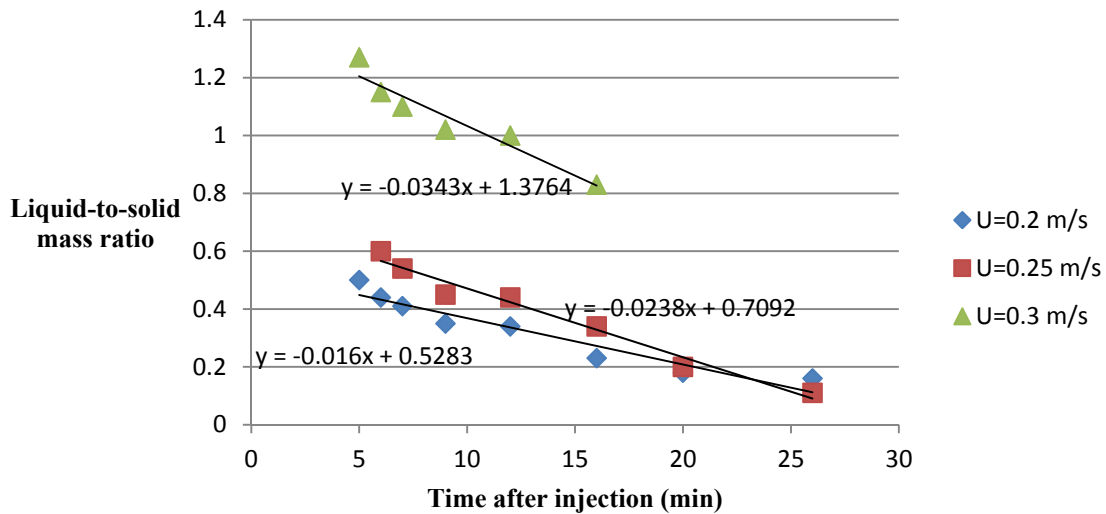


Figure 4.11 Liquid-to-solid mass ratio measurements vs. time after adding 200 ml of ethanol.

### 4.6.3 Small box experiments

The relation between normalized capacitance and liquid content of solid particles was further investigated by means of “small box experiments”. The purpose was to provide a calibration procedure, as discussed further in section 4.6.4. In these experiments, liquid was spread evenly on the solid particles with mechanical agitation, using a hand mixer similar to that in the schematic in Fig. 4.12. As indicated in Fig. 4.12, 5 to 10 ml of ethanol was well mixed using an agitator with  $0.008 \text{ m}^3$  of FCC in a bucket to ensure an even spread and to facilitate liquid penetration into particle pores. A sample was then taken, using a small laboratory sample box, immediately after mixing, for moisture content testing, and the rest was dumped into a small cubic plastic box (100 x 100 x 100mm) which had two flat metal electrodes, centered on

opposite side walls and entirely covering the side walls. These electrodes were connected to the same capacitance measuring system as described in Fig.4.2.

In this manner, the normalized capacitance data presented in section 4.6.2 corresponding to the content of liquid in FCC particles inside the box, were obtained from the measuring system. At the same time, the liquid content was measured in the analytical lab using the moisture analyzer described in section 4.6.1. The test was repeated with 5 to 10 ml of ethanol, to obtain enough data to relate normalized capacitance to actual liquid content in the FCC particles.

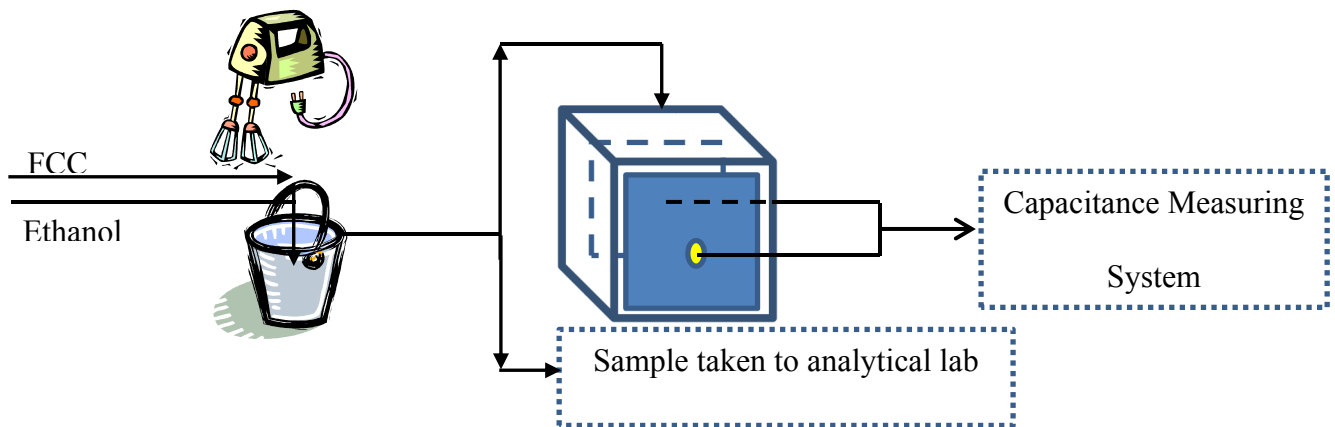


**Figure 4.12 Schematic showing small box experiment for FCC/ethanol system.**

The results are fitted on the curve in Fig. 4.13. The data indicate that a linear fit reasonably captures the relation between normalized capacitance and moisture content. The fitted correlation was utilized further to estimate the moisture content from capacitance data, as described in the next section.

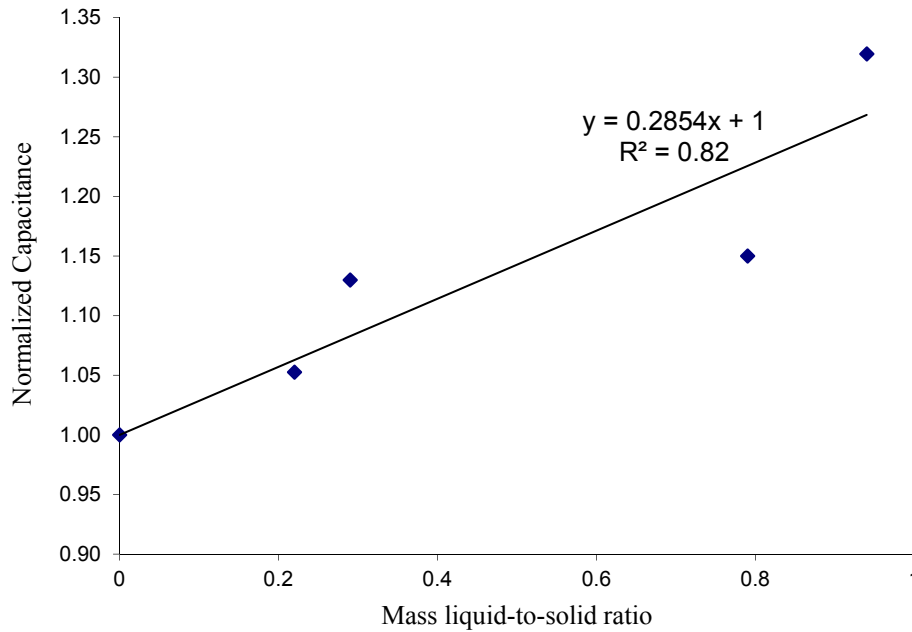


**Figure 4.13 Calibration curve from FCC/ethanol small box experiments for relating normalized capacitance data to liquid content.**

#### **4.6.4 Normalized capacitance vs. liquid content**

For cases 2 and 3 in Table 4.1, capacitance data were extracted from the measuring system through a pre-written MATLAB code. The capacitance data were then normalized based on the procedure outlined in section 4.6.1 for each electrode at the times indicated in Table 4.2.

In Table 4.2 it was initially expected that one would observe higher normalized capacitance at each electrode for higher superficial gas velocity. This expectation reflected the higher liquid content achieved from sampling and was also based on the assumption of perfect liquid mixing<sup>3</sup> inside the bed. However, the normalized capacitance at each electrode did not

---

<sup>3</sup> The term “liquid mixing” in this chapter refers to the homogeneity of liquid-solid mixture in the bed resulting from contact between liquid and particles.

follow the expected trend. Some electrodes exhibited higher normalized capacitances when the superficial velocity increased, while others showed lower values.

A tentative reason could be that the assumption of perfect liquid mixing is not valid for the FCC fluidized bed and that varying the fluidization velocity affected the extent of liquid mixing. This implies that the amount of liquid injected into the bed was insufficient to cover all particles. Vaporization and imbibition into the pores are likely to have been the dominant mechanisms that contributed to non-perfect mixing in the bed. In the water injection experiments of Mohagheghi et al. (2013), perfect liquid mixing was reported for conditions where wettability and low vapor pressure of water contributed to better liquid-solid homogeneity in the bed. However, a volatile liquid (e.g. ethanol), which evaporates much more quickly than water, would affect the liquid mixing differently inside the bed. Part of the reason could be non-homogenous vaporization of ethanol in different regions of the bed. In addition, the FCC particles are much more porous than the coke particles tested by Mohagheghi et al. (2013), possibly contributing to different liquid mixing behaviour inside the bed. This possible explanation was further supported by the measured capacitance data for different superficial gas velocities.

Taking this less-than-perfect liquid mixing behaviour into account, it is anticipated that the measured liquid content from sampling is not representative of liquid content in the entire bed, but shows the amount of liquid near the sampling port. In order to check this assumption, the normalized capacitance data, corresponding to the measured liquid content from the samples in Table 4.2, are calculated using the calibration curve discussed in section 4.6.3. The calculated values are taken as the overall mean from all 20 electrodes. They are then compared to the normalized capacitance data, obtained using the measurement system shown in Fig 4.2 at each electrode inside the bed. The Root-Mean-Square (RMS) deviations of this comparison, selected

for five samples out of ten in Table 4.2, are depicted in Table 4.3 for a superficial velocity of 0.15 m/s, and in Table 4.4 for  $U = 0.2$  m/s. The sample numbers in these tables are the same as in Table 4.2.

**Table 4.3 Root-Mean-Square (RMS) deviations of measured normalized capacitance data at all 20 electrodes from the actual data read from calibration curve at different sampling times for case #1 in Table 4.2 (superficial gas velocity = 0.15 m/s, injected ethanol volume = 150 ml). Electrode positions are shown in Fig 4.1.**

	Sample #2	Sample #3	Sample #5	Sample #8	Sample #10
Elect. 1	0.049	0.053	0.042	0.058	0.039
Elect. 2	0.046	0.060	0.046	0.052	0.038
Elect. 3	0.033	0.044	0.049	0.044	0.031
Elect. 4	0.029	0.022	0.019	0.026	0.022
Elect. 5	0.032	0.027	0.025	0.030	0.125
Elect. 6	0.173	0.137	0.055	0.125	0.187
Elect. 7	0.045	0.025	0.038	0.044	0.021
Elect. 8	0.047	0.031	0.044	0.033	0.033
Elect. 9	0.070	0.038	0.031	0.032	0.021
Elect. 10	0.062	0.044	0.048	0.046	0.044
Elect. 11	0.051	0.053	0.035	0.037	0.080
Elect. 12	0.029	0.026	0.031	0.031	0.021
Elect. 13	0.040	0.032	0.038	0.042	0.033
Elect. 14	0.025	0.035	0.037	0.038	0.031
Elect. 15	0.033	0.027	0.040	0.050	0.022
Elect. 16	0.050	0.019	0.036	0.040	0.011
Elect. 17	0.051	0.022	0.038	0.047	0.014
Elect. 18	0.056	0.043	0.044	0.054	0.026
Elect. 19	0.062	0.041	0.050	0.040	0.017
Elect. 20	0.066	0.043	0.062	0.044	0.027

**Table 4.4 Root-Mean-Square (RMS) deviations of measured normalized capacitance data at all 20 electrodes from the actual data read from calibration curve at different sampling times for case #2 (superficial gas velocity = 0.2 m/s, injected ethanol volume = 200 ml). Electrode positions are shown in Fig 4.1.**

	Sample #1	Sample #2	Sample #3	Sample #4	Sample #6	Sample #7	Sample #9
Elect. 1	0.093	0.286	0.087	0.076	0.103	0.090	0.088
Elect. 2	0.076	0.076	0.063	0.066	0.073	0.060	0.063
Elect. 3	0.067	0.060	0.069	0.065	0.071	0.057	0.067
Elect. 4	0.058	0.031	0.051	0.044	0.041	0.033	0.051
Elect. 5	0.072	0.047	0.065	0.059	0.054	0.045	0.091
Elect. 6	0.147	0.130	0.225	0.110	0.172	0.114	0.298
Elect. 7	0.065	0.066	0.065	0.054	0.041	0.039	0.055
Elect. 8	0.052	0.054	0.071	0.044	0.058	0.041	0.048
Elect. 9	0.064	0.080	0.064	0.053	0.052	0.045	0.060
Elect. 10	0.127	0.128	0.150	0.104	0.108	0.092	0.109
Elect. 11	0.075	0.054	0.074	0.100	0.060	0.063	0.074
Elect. 12	0.082	0.061	0.066	0.069	0.046	0.060	0.085
Elect. 13	0.068	0.088	0.064	0.045	0.051	0.032	0.066
Elect. 14	0.065	0.071	0.058	0.035	0.049	0.036	0.058
Elect. 15	0.072	0.080	0.211	0.050	0.054	0.051	0.068
Elect. 16	0.048	0.036	0.045	0.042	0.042	0.024	0.036
Elect. 17	0.064	0.050	0.059	0.057	0.049	0.026	0.047
Elect. 18	0.080	0.055	0.056	0.071	0.048	0.029	0.041
Elect. 19	0.095	0.079	0.079	0.059	0.054	0.028	0.047
Elect. 20	0.084	0.069	0.129	0.242	0.042	0.026	0.037

Comparison of Table 4.3 and 4.4 indicates that lower deviations were observed at the lower superficial velocity. For the higher velocity of 0.2 m/s, the data differ considerably from electrode to electrode, confirming the earliest observations of imperfect liquid mixing in the bed. Electrode no. 16, located immediately above the sampling port (see Fig. 4.1), had the smallest

deviations for most sampling times in Table 4.3. According to the procedure followed during sampling, the sampling valve was opened abruptly at the specified sampling time and remained open for less than 5 s to completely fill the small sampling box. This duration allowed the particles to flow down from the top of the sampling port and reach the sampling box. That could be why electrode 16, which is immediately above the sampling port, shows the closest values to the measured data.

Higher deviations observed for a superficial velocity of 0.2 m/s could be due to the effect of short-lived agglomerates which are likely to be created more frequently and observed more often at higher gas velocities. In the small box experiments described in section 4.6.3, agglomerates could not form due to mixing the bed manually (see Fig. 4.12) which differs from the mechanism of mixing in the fluidized bed. The complex effects of imbibition into the pores and evaporation, which are more prominent at higher superficial gas velocities due to more particle-droplet and particle-particle collisions, may also be factors causing higher deviations.

The following procedure was followed to obtain quantitative data for liquid content inside the bed:

- 1- The measured capacitance data were normalized using Eq. 4.9. Normalized values equal to 1 correspond to a dry bed, whereas higher values indicate the presence of liquid.
- 2- For superficial gas velocities of 0.15 and 0.2 m/s, the calibration line shown in Fig. 4.13 was used to estimate the corresponding liquid-to-solid mass ratio. This was repeated for all time intervals to find the liquid content at all 20 electrodes.

Following the procedure described above, the changes of the liquid-to-solid ratio at two different superficial gas velocities with time, averaged for all 20 electrodes, are depicted in Fig. 4.14. For the higher superficial gas velocity (0.2 m/s), the liquid content reached a greater value at the beginning of injection and dried more rapidly, consistent with the results in Fig. 4.11.

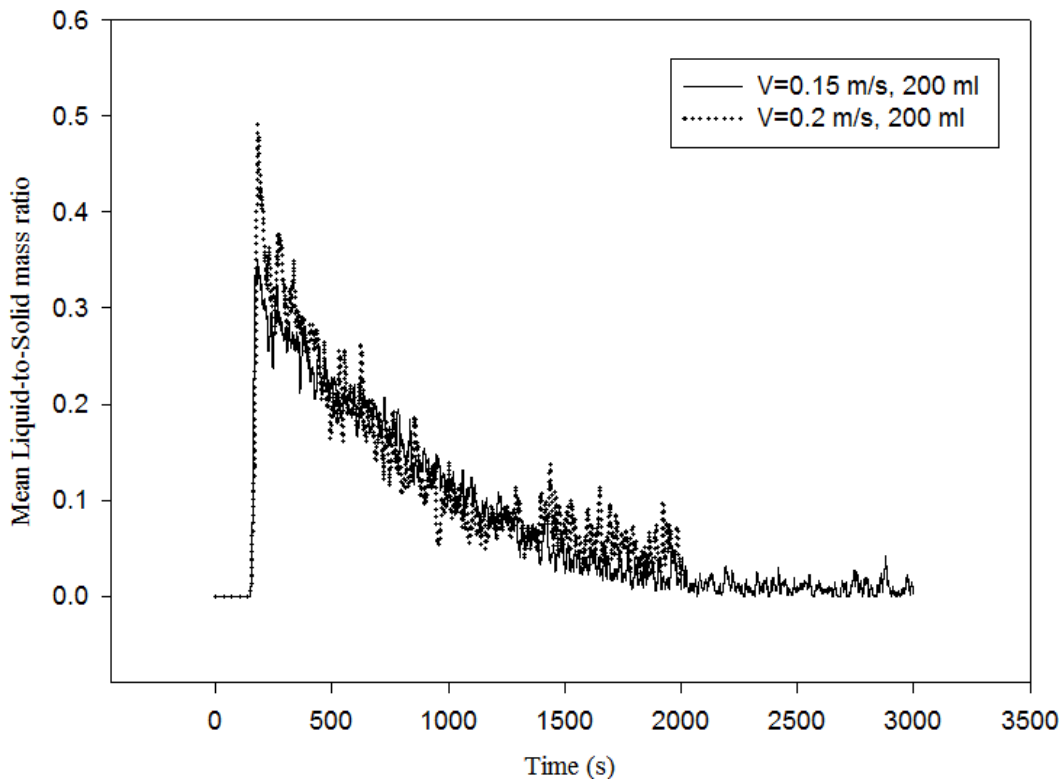


**Figure 4.14 Mean liquid-to-solid mass ratio measurements of all 20 electrodes vs. time at different superficial gas velocities for injection of 200 ml ethanol over a time span of 30 s.**

#### **4.7 Liquid distribution inside FCC pores**

One of the main objectives of the present study was to understand the effect of FCC particle porosity on liquid distribution inside the bed. During the experiments, it was observed that injection of the same liquid volume into a bed fluidized at different superficial gas velocities resulted in different liquid contents in the bed.

In order to investigate this issue further, the HB43-S Halogen moisture analyzer by Mettler Toledo, used in section 4.6.1, was again utilized. The fluidization system was the same as the set-up whose properties are listed in Table 4.1, with superficial velocities of 0.20 and 0.25 m/s. Liquid injection was initiated 150 s after fluidization began and lasted about 30 s. 100 s after termination of liquid injection, a sample was withdrawn from the sampling port (see Fig. 4.1) and immediately taken to the analytical lab for moisture content determination, similar to the procedure described in section 4.6.1. Drying kinetics were determined by inspecting the FCC drying curves, allowing the portion of the injected ethanol which entered the FCC pores to be estimated.

The moisture removal for the system with a superficial gas velocity of 0.20 m/s, shown in Fig. 4.15, was determined at each step by multiplying the given M% by the dry weight reported by the HB43-S at the end of the experiment. As shown in Fig. 4.15, the moisture content followed a non-linear curve. The section with a steep slope corresponds to evaporation of interstitial liquid, whereas the lower slope section (starting after 50-100 s) is believed to correspond to moisture removal from inside the FCC pores.

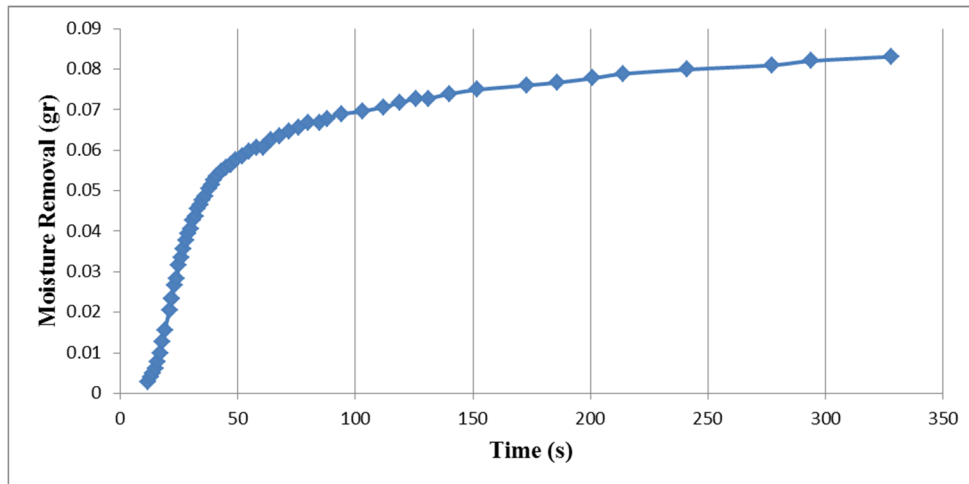


**Figure 4.15 Moisture removal of sample vs. Time (Drying curve) for superficial gas velocity of 0.20 m/s after injection of 200 ml ethanol.**

It was observed that at superficial gas velocities of 0.20 and 0.25 m/s, most liquid was not distributed in the pores, but as interstitial liquid. However, increasing the superficial velocity seems to have affected this distribution, as shown in Table 4.5. This is consistent with initial observations in the injection experiments where in-pore moisture content was higher for a higher superficial gas velocity.

A tentative reason could be the effect of superficial gas velocity on solid-liquid mixing inside the bed. As the velocity increases, a larger portion of the interstitial liquid is likely to be absorbed inside FCC pores resulting in more liquid in the pores. This ultimately results in extended liquid vaporization time inside the bed, as observed in the experiments.

**Table 4.5 Liquid distribution in pores and in interstices**

Superficial gas velocity	Amount of ethanol injected	Percent of Liquid content in Sample 1: 4 min after injection	Percent of Liquid content in Sample 2: 7 min after injection
0.20 m/s	200 ml	Pores: 30% Interstitial: 70%	Pores: 33% Interstitial: 67%
0.25 m/s	200 ml	Pores: 33% Interstitial : 67%	Pores: 42% Interstitial : 58%

#### **4.8 Conclusions**

Liquid ethanol was injected into fluidized beds of FCC and sand. The results indicated that little or no wetting was obtained when ethanol was injection into a bed of sand, Hence analysis was carried out only for injection into FCC. The effects of fluidization velocity and internal FCC porosity were investigated in this study and it was found that:

- 1- In the case of injection of a volatile liquid (ethanol), if the injection time is relatively small or the amount of liquid injected into the bed is not enough to cover all particles, the assumption of perfect liquid-solid mixing is not appropriate. This was concluded by comparing liquid measurements from normalized capacitance measurements on samples taken at the sampling port (see Fig. 4.1).
- 2- Elevating the gas superficial velocity resulted in detection of more liquid inside internal pores, and consequently higher moisture content inside the FCC particles.
- 3- An approach was proposed to quantify the liquid-to-solid mass ratio inside the bed based on capacitance measurements. The quantitative results confirmed earlier

observations, showing that higher gas superficial velocity resulted in faster drying and more liquid content inside the particles. These results give some insight into the underlying mechanisms of liquid imbibition into pores and evaporation inside the bed, studied further in Chapter 5.

## **Chapter 5: Liquid Imbibition/Vaporization Model in Porous Media**

### **5.1 Background**

The purpose of this chapter is to study distribution and vaporization of liquid injected into a fluidized bed containing FCC particles using numerical techniques. CFD simulations were conducted based on existing models, modified to more fully capture the physics of the experiments described below. Different simulations were performed with operating conditions matching those used to obtain experimental data, for injection of liquid into the bed.

### **5.2 Experiments**

Experiments were conducted by collaborating partners at British Columbia Research Institute (BCRI) in a two-dimensional column containing FCC particles as depicted in Fig. 5.1. Because the experiments relevant to this chapter were done for a commercial client, it is not possible to fully describe all details of the equipment and results. The liquid evaporation was monitored by continuously measuring the concentration of evaporated liquid (ppmv) in the vapor phase at two sampling points, SP4 and SP5, shown in Fig. 5.1. Evaporated liquid concentrations were measured using thermal conductivity detectors (TCDs) at sampling rate of 1 Hz. Heptane (98% wt.) was used in these experiments as a model liquid for industrial tests. Hence, heptane is the liquid considered in this chapter. The liquid injection was initiated 120 s after fluidization and continued for 73 minutes. The injection was stopped and the bed was allowed to dry for 53 minutes. It is not feasible to consider the complete process due to the long run-time of the experiments. Therefore, in this chapter the whole process of liquid injection experiments is divided into three stages:

A) Liquid injection starts into a dry bed with liquid film forming around the particles and then imbibed into particle pores. The simulation results are then analyzed in section 5.6.1.

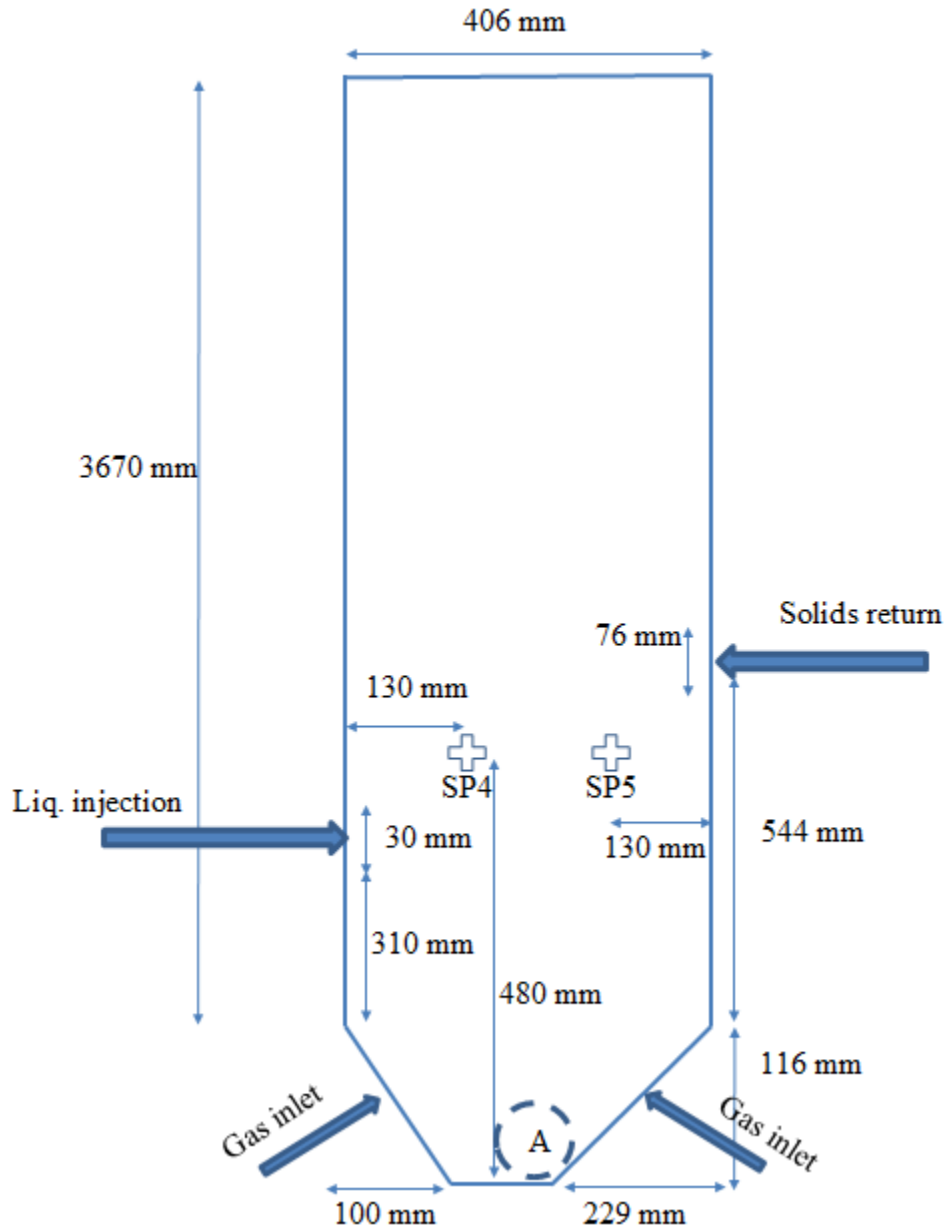


Figure 5.1 Experimental setup and location of sampling points SP4 and SP5 which are on the same face of the column.

B) Liquid injection continues beyond the state where all particle pores are saturated with liquid. It is assumed that there is no further imbibition and evaporation is driven by convection from the outer surface of the particles to the surrounding air. The results are discussed in section 5.6.2 below.

C) Liquid injection stops, and the bed is allowed to dry. There is initially no liquid film around the particles, and evaporation is considered to take place from inside particle pores to the surrounding air.

CFD simulation studies are performed for stages A and B. The starting point of transition from state A to B was judged based on observations described in section 5.6.1. Experimental results obtained in section C were analyzed, and a methodology is proposed to capture the mechanism of drying in that stage. Uncertainties remain due to complexity of experiments, and the conclusions plus proposed approach in this chapter are based on a rational explanation of the results obtained from CFD and comparison with experimental data. Note that the interpretation of CFD results and explanations given for lack of agreement between CFD and experimental results in subsequent sections are based on the observed trends of experimental data obtained from BCRI.

A description of the model and details of the simulations are provided in the following sections, together with a comparison between simulation results and experimental data.

### **5.3 Physics**

Liquid-particle collision, film formation, imbibition and drying are shown schematically in Fig. 5.2. Recently, Terrazas-velarde et al. (2011a, 2011b) proposed a methodology to derive an equation to describe the relationship between “h” (liquid film height) and “y” (penetrating

liquid distance). In this work, the same methodology is followed to derive a new set of equations based on assumptions outlined in subsequent sections.

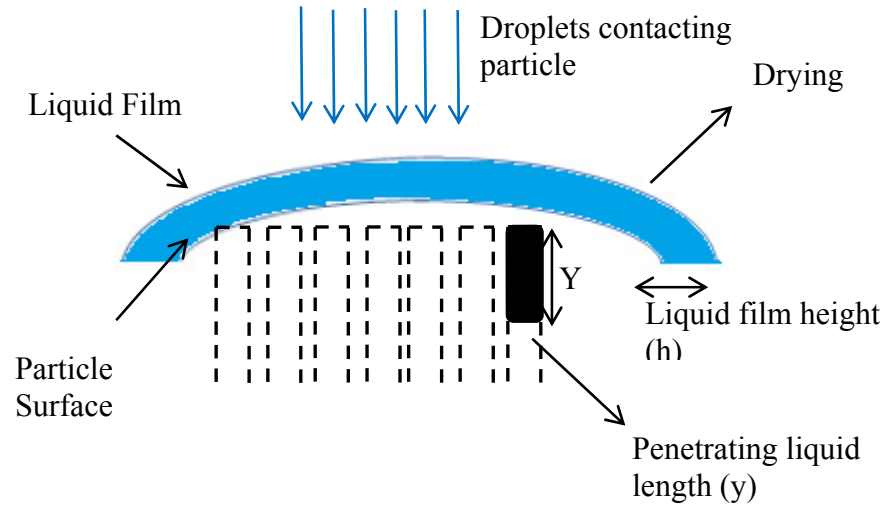


**Figure 5.2 Schematic of liquid film formation and penetration inside the pores.**

Liquid injection in an actual fluidized bed is a complex three-phase process. In order to model the process of liquid distribution in the bed, several simplifying assumption are required. Some assumptions in this section are based on previous experimental observations and studies by earlier research groups. The validity of these assumptions is later checked by conducting CFD simulations and comparison with experimental results.

Following the liquid injection and distribution, there are three different physical phenomena as follows, with assumptions listed in each part. These form the basis of derivations in subsequent sections:

- Assumptions for collisions:
  - The velocity of liquid spreading around a particle is assumed to be equal to the collisional velocity. This assumption is based on direct numerical simulations by

Ge and Fan (2006) in which the spreading speed of the liquid film on the particle surface was reported to be close to the initial impact velocity.

- The spreading velocity is assumed to be constant.
  - The liquid has perfect wettability on the surface of particles, resulting in dynamic and static contact angles equal to zero: Alkanes (including hexane and heptane) are low surface energy liquids, which completely wet the powders (Yildirim, 2001).
  - Particle density change due to liquid coating and imbibition is negligible
  - Upon collision and transfer of liquid, the liquid is distributed uniformly over all particles contacted by the liquid.
- Assumptions for imbibition:
    - Three types of liquid are considered in this work: liquid film around the particles free-liquid which is separated from the particle surface and imbibed liquid inside the pores.
    - Injection of liquid increases the liquid film thickness around the particle and imbibition starts immediately upon liquid film formation which is predicted based on a balance of forces as described in section 5.3.1 below. If the liquid film thickness satisfies the agglomerate<sup>4</sup> formation criteria discussed in section 5.3.4, the excess liquid is designated as agglomerate liquid, which cannot be imbibed, but is available for vaporization. The detailed mechanisms of agglomerate

---

<sup>4</sup> “Agglomerate” in Chapters 4 and 5 includes interface liquid that fills the space between particles and holds the particles together.

formation, breakup and interaction between agglomerates are complex and are not included in the present study.

- The mechanism determining imbibition involves a balance of capillary and viscous forces.
- Pores are modeled as equi-spaced cylinders with length equal to the particle diameter and pore diameter on the scale of nanometers. The pores are assumed to be open-ended, extending from one particle surface to the opposite particle surface.
- Imbibition is considered to take place from the liquid film on the surface of the particle to the center of the particle through cylindrical pores. The liquid film thickness decreases based on liquid evaporation and the balance between capillary and viscous forces, as described in section 5.3.1.
- Increased gas pressure in particle pores resulting from imbibition is not considered in this work.
- Assumptions for drying:
  - Drying is considered to be by mass transfer from the liquid film around wet particles and liquid droplets to the bulk of the gas, with negligible heat transfer resistance.
  - Liquid which penetrates into the pores is conserved and not available for transport to another particle. When there is liquid film around particle, it is assumed that no vaporization occurs from internal pores. Otherwise, liquid evaporation from pores is investigated as outlined in section 5.6.3.

- Due to time-scale differences, liquid first penetrates into the pores, and then the remaining liquid film undergoes drying.

Based on the physics and derivations described above and the liquid film growth criterion, the following sequential mechanisms are considered when modeling imbibition:

- 1- Injection starts at  $t=t_0$ . The particles are dry and there is no imbibition.
- 2- Liquid droplets reach the first group of particles, resulting in collision between droplets and dry particles.
- 3- The liquid reaching particles is distributed equally over all wetted particles in a control volume. This is simulated by utilizing the volume fractions of wet particles, obtained from the CFD solver, to calculate the number of wet particles and the corresponding initial liquid layer covering all wet particles. The liquid is transferred by two mechanisms: from liquid phase to dry particles, transforming dry particles to wet ones, and from wet particles to dry ones as a result of collisions between particles. As soon as the liquid film forms, i.e. its thickness ( $h_0$ ) exceeds zero, imbibition by capillary effect begins to occur, as well as drying. Once particle pores are filled completely with liquid, there is no further imbibition.
- 4- Upon contacts between liquid and particles, " $h_0$ " begins to grow on the wet particles, while at the same time decreasing due to drying and imbibition. The initial liquid film thickness is calculated based on a balance of total liquid entering the bed and evaporation in the bed. The liquid film is assumed to grow until an agglomerate is formed. At this stage, it is assumed that the liquid film growth stops, and the excess liquid is designated as interstitial liquid that is not attached to the particle.

- 5- The volume of liquid in agglomerate form (liquid bridges) is then calculated and the movement of agglomerate is tracked in the CFD solver. Despite formation of agglomerates, a mono-disperse granular model is considered for modeling of the solid phase for simplicity.
- 6- Imbibition due to capillary forces continues until all particle pores are saturated with liquid. Based on the experimental observations, this process takes some time, until the particles are saturated with liquid, and then only drying is available as a means of decreasing the liquid film height. There is no further liquid intake into the pores after saturation.

### 5.3.1 Imbibition model

The goal in this section is to derive an equation to describe the relationship between “h” (liquid film height) and “y” (penetrating liquid depth), and then to derive an equation to calculate the amount of liquid imbibed into pores. The mass of the liquid film can be expressed as:

$$M_{\text{film}} = \rho_l V_{\text{film}} \quad \text{Eq.5.1}$$

Here  $M_{\text{film}}$  and  $V_{\text{film}}$ , are the mass and volume of liquid film calculated as:

$$V_{\text{film}} = \pi h \left[ (h + d)^2 + \frac{1}{3} h^2 \right] \quad \text{Eq.5.2}$$

where “h” is the height (thickness) of the deposited liquid film (see Fig. 5.1). Combining Eqs. 5.1 and 5.2, the change of liquid mass can be written as:

$$\frac{dM_{\text{film}}}{dt} = \rho_l \pi (d + 2h)^2 \frac{dh}{dt} \quad \text{Eq.5.3}$$

On the other hand, the change of liquid mass around the particle appears as a penetrating liquid inside the pores and can be expressed as:

$$\frac{dM_{\text{film}}}{dt} = -N_{\text{pore}} \frac{dM_1}{dt} \quad \text{Eq.5.4}$$

where  $N_{\text{pore}}$  is the number of pores inside the particle, calculated from:

$$N_{\text{pore}} = \varepsilon_p \left( \frac{A_{\text{wet}}}{A_{\text{pore}}} \right) \quad \text{Eq.5.5}$$

$$A_{\text{wet}} = \pi d_p^2 \quad \text{Eq.5.6}$$

$$A_{\text{pore}} = \pi r_{\text{pore}}^2 \quad \text{Eq.5.7}$$

where  $\varepsilon_p$  is the intraparticle porosity and  $A_{\text{wet}}$  corresponds to the wet surface area, which is the surface area wetted by droplet, and  $A_{\text{pore}}$  is the pore cross-sectional area. The mass of liquid in a cylindrical capillary at any time is given by:

$$M_1 = \rho_1 V_1 = \rho_1 \pi r^2 y \quad \text{Eq.5.8}$$

Hence

$$\frac{dM_1}{dt} = \rho_1 \pi r^2 \frac{dy}{dt} \quad \text{Eq.5.9}$$

where “r” is the pore radius, y is the vertical distance from the surface of the particle to which the liquid penetrates and  $V_1$  is the volume of liquid in the particle pore. Substituting equations 5.5 and 5.9 into equation 5.4 and combining with equation 5.3, we can derive the relation:

$$\frac{dh}{dy} = \varepsilon_p \frac{d_p^2}{(d_p + 2h)^2} \quad \text{Eq.5.10}$$

$$\int_{h_0}^h (d_p + 2h)^2 dh = \varepsilon_p d_p^2 \int_0^y dy \quad \text{Eq.5.11}$$

$$y = \frac{(h_0 - h) \left[ d_p^2 + 2d(h_0 - h) + \frac{4}{3}(h_0 - h)^2 \right]}{\varepsilon_p d^2} \quad \text{Eq.5.12}$$

where  $h_0$  is the initial liquid film height at the start of the penetration process.

At the next stage, an equation is required to relate the penetration length ( $y$ ) to liquid and to the pore properties. According to Washburn (1921), liquid penetration inside the pores can be described based on a force-balance:

$$F_{ca} + F_{hs} = F_{gr} + F_v \quad \text{Eq.5.13}$$

where  $F_{ca}$ ,  $F_{gr}$ ,  $F_{hs}$  and  $F_v$  are the capillary, gravity, hydrostatic and viscous forces, respectively, Eq. 5.13 is based on the assumption of open-pores at both ends and a uniform liquid film thickness around the particles. The forces are described by:

$$F_{ca} = 2\pi r \sigma_l \quad \text{Eq. 5.14}$$

$$F_{gr} = \pi \rho_l g r^2 y \quad \text{Eq. 5.15}$$

$$F_v = 8\pi \mu_l y \frac{dy}{dt} \quad \text{Eq. 5.16}$$

$$F_{hs} = \pi \rho_l g (h_0 - h) r^2 \quad \text{Eq. 5.17}$$

Here  $\mu_l$  is the liquid viscosity,  $\sigma_l$  the liquid surface tension and “ $r$ ” is the pore radius. For the case studied in this section, capillary and viscous forces act in opposite directions. The hydrostatic force would act in favor of imbibition and is on the same side as the capillary force. Gravity may accelerate or reduce imbibition, depending on the position of the deposited droplet. If the liquid is imbibed downwards through the top section of the particle, then gravity accelerates penetration. On the other hand, if imbibition is upwards starting at the bottom section, then the

gravity force reduces the penetration speed. Terrazas-Velarde et al. (2011a; 2011b) assumed that the effect of gravity, on average, can be neglected, due to continuing rotation of the particles which contributes to occurrence of both cases described. The same assumption is adopted in the present work. Eq. 5.13 assumes that the end of the pores at which imbibition begins is aligned with the gravity vector.

The pore diameter is on the scale of nanometers, whereas the liquid film thickness (h), at its maximum, is on the scale of microns. Therefore, the hydrostatic force given by Eq. 5.17 can be neglected compared to other forces described above. Eq. 5.15 then becomes:

$$F_{ca} = F_v \quad \text{Eq. 5.18}$$

After substitution of equations 5.14 and 5.16 into equation 5.18, liquid penetration due to capillary effects can be estimated by solving the differential equation:

$$y \frac{dy}{dt} = \frac{\sigma_l r_{\text{pore}}}{4\mu_l} \quad \text{Eq.5.19}$$

Considering the initial condition of  $y(t=0)=0$ , the solution is:

$$y = \sqrt{\frac{\sigma_l r_{\text{pore}}}{2\mu_l} \cdot t} \quad \text{Eq.5.20}$$

Finally, substituting Eq. 5.12 into Eq. 5.19 and solving for t, we obtain an equation for imbibition time:

$$t_{imb} = \frac{2\mu_l}{(\varepsilon_p \cdot d_p^2)^2} \times \frac{\left( (h_0 - h_{imb}) \cdot d_p^2 + 2 \cdot d_p \cdot (h_0 - h_{imb})^2 + \frac{4}{3} (h_0 - h_{imb})^3 \right)^2}{\sigma \cdot r_{\text{pore}}} \quad \text{Eq.5.21}$$

Equation 5.21 can be rearranged to provide a cubic equation which is then solved for the height decrease due to imbibition ( $h_0 - h_{imb}$ ):

$$\frac{4}{3} \cdot (h_0 - h_{imb})^3 + 2 \cdot d_p \cdot (h_0 - h_{imb})^2 + (h_0 - h_{imb}) \cdot d_p^2 + \alpha \cdot \varepsilon_p \cdot d_p^2 \cdot \left( \frac{\sigma_l r_{\text{pore}}}{2\mu_l} \right)^{1/2} \cdot t^{1/2} = 0$$

$$\text{Eq. 5.22}$$

By regarding “t” as the simulation time-step, the corresponding imbibition height at each time-step is calculated by solving Eq. 5.22. The outcome of the first set of simulations indicates that there is only one physically reasonable solution for  $(h_0 - h_{imb})$  in Eq.5.22.

### **5.3.2 Drying experiments and models**

Drying by mass transfer is due to the combined effects of convection and diffusion. The former is expected to be the dominant mechanism when there is a liquid film around particles, whereas the latter is expected to govern when the drying occurs in particle pores. In order to test this hypothesis, simple experiments were conducted to determine the drying rate from internal pores of stationary particles. Experiments were conducted in two phases:(1) ambient conditions ( $T=21\text{ }^{\circ}\text{C}$ ), and (2) heated conditions ( $T=60\text{ }^{\circ}\text{C}$ ). About 40 g of a mixture of FCC particle stirred and wetted with pure heptane was put in a Pyrex petri glass and kept under sealed condition for about 4 hours to ensure complete imbibition of liquid inside the particle pores. The wet mixture was then placed on a weighing scale (with 0.01 g accuracy) and a table fan was turned on to blow air over the wet sample on the scale (Fig. 5.3). The table fan speed was altered between settings of 1 and 3 corresponding to a range between 1000 and 1750 rpm. The change of weight due to vaporization is then plotted versus time to monitor the change of slope.

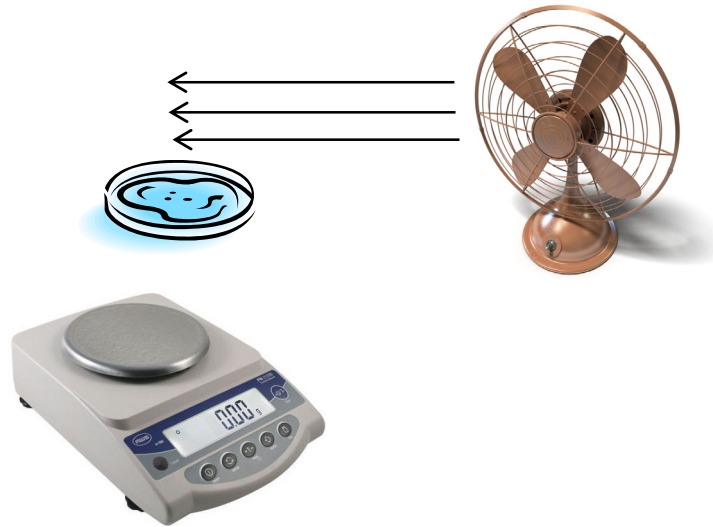


**Figure 5.3 Schematic of drying experiments.**

Fig. 5.4 plots mixture weight index (a non-dimensional value obtained by dividing the wet mixture weight by initial dry weight) vs. time for three different blower speeds at ambient conditions. The simulated and experimental conditions were identical in all three cases. The constant rate region occurs between 70 to 100 s of drying, due to vaporization of liquid film around particles and any liquid bridges between particles. Then there is a falling rate region where noticeable change in slope due to evaporation of liquid from inside the particle pores. Despite an increase in fan speed, the slope in falling rate region of drying does not show a significant change. The time required for complete drying was observed to be the same for all three fan speeds, implying that forced convection is not the dominant mechanism and that the evaporation occurs from inside particle pores due to diffusion effects.

In the second set of experiments, a mixture of particles and heptane was heated in an oven to 60°C. A heat gun was utilized to provide hot air at 60°C to blow over the mixture. The results shown in Fig. 5.5, depict a steeper slope of drying compared to the ambient condition tests. It was observed that convection dries the surface almost immediately, leaving evaporation

from pores for most of the time included in Fig. 5.5. The slope of the drying curve for heated conditions was about 10 times the slopes of the drying curve for ambient conditions, implying a strong effect of temperature on the diffusion coefficient. The temperature-dependence of diffusion coefficient is often expressed as:

$$D_T = D_0 \left( \frac{T}{T_0} \right)^n \quad \text{Eq. 5.23}$$

where  $D_T$  and  $D_0$  are diffusion coefficients at temperatures  $T$  and  $T_0$ . Exponent “ $n$ ” has been reported to be equal to 2 (Beyhaghi et al. 2014) or 1.75 (Fogler, 2004). This is in agreement with the experimental results presented in this section where the exponent was close to 2.

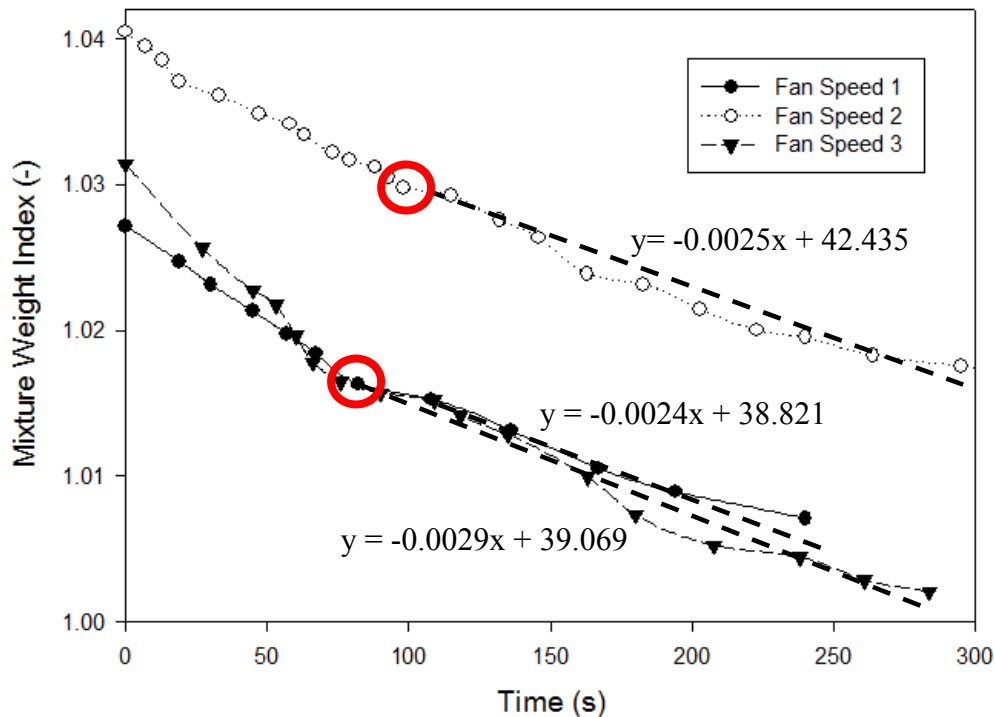


**Figure 5.4 Mixture weight index (non-dimanesional) vs. time (s) at ambient condition for three fan speeds (1000, 1400 and 1750 rpm). The circles show transition in drying from falling to constant rate.**

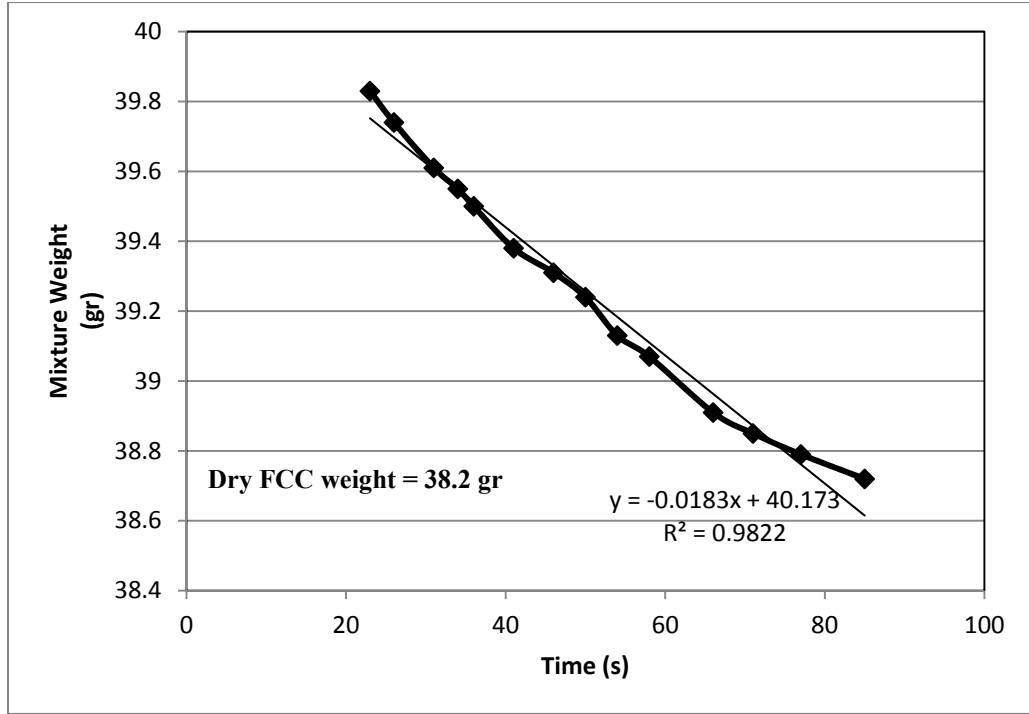


Figure 5.5 Mixture weight (g) vs. time (s) at T = 60 °C.

### 5.3.3 Drying model

#### 5.3.3.1 Convection drying

The transient change of liquid mass around the particle due to vaporization can be described (Ennis et al. 1991) as:

$$\frac{dM_{film}}{dt} = A_{film}\beta\rho_g(y^* - y_g) \quad \text{Eq.5.24}$$

where  $A_{film}$  is the surface area (including pore surface) of the liquid deposited on the particle surface,  $\beta$  is the mass transfer coefficient and  $y^*$  is the vapor molar fraction at saturation obtained from:

$$y^* = P_v^*/P \quad \text{Eq.5.25}$$

$P_v^*$  is the saturation vapor pressure and  $y_g$  is the vapor molar fraction in the bulk gas. Comparing the right-hand-side (RHS) and solution to Eqs 5.4 and 5.24, we find that the imbibition is one to

two orders of magnitude faster than the drying process. Hence it is assumed that liquid first penetrates into the pores after which the remaining liquid film undergoes drying.

Combining equations 5.24 with equation 5.3 yields:

$$(h_0)_{new} = h^* - h_{dry} = \beta \frac{\rho_g}{\rho_l} (y^* - y_g). t \quad \text{Eq.5.26}$$

where  $h^*$  is the height of liquid film remaining after penetration ( $h_0 - h_{penetration}$ ), and “ $h_{0new}$ ” is the new liquid film height at which the effect of liquid penetration and drying are both considered.  $\beta$  is the mass transfer coefficient, which can be estimated by the Frossling correlation (Frössling, 1938):

$$\beta = \frac{(2+0.6Re_l^{0.5}Sc_g^{0.33})D_v}{d_p} \quad \text{Eq.5.27}$$

where  $Sc_g = \frac{\mu_l}{\rho_l D_v}$  is the Schmidt number and  $D_v$  is the diffusivity of liquid in the vapor phase.

### 5.3.3.2 Diffusion drying

Based on the experimental observations described in section 5.3.2, The drying rate for liquid evaporation from inside particle pores can be determined (Kelly-Zion et al., 2011) assuming a diffusion-dominant mechanism:

$$E = 4r_{pore}D_v\rho_v \frac{P_A}{P_V} \ln \left( \frac{1}{1-(P_V/P_A)} \right) \quad \text{Eq.5.28}$$

where  $E$  is the mass evaporation rate,  $r_{pore}$  is the pore radius,  $D_v$  is the mass diffusivity of heptane in air,  $\rho_v$  is the density of heptane in vapor phase,  $P_A$  is the atmospheric pressure and  $P_V$  is the vapor pressure of heptane. The mass diffusivity of heptane in air has been reported to be 7.43 mm<sup>2</sup>/s (Kelly-Zion et al., 2011) at 25°C. Eqs. 5.28 and 5.23 can then be utilized to estimate the evaporation rate at different temperatures in the experiments.

### 5.3.4 Maximum liquid film growth

Liquid film growth is a limiting factor in imbibition. One possible scenario is that the liquid film continues to grow due to more impacts with droplets, reaching a limit where the film starts to coalesce with another wet particle, forming an agglomerate. This limit can be referred to as the “minimum film thickness required for agglomeration”. The agglomeration mechanism can be dominated by viscous or capillary forces. In order to check the predominant mechanism, the capillary number ( $Ca$ = ratio of viscous forces to capillary force) is calculated over the range of experimental conditions in this work (Donahue et al., 2010). The approximate values used for calculations are listed in Table 5.1, with

$$Ca = 3\mu \left(\frac{d_p}{4}\right) v / \sigma h_0 = 0.3 \sim 16 \quad \text{Eq.5.29}$$

Here “ $h_0$ ” is the separation distance between two colliding particles and “ $v$ ” is the relative particle velocity, approximated based on typical granular temperatures. Based on the results, both capillary and viscous forces contribute to agglomerate formation over the range of experimental conditions in this work. However, taking into account the liquid jet region where there is a high collision velocity, leading to higher relative particle velocity, the capillary number shifts towards higher values, suppressing the effect of capillary forces. This is in agreement with Darabi et al. (2009) with respect to agglomerate formation in a typical fluid coker.

In a viscous-dominant approach, a critical Stokes number is used to determine whether or not an agglomerate forms. According to Ennis et al. (1991), the Stokes number for conditions where particles contact each other under wet conditions is:

$$St_{coalesce} = \frac{2M_{agg}u_c}{3\pi\mu d_{agg}^2} \quad \text{Eq.5.30}$$

$$\text{with } M_{agg} = V_{cap}\rho_l + V_p\rho_p = \left[ \pi h(h + d_p)^2 + \frac{\pi}{3}h^3 \right] \rho_l + \frac{\pi}{6}d_p^3\rho_p$$

$$d_{agg} = d_p + 2h_0$$

where “ $h_0$ ” is the height of liquid film around each particle and “ $u_c$ ” is the particle collision velocity that could be related to granular temperature. Coalescence occurs when the calculated Stokes number is less than or equal to the critical Stokes number defined (Davis et al. 2002) as:

$$St_c^* = \ln\left(\frac{h_0}{h_r}\right) \quad \text{Eq. 5.31}$$

where “ $h_0$ ”, the thickness of liquid deposited on particles, is taken as the initial separation distance between surfaces of colliding particles, and “ $h_r$ ” is the separation distance at the time of collision. There are different length-scales for specifying the viscous-dominant critical separation distance: (i) glass-transition, (ii) lubrication and (iii) roughness length scales (Donahue et al., 2010). The glass-transition criterion is a way to treat a pressure-dependent viscosity where at some high-pressure point, the liquid has infinite viscosity, behaving as a solid (Donahue et al., 2010). The lubrication length scale corresponds to when the particles have sufficient inertia during the collisions to penetrate the liquid layer and decrease it until their separation distance reaches an elastohydrodynamic length scale defined (Davis et al., 2002; Donahue et al., 2010) as:

$$h_r = \left( 3\pi\theta\mu\alpha^{3/2}v_0/\sqrt{2} \right)^{2/5} \quad \text{Eq. 5.32}$$

where  $\theta = \frac{2(1-\nu^2)}{\pi E^2}$ ,  $E$  is the Young modulus of elasticity,  $\nu$  is Poisson’s ratio, “ $a$ ” is the radius of the colliding particles, and  $v_0$  is the initial relative velocity of a given particle-pair collision. The roughness length scale is used when the colliding surfaces have sufficiently large asperities. In that case, the separation distance between two objects equals the effective height of the

asperities. In this work, only the lubrication and roughness length scales are considered, with the largest value used as “ $h_r$ ” in Eq. 5.31.

Adding the effect of capillary forces would increase the critical separation distance at which the agglomerates form. Darabi et al. (2009) proposed an approach which considered the effect of both capillary and viscous forces by calculating the maximum possible energy dissipation and total kinetic energy of the colliding wet particles:

$$L_{t,max} = 2(W_{vis} + W_{cap} + L_c) \quad \text{Eq. 5.33}$$

$$E_k = mu^2 \quad \text{Eq. 5.34}$$

$L_{t,max}$  is the maximum possible energy dissipation, while  $E_k$ ,  $m$  and  $u$  are the kinetic energy, mass and velocity of the colliding particle,  $W_{vis}$  and  $W_{cap}$  are the maximum possible viscous and capillary works, and  $L_c$  is the contact loss. All of these terms were defined by Darabi et al. (2009) at both the approach and rebound stages. If  $E_k \leq L_{t,max}$ , then an agglomerate forms. Otherwise, the colliding wet particles bounce apart, and any existing agglomerate ruptures.

In this work, the maximum liquid film growth is governed by the agglomerate formation criterion described above by Eqs 5.29 and 5.30. Due to the relative complexity of the Darabi et al. (2009) approach, the capillary effect is neglected, and the critical Stokes number is used to characterize agglomerate formation:

$St_{coalesce} \leq St_c^* \rightarrow$  *new agglomerate forms*  $\rightarrow$  “ $h_0$ ” does not increase further

$St_{coalesce} > St_c^* \rightarrow$  *agglomerate does not form*  $\rightarrow$  “ $h_0$ ” can increase further

**Table 5.1 Properties used when calculating capillary number**

<u>Property</u>	<u>Value</u>
$d_p$	100 – 150 microns
$v$	0.3 ~ 1 m/s
$h_0$	0.1 - 10 microns
$\mu_l$ (@ 60°C)	0.0003 – 0.001 Pa.s
$\sigma$	0.02 N/m

#### 5.4 Structure of the CFD model

The modeling studies in this work are based on the presence of three phases: gas, solid and liquid, each with its own physical properties. Due to the neglect of temperature gradients and heat transfer effect, the only interactions between phases considered here are mass and momentum transfer. Momentum transfer between phases is taken into account based on relevant drag models, whereas mass transfer between the phases is based on the mechanisms outlined in section 5.3.

In order to differentiate dry particles from those contacted by liquid (wet particles), two species are introduced: (a) *Dry particles*, i.e. particles with no liquid, and (b) *wet particles* with solid cores (dry particles) coated by a thin liquid film on their outer surfaces. Both species are grouped into a mixture component in FLUENT under the name “particles”. Because these two species do not represent a separate phase, but are considered as descendants of the solid phase, their physical properties such as pressure and viscosity are assumed to be identical to the solid phase and are calculated from the kinetic theory of granular flow. The densities and diameters of dry and wet species are also assumed to be identical for simplicity.

### 5.4.1 Mass transfer mechanisms

Based on the assumptions described above, the following mass transfer mechanisms between phases/species are considered:

- Mass transfer between liquid droplets and particle mixture ( $q_{lp}$ )
- Mass transfer between wet particles and dry particles within the particle mixture ( $q_{dwet}$ )
- Mass transfer between wet particles and the bulk gas due to vaporization ( $q_{pg}$ )

Since the liquid layer thickness is assumed to be identical for all wet particles, liquid transfer among wet particles is assumed to be negligible.

Next consider collisions between liquid droplets and particles. Mass transfer due to particle-droplet collisions is proportional to the number of collisions. These source terms are described by:

$$q_{dwet} = m_{pwet} f_{p,dwet} \quad \text{Eq. 5.35}$$

$$q_{lp} = m_l f_{lp,d} \quad \text{Eq. 5.36}$$

The subscripts l, p and d stand for liquid, particle and dry.  $m_{pwet} = \rho_p \pi d_{pwet}^3 / 6$  is the mass of a single wet particle,  $m_l = \rho_l \pi d_l^3 / 6$  is the mass of a single liquid droplet,  $f_{lp,d}$  is the number of collisions between droplets and dry particles per unit volume and time, and  $f_{p,dwet}$  is the number of collisions between wet and dry particles per unit volume at time. We approximate  $f_{p,d}$  (Iyer et al. 2002; Nayak et al. 2005) by:

$$f_{lp,d} = \frac{\pi}{4} \left( \frac{6\varepsilon_l}{\pi d_l^3} \right) \left( \frac{6\varepsilon_d}{\pi d_{pd}^3} \right) (d_{pd} + d_l)^2 |\vec{V}_l - \vec{V}_p| \quad \text{Eq. 5.37}$$

where  $d_{pd}$  is the diameter of dry particles,  $V_l$  is the velocity vector for liquid and  $V_p$  is the velocity vector for particles. Using the same approach and considering two colliding particles to reach each other due to granular temperature,  $\theta$ , we arrive at:

$$f_{p,dwet} = \frac{\pi}{4} \left( \frac{6\varepsilon_d}{\pi d_{pd}^3} \right) \left( \frac{6\varepsilon_{wet}}{\pi d_{pwet}^3} \right) (d_{pwet} + d_{pd})^2 |2\sqrt{3\theta}| \quad \text{Eq. 5.38}$$

Mass transfer due to vaporization, i.e. evaporation of liquid from particle surfaces and agglomerates, is estimated based on the approach described in section 5.3.3.

## 5.4.2 Modeling species/phase transport

FLUENT solves the conservation equation for species by predicting the mass fraction of each species through the solution of a convection-diffusion equation:

$$\frac{\partial}{\partial t} (\alpha_i \rho_i X_i) + \nabla \cdot (\alpha_i \rho_i X_i \vec{V}_i) = \nabla \cdot (D_m \alpha_i \rho_i \nabla(X_i)) + q_{ij} \quad \text{Eq.5.39}$$

where  $\alpha_i$  is the volume fraction of species (i),  $X_i$  is the mass fraction of species (i),  $D_m$  is the diffusion coefficient of species in the mixture and  $q_{ij}$  is a source term, described in section 5.4.1, related to mass transfer between species/phases.

Based on the type and direction of mass transfer (between species or between one species and a phase), the mass source term contribution is reflected in the mass and momentum equations and can be categorized as follows:

- Mass transfer from phase (i) to species (j):  $+q_{ij}$  to species transport equation,  $-q_{ij}$  to phase mass transport equation,  $-q_{ij} \times \vec{V}_i$  to phase (i) momentum equation and  $+q_{ij} \times \vec{V}_i$  to the momentum equation of the phase which contains species (j), where  $\vec{V}_i$  is the velocity vector
- Mass transfer from species (i) to species (j):  $+q_{ij}$  to species (j) transport equation,  $-q_{ij}$  to species (i) transport equation,  $-q_{ij} \times \vec{V}_i$  to momentum equation of the phase which contains species (i) and  $+q_{ij} \times \vec{V}_i$  to momentum equation of the phase which contains species (j).

### 5.4.3 Mechanism of liquid film thickness growth in CFD modeling

After estimating the amount of liquid transferred between liquid phase and solid species, it is crucial to calculate the initial liquid film thickness at the beginning of iteration in each computational cell. The volume fraction of wet particles is calculated by the CFD solver in every iteration by solving the specie transport equation. The number of wet particles in a computational cell is then obtained from:

$$n_{wet} = \frac{6\varepsilon_{wet}}{\pi.d_p^3} \times V_{cell} \quad \text{Eq. 5.40}$$

where  $\varepsilon_w$  is the volume fraction of wet particles,  $d_p$  is the particle diameter and  $V_{cell}$  is the volume of each computational cell. According to the assumptions, liquid is distributed equally over all particles. In order to calculate the film thickness when there is continuous liquid injection into the bed, overall liquid conservation is checked after each iteration, including total injected liquid, evaporation and liquid located in pores:

$$V_{film,cell} = \left[ \left( \frac{\varepsilon_{wet} V_{cell}}{V_{wet}} \right) (V_{inj} - V_{pore} - V_{evap}) \right] / n_{wet} \quad \text{Eq. 5.41}$$

where  $V_{film,cell}$  is the liquid film volume around wet particles in each computational cell,  $V_{wet}$  is the total volume of all wet particles in the bed,  $V_{inj}$  and  $V_{evap}$  are the liquid injected volume, available in droplet form, and evaporated liquid volume, both calculated from the beginning of liquid injection,  $V_{pore}$  is the volume of liquid in particle pores, and  $n_{wet}$  is the number of wet particles in the computational cell. This liquid balance check is used to calculate the thickness of the liquid film. This is then tested against the maximum liquid film growth described in section 5.3.4. If the calculated value exceeds the maximum value allowed by the critical Stokes criteria,

then the excess liquid is designated as agglomerate. In this case, it is available only for drying and not for imbibition.

#### **5.4.4 CFD solution procedure**

The general solution process for the pressure-based coupled solver in FLUENT is depicted in Fig. 5.6. In the initial stage of the iteration loop, FLUENT solves the governing equations of continuity and momentum in a coupled fashion, i.e. simultaneously as a set, or vector, of equations. Species transport equations, described in section 5.4.3, are then solved sequentially. After the conservation and species equations, user-defined properties, including liquid film thickness in each computational cell, are updated. A check for either convergence or additional iterations is performed, and the loop either continues or stops.

Based on the solution algorithm shown in Fig. 5.6 and the CFD modeling considerations discussed in section 5.4.1, the steps in the CFD solution algorithm of liquid injection with imbibition and drying mechanisms present in a computational cell in the vicinity of liquid injection are as follows:

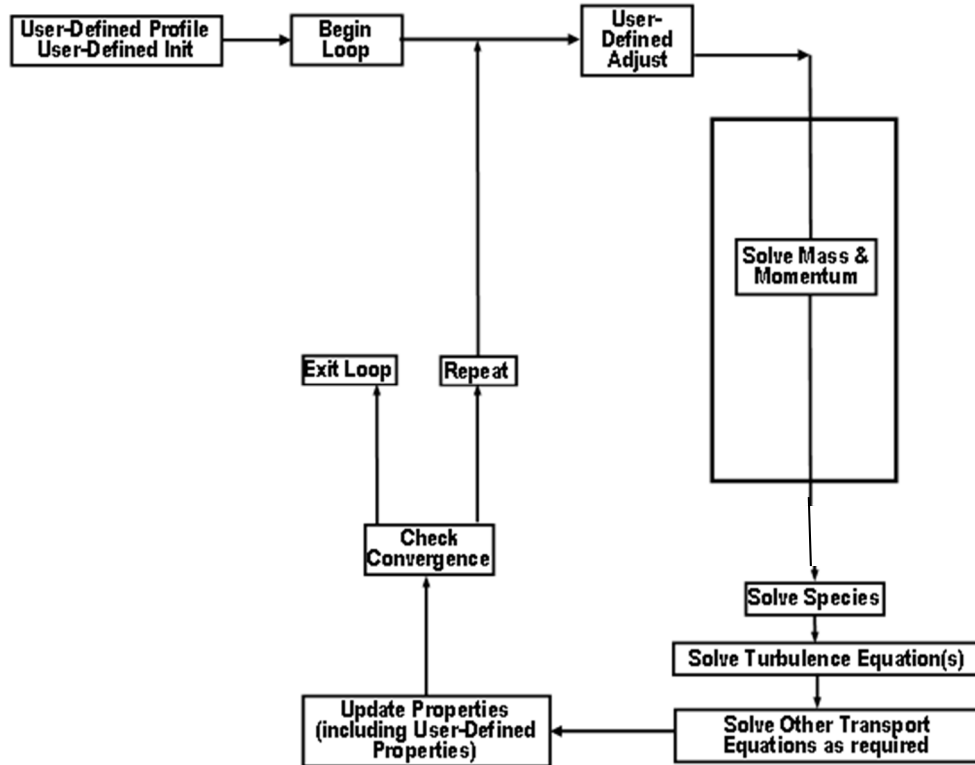


Figure 5.6 Solution Procedure for Pressure-Based Coupled Solver.

- 1- Prior to liquid injection, the particles are assumed to be dry, and there is no imbibition nor drying. The volume fraction of liquid phase ( $\epsilon_l$ ) then gradually increases due to liquid injection. As shown in Fig. 5.6, the species transport equation is solved after the conservation equations are solved. Therefore, the volume fraction of wet particles ( $\epsilon_w$ ) is still zero at this stage.
- 2- The liquid droplets reach and collide with the first group of particles. The mass transfer source terms described in sections 5.4.1 and 5.4.2 are calculated, and the conservation and species equations are updated. Now the volume fraction of wet particle species ( $\epsilon_w$ ) gradually increases from zero. The initial film thickness is calculated based on the

equations in section 5.4.3. As soon as the liquid film thickness exceeds zero, imbibition by the capillary effect occurs, as well as drying, each with its own time-scale.

- 3- The updated liquid film thickness influences the mass transfer source terms, consequently affecting the volume fraction of liquid and wet particles. In the next series of time-steps, the liquid phase volume fraction gradually starts to decrease due to mass transfer between liquid and particles/gas. This converts more dry particles to wet particles, resulting in an increase in wet particle volume fraction. Part of the liquid is vaporized, adding to the gas phase volume fraction. Collisions between dry and wet particles also contribute to the growth of wet particles and distribute them rapidly throughout the entire bed. This mechanism of liquid distribution then continues in subsequent time-steps.

Table 5.2 summarizes the physical properties of the three phases involved in this study.

**Table 5.2 Summary of phase properties for tests at atmospheric pressure and 60 °C**

<b><u>Property</u></b>	<b><u>Gas: Air</u></b>	<b><u>Liquid: Pure Heptane</u></b>	<b><u>Particles: FCC</u></b>
Density, kg/m <sup>3</sup>	1.05	684	1650
Viscosity, Pa.s	0.000019	0.0004	-
Surface tension, N/m	-	0.02	-
Diameter, μm	-	160	150
Internal porosity, -	-	-	0.75
Pore radius, nm <sup>5</sup>	-	-	4

---

<sup>5</sup>Altering the values of pore radius and internal porosity in following studies was found to only affect the time required for all particles to be saturated with liquid that is imbibed into the pores.

## 5.5 Simulation setup

The experimental apparatus at BCRI is simulated in FLUENT as shown in Fig. 5.1. An initial mesh size, refined in the vicinity of the liquid injection region, is selected to perform preliminary simulations, Mesh studies are included as indicated below. Air enters the system from two inclined distributors at the bottom of the column as shown by the bottom arrows in Fig. 5.1. It leaves the system at the top, while returning solids enter the system at the bottom of the column, as shown by the arrow on the right side of Fig. 5.1, just above the liquid injection boundary. The liquid injection nozzle is treated as a liquid mass-flow inlet boundary, as shown by the side entry left arrow in Fig. 5.1. The geometric details are listed in Table. 5.3. Pressure outlet and velocity inlet boundary conditions are set for gas exit and entry. For the inlet bottom, uniform gas velocity is specified at 0.37 m/s, based on total inclined area, with no particles entering the domain. For the side walls, a no-slip boundary condition for the gas phase and Johnson and Jackson (1987) partial-slip condition for the solid phase are applied. In order to preserve the mass of particles in the bed, the number of particles leaving the system is calculated for each time-step and is then added to the system via a side-entry solid return boundary with the mass flow inlet boundary condition.

**Table 5.3 Simulation setup values of operating and geometric quantities**

<u>Property</u>	<u>Value</u>
Superficial gas velocity	0.3-1 m/s
Column depth	N/A(2D geometry)
Column width	0.40 m
Column height	3.79 m
Static bed height (measured from point “A” shown in Fig. 5.6)	0.65 m

The two-dimensional double-precision (2DDP) computational domain was selected in FLUENT. Convergence criteria of  $10^{-3}$  for the continuity and momentum equations and  $10^{-4}$  for granular temperature were specified for absolute error monitoring. The laminar flow model was solved for the gas phase using the Phase-Coupled SIMPLE algorithm for pressure-velocity coupling. Second-order upwind discretization schemes were adopted for the convection terms, with the time step varied between  $10^{-4}$  and  $10^{-3}$  s to reach convergence.

### **5.5.1 Mesh study**

Mesh studies for simulations performed with the FB model in 2D require special care as the trend is not similar to cases where conventional drag models are utilized (see section 3.2.3.1). The effect of mesh size on liquid evaporation for the first 5 s of liquid injection is shown in Fig. 5.7. The ordinate is the concentration of heptane in vapor phase at sample point 4 (SP4). It can be seen that refining the mesh from the coarsest size (500 Cells) to 1215 Cells results in a

reduction of the amount of vaporized liquid. However, refining the mesh further results in a significant increase in the predicted amount of vaporized liquid. The reason was the prediction of denser region inside the bed when refining the mesh, which resulted in more particles in computational cells, contributing to a greater volume of liquid formed around the particles, hence to a higher vaporization rate. Referring to the similar behavior when using the FB model in hydrodynamic studies shown in section 3.2.3.1, it is concluded that further refinement of the mesh ( $> 1215$  Cells) could lead to over-prediction of liquid vaporization. Therefore, mesh sizes below 1215 Cells would be an appropriate choice for both hydrodynamics and liquid injection studies. In the present work, we chose 800 Cells as the basis for simulations.

### **5.5.2 Time-step study**

The effect of time-step on simulation results is shown in Fig. 5.8 for liquid evaporation at SP4. Changing the time-step from 0.0001 s to 0.0006 s drastically increased the concentration of heptane in vapor phase. There is also an irregular change of slope in the drying curve when the time-step was increased to 0.0006 s. This can be due to large size of the time-step which cannot correctly capture the dynamics of the system and results in unexpected irregularities. The deviations between the smallest time-step (0.0001 s) and 0.0004 s is acceptable for the purpose of this study. Hence, 0.0004 s was selected as the simulation time-step for the remaining simulations in this chapter.

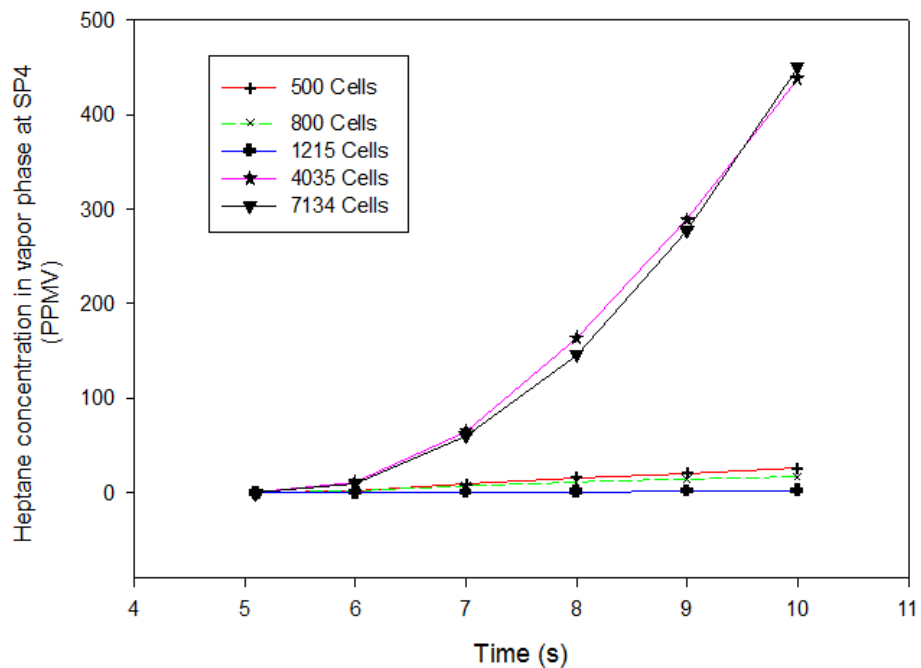


Figure 5.7 Effect of mesh size on heptane concentration in vapor phase predicted by CFD model.

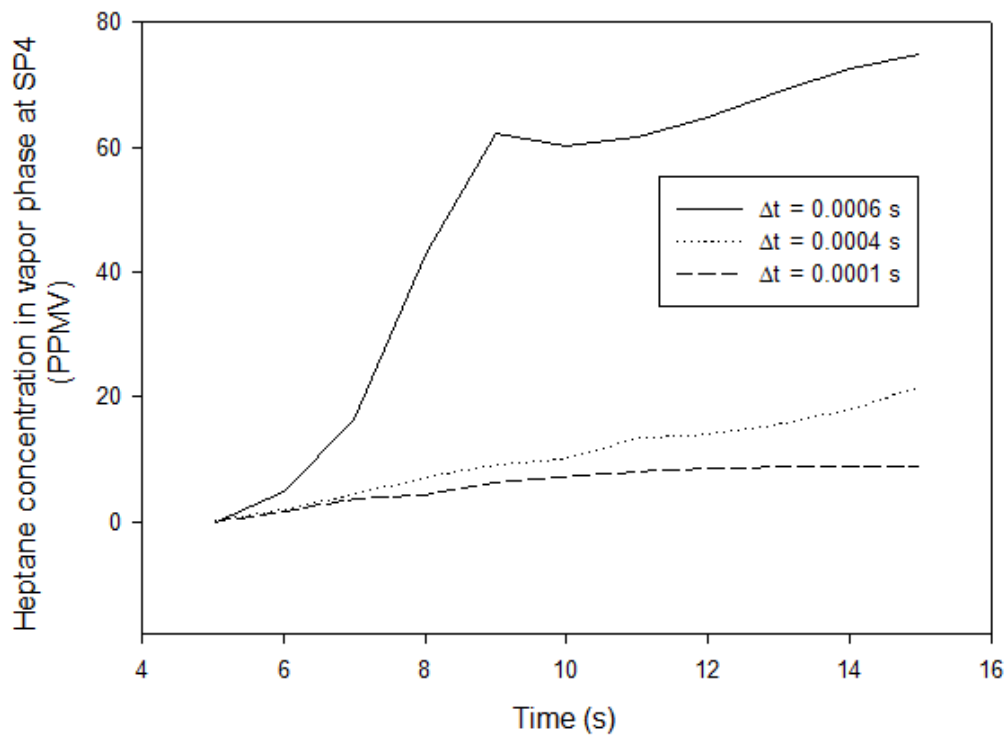


Figure 5.8 Effect of time-step on heptane concentration in vapor phase predicted by CFD model.

## 5.6 Results and discussion

### 5.6.1 A) Effect of imbibition and drying (before pore saturation)

The first simulations investigated the effect of imbibition and drying at the beginning of liquid injection when the particle pores contain no liquid. The case studied here (FCC-1) is based on experimental data from the Syncrude/BCRI cold model for pure heptane injection into a fluidized bed consisting of FCC at high Air-to-Liquid (ALR) ratio. The physical properties of phases are listed in Table 5.4. The bed and injected liquid were kept at the same temperature. The experimental mean particle (FCC) diameter was set at 150 microns. The FB drag model (described in Chapters 2 and 3) was used for gas-particle drag equation. The time-step was set at 0.0004 s. The injected liquid droplet diameter is set at 160 microns. All temperature-dependent properties are extracted for a temperature of 60°C at atmospheric pressure which corresponds to the operating conditions of the experimental setup for the BCRI experiments of Case FCC-1.

The development of the wet particle volume fraction is depicted in Fig. 5.9. Liquid injection starts after 5 s of dry fluidization. It is shown that, using the current mass transfer model, the liquid is distributed quite rapidly. The wetting process is predicted to start in the vicinity of the liquid jet and continues to the upper section of the bed due to drag effects of the gas and solid particles. It then extends to the bottom of the bed due to particle circulation until the entire bed is wetted by liquid.

**Table 5.4 Physical properties for Case FCC-1 at 60°C**

<b><u>Property</u></b>	<b><u>Value</u></b>
Superficial gas velocity	0.37 m/s
Mean particle diameter	130-150 $\mu\text{m}$
Liquid droplet diameter	160 $\mu\text{m}$
Particle density	1650 $\text{kg/m}^3$
Liquid Type	Pure Heptane
Liquid density	642 $\text{kg/m}^3$
Liquid viscosity	0.00026 Pa.s
Liquid saturation pressure	35.2 kPa
Liquid surface tension	0.02 N/m
Liquid Injection rate	0.093 g/s
Atomizing air injection rate	0.000167 g/s

Fig. 5.10 shows the imbibition length ( $y$ ), which is the length inside the pores penetrated by liquid. It is shown that liquid penetration into the pores starts at the end of the liquid jet and then rapidly continues over other sections of the bed. After 5 s of injection, a homogenous imbibition pattern is observed, with the penetration gradually increasing through all particles. After 15 s of injection, the penetration length increases to about 10  $\mu\text{m}$  as shown in Fig. 5.10. The liquid film on particles disappears at the end of each time-step due to evaporation and imbibition effects. It is expected that the simulations need to progress more than 100 s until pore saturation is reached and enough liquid exists in the system to form a film around all particles.

Fig. 5.11 shows the total liquid evaporation which includes evaporated liquid from particle surfaces, droplets and agglomerates (if any). The units for measuring the evaporation in this work is the concentration of evaporated liquid (ppmv) in the vapor phase that is measured at sampling points (SP4 and SP5 in Fig. 5.6). It is shown that at early stages, a maximum heptane concentration of 30 ppmv in the vapor phase occurs in the liquid jet area, but rapidly reduces to less than 1 ppmv.

This can be due to liquid penetration inside the pores which conserves the liquid and prevents further evaporation. After 15 s of liquid injection, only droplet evaporation continues in the bed, and evaporated liquid continues to move up the column, leaving the system through the outlet boundary.

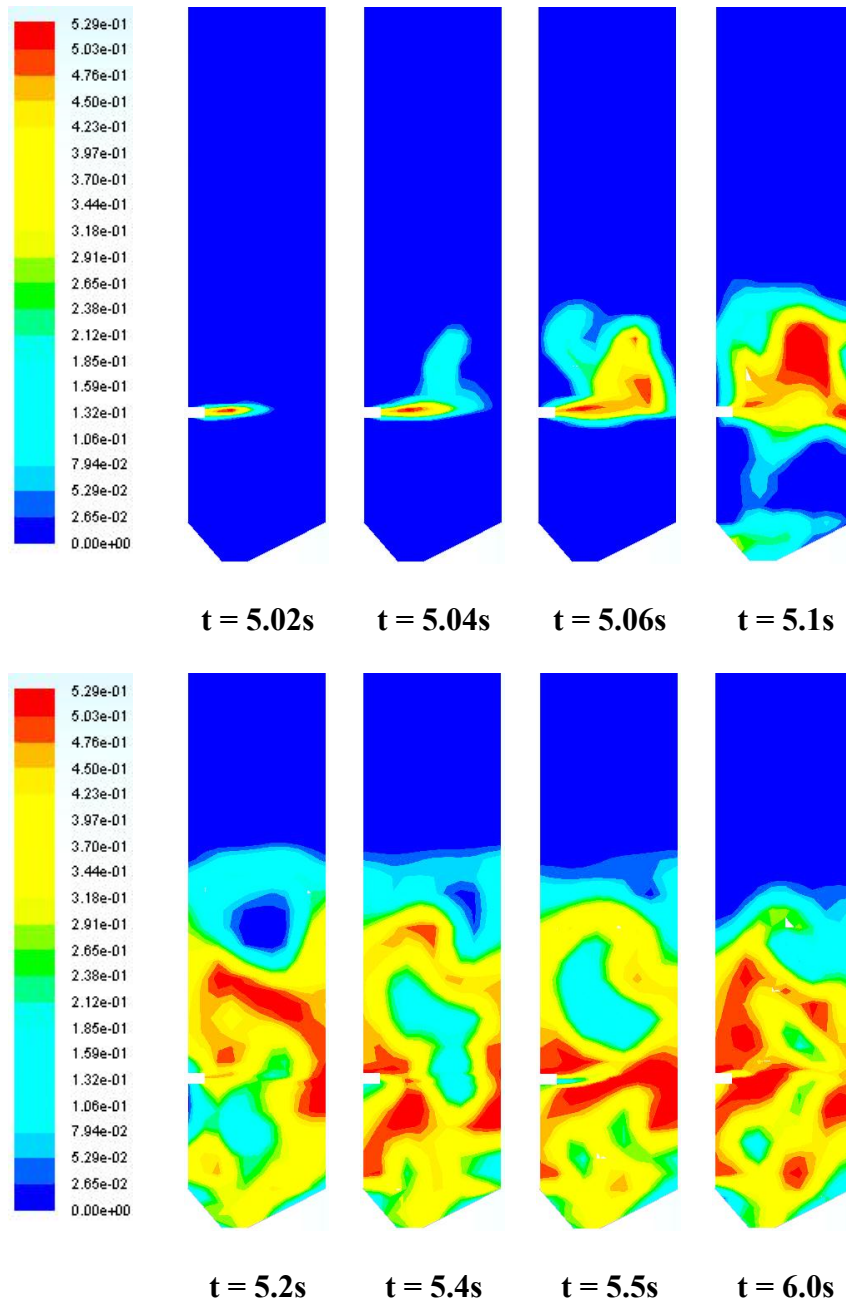


Figure 5.9 Development of wet particles volume fraction over first second after initiation of liquid jet.

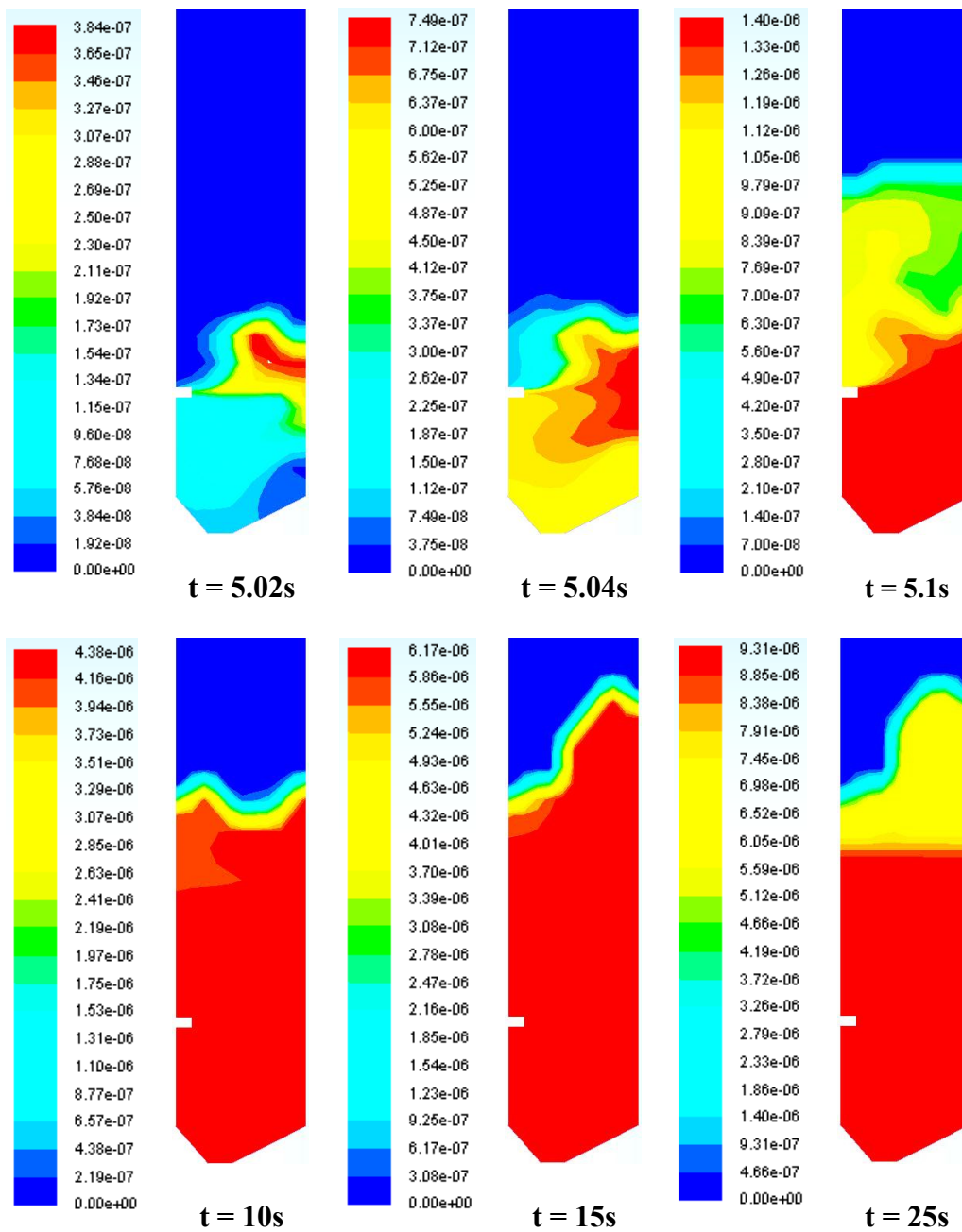


Figure 5.10 Development contours of imbibed liquid height (m) inside pores. Scale is in m.

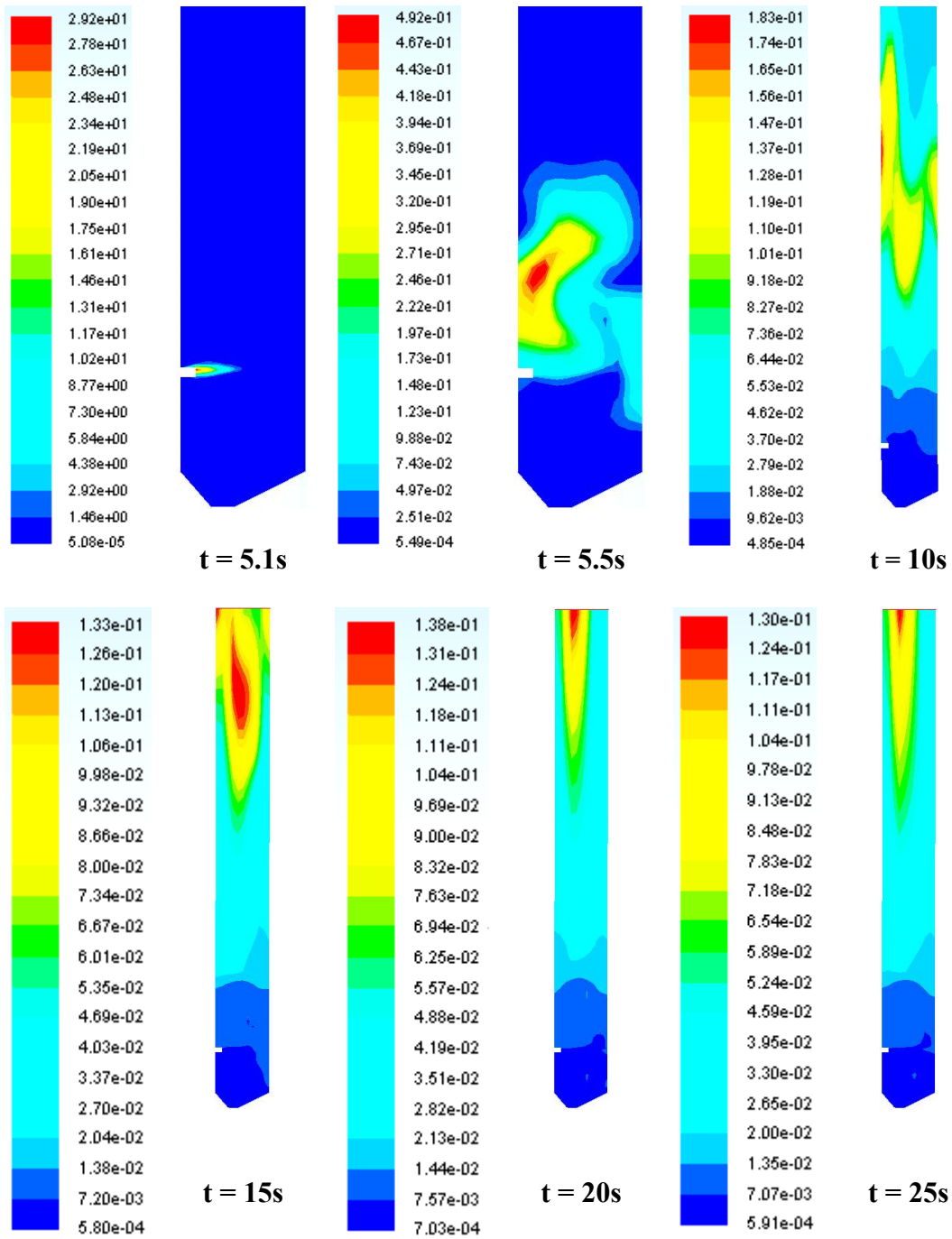
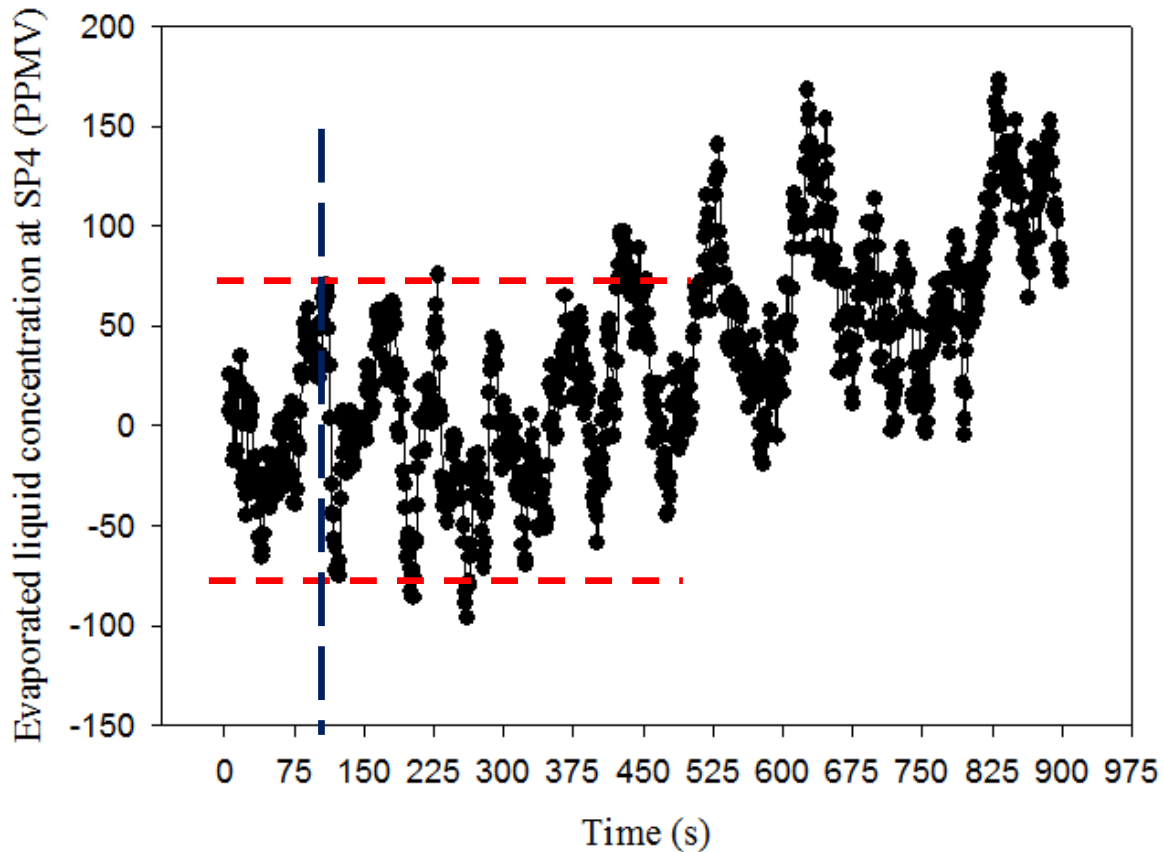


Figure 5.11 Concentration of heptane (ppmv) in vapor phase mapping.



**Figure 5.12** Experimental data (moving averaged over 5 s) for evaporated liquid concentration in case FCC-1. Vertical and horizontal dashed lines indicate initiation of liquid injection and error margins, respectively for location of SP4, per Fig. 5.1.

The experimental data indicate no significant evaporation for several minutes after initiation of liquid injection. This is apparent in Fig. 5.12 where the horizontal dashed lines show the oscillations before the initiation of injection (denoted by the vertical dashed line) and the extent of measurement errors by the analyzers SP4. It is seen that noticeable evaporation at SP4 was detected about 300 s after the initiation of liquid injection. Delay in appreciable evaporation can be due to the effect of particle pore and liquid imbibition, which delays evaporation from the liquid surfaces. The simulation results for mean liquid imbibition height in the bed vs. time is shown in Fig. 5.13. Extrapolating the trend depicted in Fig. 5.13, it appears that the imbibed

liquid will reach the maximum limit of 75 microns (after which the pores are completely saturated with liquid) about 200 s after initiation of liquid injection. This is consistent with experimental results shown in Fig. 5.12 which indicates the dominant effect of liquid imbibition in the early stages of liquid injection.

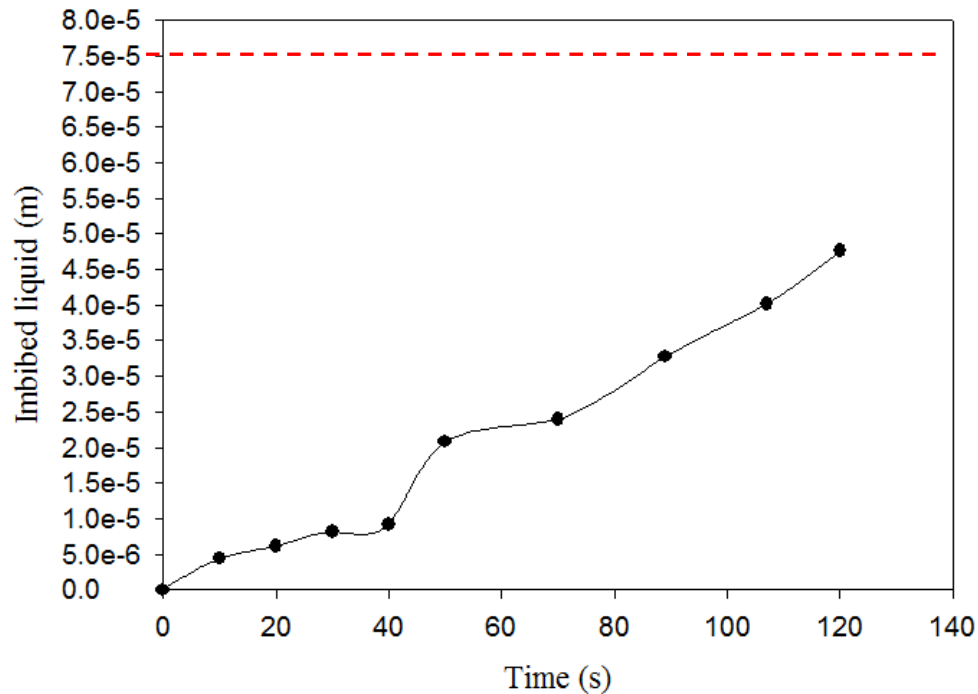


**Figure 5.13 Average liquid imbibition height (m) vs. time (s) after initiation of liquid injection. The dashed line shows the maximum imbibition capacity.**

### **5.6.2 B) Effect of imbibition and drying (after pore saturation-injection continues)**

Particle pore saturation refers to the state where all particle pores are filled completely with liquid. Imbibition of liquid into pores is the dominant mechanism before the pores become saturated with liquid, as discussed in the previous section. Drying during this period is minimal. Due to the long simulation time required to reach pore saturation, a separate set of simulations was performed starting from the saturation point. The evaporation is then considered to take

place due to convection from the liquid layer around particles and is calculated from equations in section 5.5.1, with any further liquid imbibition into particle pores neglected.

With 300 s after initiation (at time 0) of liquid injection as the basis of comparison in this section, Fig. 5.14 shows the experimental measurements of liquid evaporation at locations SP4 and SP5 (see Fig. 5.1) with CFD results. The experimental results and CFD predictions were averaged every 5 s.

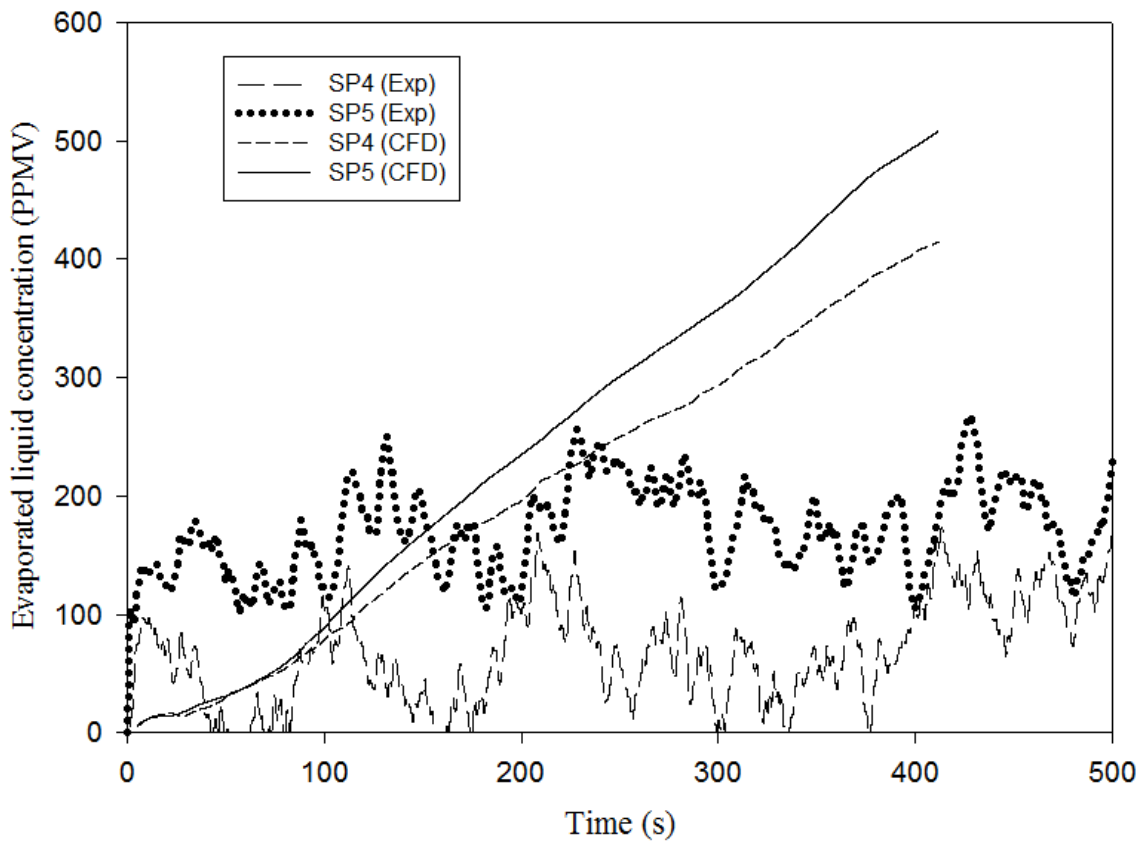


**Figure 5.14 Time-average experimental and CFD results for liquid evaporation at sample points SP4 and SP5, per Fig. 5.1.**

It is seen in Fig. 5.14 that the CFD results tend to under-predict evaporation at the beginning, then rising after 100 s to the point where there is fair agreement with experiments,

and then continuing to increase and deviate from experimental results. Note that the evaporation trend predicted by CFD showing higher evaporation for SP5 than for SP4 is in agreement with experimental data. SP5 is farther from the liquid jet. The greater heptane concentration in vapor phase at SP5 may be due to the jet propelling the liquid into the denser region where it accumulates and forms liquid films around particles, ultimately increasing vaporization in that region. Despite the fair qualitative agreement in some relatively brief periods of time during which vaporization occurs, the CFD code clearly overpredicts vaporization after 200 s since initiation of liquid injection.

The experimental results for evaporated liquid at SP4 and SP5, up to 2000 s after initiation of liquid injection, are shown in Fig. 5.15. It appears that there may be changes in trend of evaporation implying a combination of convection-diffusion driven mechanism for drying. This effect is not seen in the CFD results shown in Fig. 5.14. A tentative reason can be the complex effect of particle porosity on liquid evaporation. In addition to liquid drying from the surface of the particles, evaporation from inside particle pores allows further liquid imbibition into the pores, decreasing the thickness of the liquid layer around the particles and suppressing the convection drying. This can result in lower slopes of drying compared to the convection-driven mechanism utilized in this study and may explain the over-prediction of liquid evaporation by the CFD model.

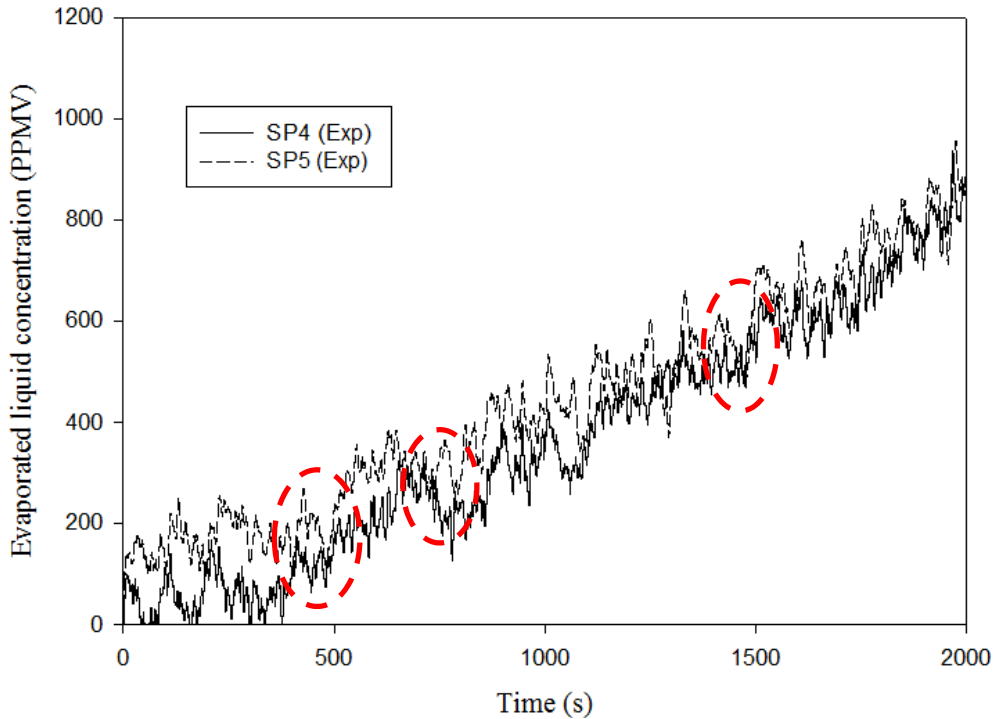


**Figure 5.15** Experimental results for evaporated liquid concentration (PPMV) at SP4 and SP5 vs. time. The circles indicate possible changes of slope, which could suggest multiple drying mechanisms.

### 5.6.3 C) Effect of imbibition and drying (after pore saturation-no injection)

The last stage of liquid injection experiments is the state where liquid injection is stopped and the bed is allowed to dry completely in a fluidized state. The experimental results for this stage are shown in Fig. 5.16. Three different drying sections were observed, denoted by numbers 1 to 3 in Fig. 5.16. The first section is the steep constant rate drying which can be attributed to the drying of any free liquid (droplets or agglomerates, if any). The second section can be related to evaporation of liquid film around the particles, and the third to the falling drying rate period featuring evaporation from pores.

Of special interest is the higher drying rate at SP4 vs. SP5, opposite to the behavior observed in both experiments and CFD simulations in section 5.6.2. This supports the role of

liquid jet explained in section 5.6.2 which contributed to the higher evaporation rates at SP5. In the absence of liquid injection, the fluidization hydrodynamics dictate the drying behavior at these two sample points.

In the diffusion-driven drying section 3 shown in the bottom portion of Fig. 5.16, two fitted drying curves are shown with different slopes at SP4 and SP5, again showing the effect of hydrodynamic properties (e.g. particle impact velocity) on the liquid drying behavior. The slope of the drying curves in section 3 of Fig. 5.16 is more than 10 times the slope obtained for the second set of simple drying experiments covered in section 5.3.2 which was conducted at the same temperature as in the BCRI experiments. This finding also implies that the drying kinetics in the last section of drying in Fig. 5.16 are not solely due to diffusion from inside the pores. It also shows the effect of fluidization velocity on drying kinetics, which is in-line with the conclusion from the experiments described in Chapter 4. Based on the observations in this section, a mechanism is proposed to capture the drying kinetics when there is no further liquid injection in the bed, as described below.

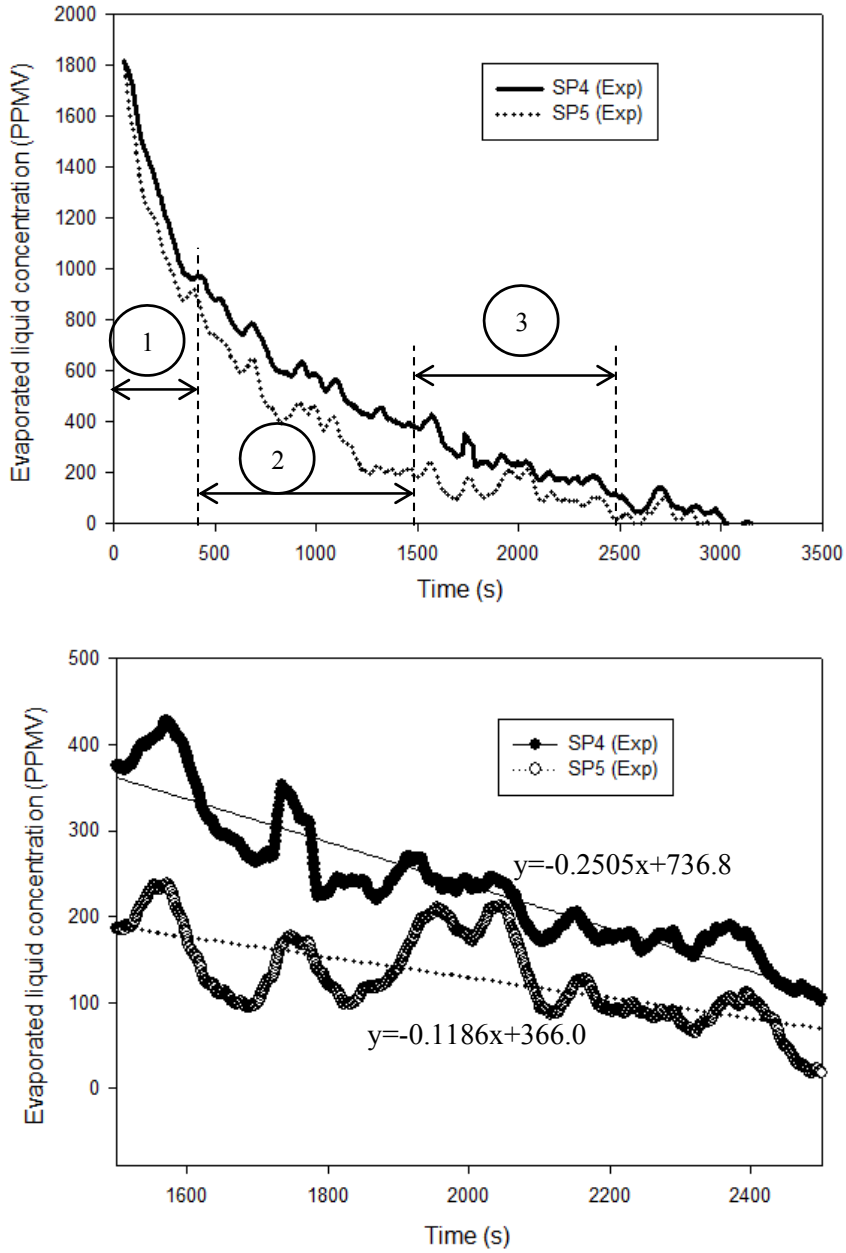


**Figure 5.16** Experimental results for evaporated liquid concentration (PPMV) at SP4 and SP5 vs. time (after liquid injection stops). Top sub-figure shows the whole drying curve, and bottom one magnifies drying section 3.

#### 5.6.4 Mechanism for drying from inside particle pores

Based on the experimentally observed drying behavior in Chapter 4 and CFD modeling discussed in this chapter, it was found that considering simple convection-driven or diffusion-driven mechanisms for liquid evaporation from either outer surface of particles or internal pores does not lead to accurate predictions, with the results not matching the trend of experimental data quantitatively. Therefore, a revised mechanism for liquid drying is proposed here for comparison with experimental data:

- 1- Injection starts at  $t=t_0$ . The particles are dry and there is neither imbibition nor drying.
- 2- Liquid droplets reach the first group of particles, resulting in collision between droplets and dry particles.
- 3- The liquid reaching particles is distributed equally over all particles in a control volume.
- 4- Upon contacts between liquid and particles, liquid film thickness begins to grow on the wet particles, while at the same time the growth is countered due to drying and imbibition. Liquid that is imbibed in the pores is not conserved, but contributes to the drying process. Regardless of whether the internal pores are saturated with liquid or the complete liquid film has penetrated into the pore, drying occurs from both the outer surface of the particles and from inside the particle pores due to convection and diffusion-driven drying mechanisms, respectively.
- 5- Changes in liquid height inside the particle pores and liquid thickness around the particle results in movement of liquid inside the pores which may bring a portion of the liquid to the outer surface of particles and, at the same time, allow more liquid to be imbibed into pores. A way to estimate this movement is described in the next paragraph.

It can be argued that liquid capillaries inside the pores move due to evaporation and collision of particles. It is also assumed that before evaporation occurs, the liquid height inside the pores reaches a steady level. Both convection and diffusion mechanisms are assumed to be responsible for drying at this stage. When there is no liquid formation around the particles, evaporation is limited by the rate of diffusion. Evaporation from the pores reduces the liquid column height inside the pores. This reduction, along with kinetic pressure exerted from collision of particles, results in movement of liquid inside the pores towards the particle surface. The imbibition of liquid from particle surfaces into the pores together with movement of liquid from inside the pores towards the outer surface would determine the liquid height inside the pores. Based on the capillary dynamics described by Washburn (1921), changes of liquid column height inside a capillary can be expressed by:

$$\frac{dy}{dt} = \frac{\sum P \cdot (r^2)}{8\mu_l y} \quad \text{Eq.5.25}$$

$$\sum P = P_h + P_s \quad \text{Eq.5.26}$$

$$P_h = hg\rho_l + \frac{1}{2}\rho_s v_s'^2 - y_0 g\rho_l \quad \text{Eq.5.27}$$

$$P_s = \frac{2\sigma_l}{r} \quad \text{Eq.5.28}$$

where  $y$  is the length of liquid column inside the pores,  $h$  is the thickness of liquid film around the particle,  $r$  is the pore radius and  $v_s'$  is the fluctuation velocity of particles, calculated using the granular temperature. Replacing  $v_s'$  by the granular temperature and solving Eq. 5.25 yields the change in liquid column height:

$$\Delta y = \sqrt{2 \left( \frac{\frac{3}{2}\rho_s \theta - y_0 g\rho_l + \frac{2\sigma_l}{r_{pore}} + hg\rho_l}{8\mu_l} r_{pore}^2 \right) \Delta t} - y_0 \quad \text{Eq.5.29}$$

If the calculated liquid height reaches the particle surface, the added liquid would change the liquid film thickness around the particle and the calculation procedure would then be repeated for the next time-step.

## 5.7 Conclusion

Liquid distribution and evaporation inside a fluidized bed was studied by performing CFD simulations utilizing existing imbibition and drying models and based on a series of assumptions. The modeling predictions were compared to experimental results from liquid injection experiments conducted at the British Columbia Research Institute (BCRI) in Burnaby with heptane as the liquid. Constraint of long run-time in experiments made it essential to perform simulations in stages. The process was divided into three different stages: A) Liquid injection starts into a dry bed with liquid film forming around the particles and then imbibed into particle pores. B) Liquid injection continues beyond the state where all particle pores are saturated with liquid and C) Liquid injection stops, and the bed is allowed to dry.

Simulations were performed for stages A and B. Comparison between CFD predictions and experimental results in stage A indicated a delay in start of liquid vaporization as observed in experiments, possibly due to the effect of particle porosity and liquid imbibition into particle pores. Comparing the CFD-predicted time-average heptane concentration in vapor phase with experimental results in stage B depicted qualitative consistency but quantitative deviations remain. Interpreting the trend of liquid concentration in vapor phase from CFD predictions and experimental data, it was suggested that a convective- or diffusion-based drying model is not sufficient to represent the physics correctly. The assumption of liquid conservation in the pores was found to be not appropriate and a mechanism should be considered for drying from inside

particle pores. Analyzing the experimental data in stage C, different slopes of drying curves at two different locations inside the bed implied that a more complex drying mechanism is involved and hydrodynamic variables such as superficial velocity and particle impact velocity may play a role.

Based on observed deviation, a new mechanism is proposed which takes into account the effect of particle impact velocity and movement of liquid inside the pores which contributes to drying by convective and diffusion effects. The suggested approach can be tested in future research against experimental results.

## Chapter 6: Summary, Contribution and Future Work

This chapter summarizes the most important results and observations obtained from the modeling and experiments reported in the thesis. Recommendations for further research are also provided.

### 6.1 Summary and contributions

- 1- A novel structure-dependent drag-correction model, named force-balance (FB) model, was developed to correctly capture the hydrodynamics in fluidized beds containing Geldart A particles.
- 2- The FB model was tested for prediction of hydrodynamic characteristics such as minimum bubbling velocity, voidage distribution, radial profile of particle volume fraction, bed expansion, formation of agglomerates, and circulation patterns in a bubbling fluidized.

Minimum bubbling velocity predictions from the FB model were compared with predictions from DEM simulations by Hou et al. (2012) for an ideal case with identical smooth particles, and the results are in good agreement with the DEM simulations. The FB model was capable of predicting agglomerate formation, capturing the gross solid circulation phenomena and obtaining promising results for radial voidage profiles and bed expansion predictions from both 2D and 3D simulations. The results based on the FB model are consistent with experimentally measured data. Comparison of predictions from the FB model with those from EMMS model showed that only one version of the EMMS model obtained promising agreement with experimental observations, except for bed expansion predictions. The number of cells utilized for the EMMS model was considerably larger than the number needed for the FB model, a significant benefit of

the latter model, with substantial computational savings when performing large-scale simulations. However, careful mesh studies should be conducted, especially in 2D simulations, where increasing the number of cells does not necessarily improve CFD predictions, especially for the FB model.

- 3- Liquid ethanol injection experiments were conducted at the Institute of Chemical and Fuels from Alternative Sources (ICFAR) of Western University where ethanol was injected into fluidized beds of FCC and sand.

The results indicated that little or no wetting was obtained when ethanol was injected into a bed of sand. Hence the analysis was carried out only for injection into FCC. The effect of fluidization velocity and internal FCC porosity were investigated, and it was found that if the injection time of a volatile liquid is relatively small or the amount of liquid injected into the bed is insufficient to cover all particles, it is not appropriate to assume uniformity of composition, referred to as perfect liquid-solid mixing. For the cases studied in these experiments, it was also concluded that elevating the gas superficial velocity resulted in penetration of more liquid into internal pores, and, consequently, higher moisture content in the FCC particles. An approach was proposed to quantify the liquid-to-solid ratio inside the bed based on electrical capacitance measurements. The quantitative results showed that higher gas superficial velocity resulted in faster drying and greater liquid content inside the bed. These results shed some light on the underlying mechanisms of liquid imbibition into pores and evaporation inside the bed.

- 4- The effect of particle internal porosity on liquid distribution and evaporation in a fluidized bed was studied by performing CFD simulations utilizing existing imbibition and drying models. A new approach was developed, based on a series of assumptions, to incorporate imbibition and drying models in CFD simulations.

The modeling predictions were compared to experimental results from liquid injection experiments conducted at the British Columbia Research Institute (BCRI) in Burnaby with heptane as the liquid. CFD simulations were modified to more fully capture the physics of the experiments.

Different simulations were performed with operating conditions matching those used to obtain experimental data. The effect of particle internal porosity in the early stages of liquid injection was captured by CFD consistently with experimental data. Qualitative agreement was obtained for liquid drying where all particle pores are saturated with liquid and injection continues. However, quantitative deviations were observed, and these were attributed to the more complex effect of convection-diffusion evaporation from liquid layer around the particles and inside particle pores, respectively. Analysis of the CFD results and experimental data where liquid injection was deliberately stopped suggested that hydrodynamic properties such as superficial velocity and particle impact velocities can significantly affect drying kinetics when there is no more liquid injection.

Utilizing the new three-phase modeling approach together with the novel structure-dependent drag correction model, provided a unique set of simulations which gave promising results and shed light on the complexities of liquid injection into gas-solid fluidized beds. Based on modeling results and experimental observations in Chapters 4 and 5, an approach is proposed for testing in CFD which may give better predictions of liquid evaporation from porous particles.

## **6.2 Recommendations for future work**

Despite the fact that the new FB model was found to be capable of predicting important hydrodynamic properties for Geldart Group A group, a definitive conclusion on the effectiveness

of the model requires further simulations and comparisons with experimental data. More work is required in the future to cover a wider range of superficial gas velocities and to compare other hydrodynamic predictions with experimental data. Polydisperse kinetic theory models (Hrenya, 2011) can be considered in the future, instead of mono-disperse theory, to derive a new set of equations for the FB model.

In the case of liquid injection modeling, the simplifying assumptions of convective- or diffusive-driven drying were tested against experimental results. The quantitative deviations suggested a more complex process, involving both drying from particle outer surface and internal porosity, with movement of liquid inside the pores. The proposed mechanism of liquid evaporation from particle surfaces and pores should be tested to make predictions for other systems and then compare these predictions with experimental results. The approach should be further extended to the injection of mixtures of pure liquid and wax to mimic real FCC reactors. The same approach can also be utilized to study liquid distribution and injection in fluidized bed reactors containing non-porous and low-porosity particles (e.g. Fluid Coke).

Combining the new FB model and a working liquid distribution CFD model in the future should provide a useful tool for both academia and industry to better understand the flow behaviour in these reactors and to improve the design and operating of reactors which include liquid injection.

## Bibliography

- Agrawal, K., Loezos, P. N., Syamlal, M., & Sundaresan, S. (2001). The Role of Meso-Scale Structures in Rapid Gas–Solid Flows. *Journal of Fluid Mechanics*, 445, 151–185.
- Ahmadi Motlagh, A. H., Grace, J. R., Salcudean, M., & Hrenya, C. M. (2014). New Structure-Based Model for Eulerian Simulation of Hydrodynamics in Gas–Solid Fluidized Beds of Geldart Group “A” Particles. *Chemical Engineering Science*, 120, 22–36.
- Ancheyta, J. (2011). *Modeling and Simulation of Catalytic Reactors for Petroleum Refining. Simulation* (1st ed.). New Jersey: John Wiley & Sons, Inc.
- Anderson, T. B., & Jackson, R. (1967). A Fluid Mechanical Description of Fluidized Beds. *Ind. Eng. Chem. Fund.*, 6(4), 527–539.
- ANSYS Inc. (2011). *FLUENT 13.0 Theory Documentation*. Canonsburg, PA.
- Arastoopour, H. & Gidspow, D. (1979). Analysis of IGT Pneumatic Conveying Data and Fast Fluidization Using a Thermohydrodynamic Model, *Powder Technology*, 22(1), 77–87.
- Ariyapadi, S. (2004). *Interaction Between Horizontal Gas-Liquid Jets and Gas-Solid Fluidized Beds. PhD Thesis*. Western University, London, ON.
- Benyahia, S. (2012). Analysis of Model Parameters Affecting the Pressure Profile in a Circulating Fluidized Bed. *AIChE Journal*, 58(2), 427–439.
- Benyahia, S., Syamlal, M., & Brien, T. J. O. (2007). Study of the Ability of Multiphase Continuum Models to Predict Core-Annulus Flow. *AIChE Journal*, 53(10).
- Beyhaghi, S., Prat, M., & Pillai, K. M. (2014). Wicking and Evaporation of Liquids in Porous Wicks : A Simple Analytical Approach to Optimization of Wick Design. *AIChE Journal*, 60(5).
- Bruhns, S. (2002). *On the Mechanism of Liquid Injection into Fluidized Bed Reactors. PhD Thesis*. Technischen Universität Hamburg-Harburg.
- Bruhns, S., & Werther, J. (2005). An Investigation of the Mechanism of Liquid Injection into Fluidized Beds. *AIChE Journal*, 51(3), 766–775.
- Cammarata, L., Lettieri, P., Micale, G. D. M., & Colman, D. (2003). 2D and 3D CFD Simulations of Bubbling Fluidized Beds Using Eulerian-Eulerian Models. *International Journal of Chemical Reactor Engineering*, 1(A48).

- Chalermsoonsuwan, B., Gidaspo, D., & Piumsomboon, P. (2011). Two- and Three-Dimensional CFD Modeling of Geldart A Particles in a Thin Bubbling Fluidized Bed: Comparison of Turbulence and Dispersion Coefficients. *Chemical Engineering Journal*, 171(1), 301–313.
- Chen, Y., Yang, J., Dave, R., Pfeffer, R. (2008). Fluidization of Coated Group C Powders. *AIChE Journal*, 54(1), 104–121.
- Cocco, R., Shaffer, F., Hays, R., Reddy Karri, S.B., Knowlton, T. (2010). Particle Clusters in and Above Fluidized Beds. *Powder Technology*, 203(1), 3–11.
- Czachor, H. (2007). Applicability of the Washburn Theory for Determining the Wetting Angle of Soils. *Hydrological Processes*, 2247, 2239–2247.
- Darabi, P. (2011). Mathematical Modeling of Interaction of Wet Particles and Application to Fluidized Beds. *PhD Thesis*, (May).
- Darabi, P., Pougatch, K., Salcudean, M., & Grecov, D. (2009). A Novel Coalescence Model for Binary Collision of Identical Wet Particles. *Chemical Engineering Science*.
- Davis, R. H., Rager, D. a., & Good, B. T. (2002). Elastohydrodynamic Rebound of Spheres from Coated Surfaces. *Journal of Fluid Mechanics*, 468, 107–119.
- Deen, N. G., Van Sint Annaland, M., Van der Hoef, M. A., & Kuipers, J. A. M. (2007). Review of Discrete Particle Modeling of Fluidized Beds. *Chemical Engineering Science*, 62(1-2), 28–44.
- Donahue, C. M., Hrenya, C. M., Davis, R. H., Nakagawa, K. J., Zelinskaya, A. P., & Joseph, G. G. (2010). Stokes' Cradle: Normal Three-Body Collisions between Wetted Particles. *Journal of Fluid Mechanics*, 650, 479.
- Du, B., Warsito, W., & Fan, L. (2006). Flow Dynamics of Gas-Solid Fluidized Beds with Evaporative Liquid Injection. *China Particuology*, 4(1), 1–8.
- Dubrawski, K., Tebianian, S., Bi, H.T., Chaouki, J., Ellis, N., Gerspacher, R., Jafari, R., Kantzas, A., Lim, C., Patience, G.S., Pugsley, T., Qi, M.Z., Zhu, J.X., Grace, J. R. (2013). Traveling Column For Comparison of Invasive and Non-Invasive Fluidization Voidage Measurement Techniques. *Powder Technology*, 235, 203–220.
- Ennis, B. J., Tardos, G., & Pfeffer, R. (1991). A Microlevel-Based Characterization of Granulation Phenomena. *Powder Technology*, 65(1-3), 257–272.
- Enwald, H., Peirano, E., & Almstedt, A.-E. (1997). Eulerian Two-Phase Flow Theory Applied to Fluidization. *International Journal of Multiphase Flow*, 22, 21–66.

- Fan, L., Lau, R., Zhu, C., Vuong, K., Warsito, W., Wang, X., & Liu, G. (2001). Evaporative Liquid Jets in Gas – Liquid – Solid Flow System. *Chemical Engineering Science*, 56, 5871–5891.
- Farkhondehkavaki, M., Engineering, B., & Studies, P. (2012). Developing Novel Methods to Characterize Liquid Dispersion in a Fluidized Bed. *PhD Thesis*.
- Fogler, H. S. (2004). *Elements of Chemical Reaction Engineering* (Third ed.). Michigan: Prentice-Hall of India.
- Forsyth, A., & Rhodes, M. (2000). A Simple Model Incorporating the Effects of Deformation and Asperities into the van der Waals Force for Macroscopic Spherical Solid Particles. *Journal of Colloid and Interface Science*, 223(1), 133–138.
- Frössling, N. (1938). Über die Verdunstung fallender Tropfen. *Gerlands Beitr. Geophys*, 52, 170–216.
- Galet, L., Patry, S., & Dodds, J. (2010). Determination of the Wettability of Powders by the Washburn Capillary Rise Method with Bed Preparation by a Centrifugal Packing Technique. *Journal of Colloid and Interface Science*, 346(2), 470–5.
- Galvin, J.E., Benyahia, S. (2013). The Effect of Cohesive Forces on the Fluidization of Aeratable Powders. *AIChE Journal*, 1–12.
- Gao, J., Xu, C., Lin, S., Yang, G., & Guo, Y. (1999). Advanced Model for Turbulent Gas–Solid Flow and Reaction in FCC Riser Reactors. *AIChE Journal*, 45(5), 1095–1113.
- Gao, J, Chang, J, Xu, C, Lan, X, Yang, Y. (2008). CFD Simulation of Gas Solid Flow in FCC Strippers. *Chemical Engineering Science*, 63(7), 1827–1841.
- Ge, Y., & Fan, L.-S. (2006). Three-Dimensional Direct Numerical Simulation for Film-Boiling Contact of Moving Particle and Liquid Droplet. *Physics of Fluids*, 18(11).
- Gehrke, S., & Wirth, K. (2007). Evaporating Liquid in a High-Density Riser. In *International Congress on Particle Technology (Partec)*. Nurnburg.
- Geldart, D. (1973). Types of Gas Fluidization. *Powder Technology*, 7(5), 285–292.
- Gibilaro, L. G., Felice, R. D. I., & Foscolo, P. U. (1985). Friction Factor and Drag Coefficient Correlations for Fluid-Particle Interactions. *Chemical Engineering Science*, 40(10), 1817–1823.
- Gidaspow, D. (1994). *Multiphase Flow and Fluidization: Continuum and Kinetic Theory Descriptions* (p. 467). New York: Academic Press.

- Gidaspow, D., Jung, J., & Singh, R. (2004). Hydrodynamics of Fluidization Using Kinetic Theory: An Emerging Paradigm (Flour-Daniel Lecture). *Powder Technology*, 148(2-3), 123–141.
- Gidaspow, D., & Lu, H. (1998). Equation of State and Radial Distribution Functions of FCC Particles in a CFB. *AIChE Journal*, 44(2), 279–293.
- Gidaspow, D., & Arastoopour, H. (2014). CFD Modeling of CFB: From Kinetic Theory to Turbulence, Heat Transfer, and Poly-Dispersed Systems. In J. Li, F. Wei, X. Bao, & W. Wang (Eds.), *Proceedings of the 11th International Conference on Fluidized Bed Technology* (pp. 23–31). Beijing: Chemical Industry Press.
- Gu, W., Tuzla, K., & Chen, J. (1966). Measurement of Liquid Spray Evaporation in Fast Fluidized Beds. *AIChE Symp. Ser., Vol. 92*, 153–154.
- Gupta, A. (2001). Model for the Performance of a Fluid Catalytic Cracking (FCC) Riser Reactor: Effect of Feed Atomization. *Chemical Engineering Science*, 56(15), 4489–4503.
- Gupta, A. (2003). Effect of Feed Atomization on FCC Performance: Simulation of Entire Unit. *Chemical Engineering Science*, 58(20), 4567–4579.
- Hong, K., Shi, Z., Wang, W., & Li, J. (2013). A Structure-Dependent Multi-Fluid Model (SFM) for Heterogeneous Gas–Solid Flow. *Chemical Engineering Science*, 99, 191–202.
- Hou, Q. F., Zhou, Z. Y., & Yu, A. B. (2012). Micromechanical Modeling and Analysis of Different Flow Regimes in Gas Fluidization. *Chemical Engineering Science*, 84, 449–468.
- Hrenya, C. (2011). Kinetic Theory for Granular Materials : Polydispersity. *Computational Gas-Solids Flows And Reacting Systems*.
- Igci, Y. (2011). *Closures for Coarse-Grid Simulation of Fluidized Gas-Particle Flows*. PhD Thesis. Princeton University, Dept. of Chemical & Biological Engineering, Princeton, NJ.
- Igci, Y., Iv, A. T. A., Sundaresan, S., & Brien, T. O. (2008). Filtered Two-Fluid Models for Fluidized Gas-Particle Suspensions. *AIChE Journal*, 54(6), 1431–1448.
- Igci, Y., & Sundaresan, S. (2011). Verification of Filtered Two-Fluid Models for Gas-Particle Flows in Risers. *AIChE Journal*, 57(10), 2691–2707.
- Israelachili, J. (1992). *Intermolecular & Surface Forces* (Second Edi.). Santa Barbara: Academic Press.
- Iyer, V. A., Abraham, J., & Magi, V. (2002). Exploring Injected Droplet Size Effects on Steady Liquid Penetration in a Diesel Spray with a Two-Fluid Model, 45, 519–531.

- Jaeger, H. M., & Nagel, S. R. (1992). Physics of Granular States. *Science*, 255(1523-1531).
- Jalalinejad, F. (2013). *Electro-Hydrodynamics of Gas-Solid Fluidized Beds*. The University of British Columbia.
- Johnson, P.C., Jackson, R. (1987). Frictional Collisional Constitutive Relations for Antigranulocytes– Materials, with Application to Plane Shearing. *Journal of Fluid Mechanics*, 176, 67–93.
- Kelly-Zion, P. L., Pursell, C. J., Vaidya, S., & Batra, J. (2011). Evaporation of Sessile Drops under Combined Diffusion and Natural Convection. *Colloids and Surfaces A: Physicochemical and Engineering Aspects*, 381(1-3), 31–36.
- Khan, A. R., & Richardson, J. F. (1990). Pressure Gradient and Friction Factor for Sedimentation and Fluidisation of Uniform Spheres in Liquids. *Chemical Engineering Science*, 45(1), 255–265.
- Kim, H., & Arastoopour, H. (2002). Extension of Kinetic Theory to Cohesive Particle Flow. *Powder Technology*, 83–94.
- Lacks, D. J. (2012). The Unpredictability of Electrostatic Charging. *Angewandte Chemie International Edition*, (51), 6822–6823.
- Leach, A., Chaplin, G., Briens, C., & Berruti, F. (2009). Comparison of the Performance of Liquid–Gas Injection Nozzles in a Gas–Solid Fluidized Bed. *Chemical Engineering and Processing*, 48, 780–788.
- Leach, A., Portoghese, F., Briens, C., & Berruti, F. (2008). A New and Rapid Method for the Evaluation of the Liquid–Solid Contact Resulting from Liquid Injection into a Fluidized Bed. *Powder Technology*, 184(1), 44–51.
- Leclère, K., Briens, C., Gauthier, T., Bayle, J., Bergougnou, M., & Guigon, P. (2001). Liquid Vaporization in a Fluidized Bed. *Industrial & Engineering Chemistry Research*, 40(23), 5415–5420.
- Leclere, K., Briens, C., Gauthier, T., Bayle, J., Guigon, P., & Bergougnou, M. (2004). Experimental Measurement of Droplet Vaporization Kinetics in a Fluidized Bed. *Chemical Engineering and Processing*, 43(6), 693–699.
- Leclere, K., Briens, C. L., Bayle, J., Gauthier, T., Bergougnou, M. A., & Guigon, P. (2001). Experimental Study of Droplet Vaporization in a Fluidized Bed. *Canadian Journal of Chemical Engineering*, 79.
- Lewis, W. K., Gilliland, E. R., Reh, L., Squires, A., Yerushalmi, J., & Kwauk, M. (1992). A Note on Terminology: “Clusters” and “Agglomerates.” *Powder Technology*, 70, 195–196.

- Li, T., Grace, J., & Bi, X. (2010a). Study of Wall Boundary Condition in Numerical Simulations of Bubbling Fluidized Beds. *Powder Technology*, 203(3), 447–457.
- Li, T., Grace, J., Bi, X., Reid, K., & Wormsbecker, M. (2011). Numerical Investigation of Fluid COKING™ Units, Part II: Modelling of Feed Vaporisation. *Canadian Journal of Chemical Engineering*, 1–15.
- Li, T., Grace, J. R., & Bi, X. (2010b). Numerical Investigation of Gas Mixing in Gas-Solid Fluidized Beds. *AIChE Journal*, 56(9).
- Li, T., Mahecha-Botero, A., & Grace, J. R. (2010). Computational Fluid Dynamic Investigation of Change of Volumetric Flow in Fluidized-Bed Reactors. *Ind. Eng. Chem.*, 6780–6789.
- Li, J., Kwauk, M. (1994). *Particle-Fluid Two-Phase Flow: The Energy Minimization Multi Scale Method*. Beijing, P.R. China: Metallurgical Industry Press.
- Liu, G. (2003). *Evaporating Crossflow Sprays in Gas-Solid Flows. PhD Thesis*. New Jersey Institute of Technology.
- Liu, X., & Xu, X. (2009). Modelling of Dense Gas-Particle Flow in a Circulating Fluidized Bed by Distinct Cluster Method ( DCM ). *Powder Technology*, 195(3), 235–244.
- Loezos, P. N., & Sundaresan, S. (2005). Coarse-Grid Simulation of Gas-Particle Flows in Vertical Risers. *Industrial & Engineering Chemistry Research*, 44(16), 6022–6037.
- Lu, H., & Gidaspow, D. (2003). Hydrodynamic Simulations of Gas–Solid Flow in a Riser. *Industrial & Engineering Chemistry Research*, 42(11), 2390–2398.
- Mauleon, J. L., & Courelle, J. C. (1985). FCC Heat Balance Critical for Heavy Fuels. *Oil & Gas Journal*, 83, 64–70.
- Mazzei, L., & Lettieri, P. (2008). CFD Simulations of Expanding/Contracting Homogeneous Fluidized Beds and their Transition to Bubbling. *Chemical Engineering Science*, 63(24), 5831–5847.
- Mckeen, T., & Pugsley, T. (2003a). Simulation and Experimental Validation of a Freely Bubbling Bed of FCC Catalyst. *Powder Technology*, 129, 139–152.
- Mckeen, T., & Pugsley, T. S. (2003b). Simulation of Cold Flow FCC Stripper Hydrodynamics at Small Scale Using Computational Fluid Dynamics Simulation of Cold Flow FCC Stripper Hydrodynamics at Small Scale Using Computational Fluid Dynamics. *International Journal of Chemical Reactor Engineering*, 1, A18.

- McMillan, J., Zhou, D., Ariyapadi, S., & Briens, C. (2005). Characterization of the Contact between Liquid Spray Droplets and Particles in a Fluidized Bed. *Ind. Eng. Chem.*, 4931–4939.
- Mirgain, C., Briens, C., Pozo, M. Del, Loutaty, R., & Bergougnou, M. (2000). Modeling of Feed Vaporization in Fluid Catalytic Cracking. *Industrial & Engineering Chemistry Research*, 39(11), 4392–4399.
- Mohagheghi, M., Hamidi, M., Berruti, F., Briens, C., & McMillan, J. (2013). Study of the Effect of Local Hydrodynamics on Liquid Distribution in a Gas–Solid Fluidized Bed using a Capacitance Method. *Fuel*, 107, 236–245.
- Moreno-Atanasio, R., & Ghadiri, M. (2006). Mechanistic Analysis and Computer Simulation of Impact Breakage of Agglomerates: Effect of Surface Energy. *Chemical Engineering Science*, 61(8), 2476–2481.
- Nayak, S. V., Joshi, S. L., & Ranade, V. V. (2005). Modeling of Vaporization and Cracking of Liquid Oil Injected in a Gas–Solid Riser. *Chemical Engineering Science*, 60(22), 6049–6066.
- Neal, G, Epstein, N., Nader, W. (1973). Creeping Flow Relative to Permeable Spheres. *Chemical Engineering Science*, 28, 1865–1874.
- Newton, D., Fiorentino, M., & Smith, G. B. (2001). The Application of X-ray Imaging to the Developments of Fluidized Bed Processes. *Powder Technology*, 70–75.
- Parmentier, F., Simonin, O., & Delsart, O. (2008). A Numerical Study of Fluidization Behavior of Geldart B, A/B and A Particles Using an Eulerian Multifluid Modeling Approach. In W. Werther, J., Wirth, K.E., Nowak (Ed.), *Ninth International Conference on Circulating Fluidized Beds*. Hamburg, Germany.
- Parmentier, J. (2010). *Extension Du Formalisme Euler/Euler Pour La Simulation des Lits Fluidisés De Particules du groupe A dans la classification de Geldart*. PhD Thesis. Université de Toulouse.
- Parmentier, J.-F., & Simonin, O. (2011). A Functional Subgrid Drift Velocity Model for Filtered Drag Prediction in Dense Fluidized Bed. *AIChE Journal*, 00(0).
- Petersen, D., Link, R., Yeheskel, O., & Tevet, O. (2000). A New Assessment Method for the Bulk Modulus and the Poisson's Ratio of Porous Ceramics. *Journal of Testing and Evaluation*, 28(3), 189.
- Portoghese, F. (2007). *Interactions between Gas-Liquid Jets and Gas-Solid Fluidized Beds*.

- Portoghese, F., Ferrante, L., Berruti, F., Briens, C., & Chan, E. (2008). Effect of Injection-Nozzle Operating Parameters on the Interaction Between a Gas–Liquid Jet and a Gas–Solid Fluidized Bed. *Powder Technology*, 184(1), 1–10.
- Portoghese, F., House, P., Berruti, F., Briens, C., & Chan, E. (2008). Electric Conductance Method to Study the Contact of Injected Liquid with Fluidized Particles. *AIChE Journal*, 54(7).
- Pougatch, K., Salcudean, M., Chan, E., & Knapper, B. (2009). A Two-Fluid Model of Gas-Assisted Atomization Including Flow Through the Nozzle, Phase Inversion, and Spray Dispersion. *International Journal of Multiphase Flow*, 35(7), 661–675.
- Pougatch, K., Salcudean, M., & McMillan, J. (2012). Three-Dimensional Numerical Modelling of Interactions between a Gas–Liquid Jet and a Fluidized Bed. *Chemical Engineering Science*, 68(1), 258–277.
- Rokkam, R. G., Fox, R. O., & Muhle, M. E. (2010). CFD Modeling of Electrostatic Forces in Gas-Solid Fluidized Beds. *The Journal of Computational Multiphase Flows*, 2(4), 189–205.
- Royer, J. R., Evans, D. J., Oyarte, L., Guo, Q., Kapit, E., Möbius, M. E., ... Jaeger, H. M. (2009). High-Speed Tracking of Rupture and Clustering in Freely Falling Granular Streams. *Nature*, 459(7250), 1110–1113.
- Rumpf H. (1990). *Particle Technology*. New York: Chapman and Hall.
- Sadeghbeigi, R. (2012). *An Expert Guide to the Practical Operation, Design, and Optimization of FCC Units*. Butterworth-Heinemann.
- Shi, Z., Wang, W., & Li, J. (2011). A Bubble-Based EMMS Model for Gas–Solid Bubbling Fluidization. *Chemical Engineering Science*, 66(22), 5541–5555.
- Sinclair, J. (1997). Hydrodynamic Modeling. In J. R. Grace, T. M. Knowlton, & A. A. Avidan (Eds.), *Circulating Fluidized Beds*. Academic and Professional Press.
- Skouby, D. (1999). Hydrodynamic Studies in a 0.45-m Riser with Liquid Feed Injection. *AIChE Symp. Ser.*, 95, 67–70.
- Speight, J. G. (2006). *The Chemistry and Technology of Petroleum*. (4th ed.). CRC Press.
- Stevens, A. B., & Hrenya, C. M. (2005). Comparison of Soft-Sphere Models to Measurements of Collision Properties during Normal Impacts. *Powder Technology*, 154(2-3), 99–109.
- Sundaresan, S. (2000). Modeling The Hydrodynamics of Multiphase Flow Reactors: Current Status and Challenges. *AIChE Journal*, 46(6), 1102–1105.

- Sutherland, D. N., & Tan, C. T. (1970). Sedimentation of a Porous Sphere. *Chemical Engineering Science*, 25, 1948–1950.
- Taghipour, F., Ellis, N., & Wong, C. (2005). Experimental and Computational Study of Gas–Solid Fluidized Bed Hydrodynamics. *Chemical Engineering Science*, 60(24), 6857–6867.
- Tebianian, S. (2014). Personal Communication. *University of British Columbia, Dept. of Chemical & Biological Engineering*.
- Terrazas-Velarde, K., Peglow, M., & Tsotsas, E. (2011a). Investigation of the Kinetics of Fluidized Bed Spray Agglomeration Based on Stochastic Methods. *AIChE Journal*, 57(11).
- Terrazas-Velarde, K., Peglow, M., & Tsotsas, E. (2011b). Kinetics of fluidized bed spray agglomeration for compact and porous particles. *Chemical Engineering Science*, 66(9), 1866–1878.
- Tsuji, Y., Tanaka, T., & Yonemura, S. (1998). Cluster Patterns in Circulating Fluidized Beds Predicted by Numerical Simulation. *Powder Technology*, 95, 254–264.
- Van Wachem, B., & Sasic, S. (2008). Derivation, Simulation and Validation of a Cohesive Particle Flow CFD Model. *AIChE Journal*, 54(1), 9–19.
- Veerapaneni, S. A., & Wiesner, M. R. (1996). Hydrodynamics of Fractal Aggregates with Radially Varying Permeability. *Journal of Colloid and Interface Science*, 177, 45–57.
- Vejahati, F., Mahinpey, N., Ellis, N., Nikoo, M. B. (2009). CFD Simulation of Gas-Solid Bubbling Fluidized Bed: A New Method for Adjusting Drag Law. *Canadian Journal of Chemical Engineering*, 87(1), 19–30.
- Waitukaitis, S. R., Grütjen, H. F., Royer, J. R., & Jaeger, H. M. (2011). Droplet and Cluster Formation in Freely Falling Granular Streams. *Physical Review E*, 83, 1–12.
- Wang, J. (2009). A Review of Eulerian Simulation of Geldart A Particles in Gas-Fluidized Beds. *Industrial & Engineering Chemistry Research*, 48(12), 5567–5577.
- Wang, J., Ge, W., & Li, J. (2008). Eulerian Simulation of Heterogeneous Gas–Solid Flows in CFB Risers: EMMS-Based Sub-Grid Scale Model with a Revised Cluster Description. *Chemical Engineering Science*, 63(6), 1553–1571.
- Wang, J., Hoef, M. A. Van Der, & Kuipers, J. A. M. (2010). CFD Study of The Minimum Bubbling Velocity of Geldart A Particles in Gas-Fluidized Beds. *Chemical Engineering Science*, 65(12), 3772–3785.

- Wang, J., van der Hoef, M. a., & Kuipers, J. A. M. (2011). The Role of Scale Resolution versus Inter-Particle Cohesive Forces in Two-Fluid Modeling of Bubbling Fluidization of Geldart A Particles. *Chemical Engineering Science*, 66(18), 4229–4240.
- Wang, J., Vanderhoef, M., & Kuipers, J. (2009). Why the Two-Fluid Model Fails to Predict the Bed Expansion Characteristics of Geldart A Particles in Gas-Fluidized Beds: A Tentative Answer. *Chemical Engineering Science*, 64(3), 622–625.
- Wang, W., & Li, J. (2007). Simulation of Gas–Solid Two-Phase Flow by a Multi-Scale CFD Approach of The EMMS Model to The Sub-Grid Level. *Chemical Engineering Science*, 62(1-2), 208–231.
- Washburn, E. W. (1921). The Dynamics of Capillary Flow. *The Physical Review*, 273–283.
- Wei, W. (2013). *Personal Communication*. Chinese Academy of Sciences.
- Wen, C.Y., Yu, Y. H. (1966). Mechanics of Fluidization. *Chemical Engineering Progress Symposium Series*, 62, 100–111.
- Wu, C., Cheng, Y., & Jin, Y. (2009). Understanding Riser and Downer Based Fluid Catalytic Cracking Processes by a Comprehensive Two-Dimensional Reactor Model. *Industrial & Engineering Chemistry Research*, 48(1), 12–26.
- Xiao, F., Li, X. Y., & Wang, D. S. (2013). Three-Dimensional CFD Simulation of the Flow Field around and Through Particle Aggregates. *Colloids and Surfaces A: Physicochemical and Engineering Aspects*, 436, 1034–1040.
- Xie, H. (1997). The Role of Interparticle Forces in the Fluidization of Fine Particles. *Powder Technology*, 94, 99–108.
- Yang, W. (1996). Hardware Design of Electrical Capacitance Tomography Systems. *Meas Sci Technology*, 7, 225–232.
- Yates, Y. G., Cheesman, D. J., & Sergeev, Y. A. (1994). Experimental Observations of Voidage Distribution around Bubbles in a Fluidized Bed. *Chemical Engineering Science*, 49(12), 1885–1895.
- Ye, M., Van Der Hoef, M. A., & Kuipers, J. A. M. (2005). From Discrete Particle Model to a Continuous Model of Geldart A Particles. *Chemical Engineering Research and Design*, 83(7), 833–843.
- Yildirim, I. (2001). *Surface Free Energy Characterization of Powders*. Virginia Polytechnic Institute and State University.

- Zhang, D. (2002). The Effects of Mesoscale Structures on the Macroscopic Momentum Equations for Two-Phase Flows. *International Journal of Multiphase Flow*, 28(5), 805–822.
- Zhou, T., & Li, H. (1999). Estimation of Agglomerate Size for Cohesive Particles During Fluidization. *Powder Technology*, 101, 57–62.
- Zhou, T., & Li, H. (2000). Force Balance Modelling for Agglomerating Fluidization of Cohesive Particles. *Powder Technology*, 111, 60–65.
- Zhu, C., Wang, X., & Fan, L. (2000). Effect of Solids Concentration on Evaporative Liquid Jets in Gas–Solid Flows. *Powder Technology*, 111, 79–82.
- Zimmermann, S., & Taghipour, F. (2005). CFD Modeling of the Hydrodynamics and Reaction Kinetics of FCC Fluidized-Bed Reactors. *Ind. Eng. Chem.*, 44, 9818–9827.